Development of new thin film scintillators for high-resolution X-ray imaging

Federica Riva

N° d'ordre NNT : 2016LYSE1195

THÈSE DE DOCTORAT DE L'UNIVERSITÉ DE LYON

opérée au sein de
ESRF - European Synchrotron Radiation Facility
ILM - Institut Lumière Matière

Delivrée par :
Université Claude Bernard Lyon 1
École Doctorale de Physique et d'Astrophysique de Lyon - PHAST

DIPLÔME DE DOCTORAT

Soutenue publiquement le 20/10/2016, par :
Federica RIVA

Développement des nouveaux scintillateurs en couche mince pour l'imagerie par rayons-X à haute résolution

---

Devant le jury composé de :

Alfonso SAN MIGUEL-FUSTER Professeur, Université de Lyon	**Président**
Patrice CAMY Professeur, Université de Caen	**Rapporteur**
Anna VEDDA Professeur, Università Milano-Bicocca	**Rapporteur**
Peter CLOETENS Scientifique à l'ESRF	**Examinateur**
Thierry MARTIN Docteur-Ingenieur à l'ESRF	**Examinateur**
Jean-Louis SANTAILLER Docteur-Ingenieur au CEA-LETI	**Examinateur**
Christophe DUJARDIN Professeur, Université de Lyon	**Directeur de thèse**

N° d'ordre NNT : 2016LYSE1195

THESIS SUBMITTED FOR THE DEGREE OF
DOCTOR OF PHILOSOPHY (PhD)

ILM - Institut Lumière Matière
ESRF - European Synchrotron Radiation Facility

Université Claude Bernard Lyon 1
École Doctorale de Physique et d'Astrophysique de Lyon - PHAST

Federica RIVA

Development of new thin film scintillators for high-resolution X-ray imaging

---

Members of the jury :

Alfonso SAN MIGUEL-FUSTER Professor, Université de Lyon	**President**
Patrice CAMY Professor, Université de Caen	**Referee**
Anna VEDDA Professor, Università Milano-Bicocca	**Referee**
Peter CLOETENS Doctor, Scientist at ESRF	**Examiner**
Thierry MARTIN Doctor, Engineer at ESRF	**Examiner**
Jean-Louis SANTAILLER Doctor, Engineer at CEA-LETI	**Examiner**
Christophe DUJARDIN Professor, Université de Lyon	**Thesis Director**

UNIVERSITE CLAUDE BERNARD - LYON 1

Président de l'Université	**M. le Professeur Frédéric FLEURY**
Président du Conseil Académique	M. le Professeur Hamda BEN HADID
Vice-président du Conseil d'Administration	M. le Professeur Didier REVEL
Vice-président du Conseil Formation et Vie Universitaire	M. le Professeur Philippe CHEVALIER
Vice-président de la Commission Recherche	M. Fabrice VALLÉE
Directeur Général des Services	M. Alain HELLEU

COMPOSANTES SANTE

Faculté de Médecine Lyon Est – Claude Bernard	Directeur : M. le Professeur J. ETIENNE
Faculté de Médecine et de Maïeutique Lyon Sud – Charles Mérieux	Directeur : Mme la Professeure C. BURILLON
Faculté d'Odontologie	Directeur : M. le Professeur D. BOURGEOIS
Institut des Sciences Pharmaceutiques et Biologiques	Directeur : Mme la Professeure C. VINCIGUERRA
Institut des Sciences et Techniques de la Réadaptation	Directeur : M. X. PERROT
Département de formation et Centre de Recherche en Biologie Humaine	Directeur : Mme la Professeure A-M. SCHOTT

COMPOSANTES ET DEPARTEMENTS DE SCIENCES ET TECHNOLOGIE

Faculté des Sciences et Technologies	Directeur : M. F. DE MARCHI
Département Biologie	Directeur : M. le Professeur F. THEVENARD
Département Chimie Biochimie	Directeur : Mme C. FELIX
Département GEP	Directeur : M. Hassan HAMMOURI
Département Informatique	Directeur : M. le Professeur S. AKKOUCHE
Département Mathématiques	Directeur : M. le Professeur G. TOMANOV
Département Mécanique	Directeur : M. le Professeur H. BEN HADID
Département Physique	Directeur : M. le Professeur J-C PLENET
UFR Sciences et Techniques des Activités Physiques et Sportives	Directeur : M. Y.VANPOULLE
Observatoire des Sciences de l'Univers de Lyon	Directeur : M. B. GUIDERDONI
Polytech Lyon	Directeur : M. le Professeur E.PERRIN
Ecole Supérieure de Chimie Physique Electronique	Directeur : M. G. PIGNAULT
Institut Universitaire de Technologie de Lyon 1	Directeur : M. le Professeur C. VITON
Ecole Supérieure du Professorat et de l'Education	Directeur : M. le Professeur A. MOUGNIOTTE
Institut de Science Financière et d'Assurances	Directeur : M. N. LEBOISNE

Acknowledgements

Many people supported me and the project presented in this thesis. I would like to thank all of them for their contribution.
I would like to thank Pablo Fajardo and all the people in the detector and electronics group, for the warm welcome at the ESRF.
Thank you to Anna Vedda and Patrice Camy, for reviewing my work, and to all the members of the jury.
Thank you to my thesis director, Christophe Dujardin, for the academic support and the useful discussions.
A huge thank you to my ESRF supervisor, Thierry Martin, and to Paul-Antoine Douissard, for their essential help. Thank you Thierry, for being a great supervisor, supporting my project while always letting me free to choose the direction of my research. Thank you Paul-Antoine, for teaching me everything about the liquid phase epitaxy. And thank you both, for the enjoyable company and great help during the often-too-long days (and nights) spent on the beamline.
Thank you to all the people that helped me with the experiments: Eric Mathieu, for the crystal growth, Christophe Jarnias for the mechanics of the detectors, Eric Ziegler, Tamzin Lafford, Sebastien Berujon, Samuel Da Chuna, Jurgen Hartwig, Manuel Perez and Roberto Homs, for the help on BM05, Francesco Carlà for the measurements on ID03, Irina Snigurev, for the SEM images, Federico Moretti, for the help with the lab in Lyon, Jerome Debray, for the Laue measurements, Claudio Ferrero, Manuel Sanchez, Olivier Hignette, Iwan Cornelius, for all the hints about the simulations.
I would also like to thank all the wonderful people I met in Grenoble which made the last years an amazing period of my life. Thank you to Leandro, the first friend I met in Grenoble, Leoncino, for all the dinner together (with or

without invitation) and for the company during the "writing-weekends", Niccolo' for listening for the second time at my complaints while writing, Pasini for always washing the dishes, Flavia, for taking care of Pasini, Micheal, for the movie selection. Thank you to all the officemates from the office 01.1.06: Andrea, Sara, Ilaria, Genziana, Raphael (ok, you were there enough that I can thank you in this line). Thank you Stefan and Katharina, for all the time spent together in France, Germany and in the Netherlands! Thank you Claire, for these years of flat-sharing and the intensive French lessons.

Thank you to all the friends in Italy and to the ones that moved as me to other countries. Unfortunately, hanging out with you is not so easy as before, but thank you for every time you find the time for a message, a call, or a drink together.

Thank you to my family, my brother Matteo and his wife Francesca, for always being an example, and to my parents Paola and Edo, that supported me every single day.

Aryan, out of one million reasons to acknowledge you, thank you for loving me exactly as I am.

Contents

Chapter 1

Introduction

1.1 Scope of the thesis

In 1985 the german scientist W. C. Röntgen discovered X-rays and showed their potential as a tool to investigate matter. Due to the development of X-ray sources, experimental techniques and detectors, X-ray imaging today has been improved to the point that structures down to the nanoscale can be resolved. Firstly, the availability of modern X-ray generators and synchrotron sources improved the quality of the X-ray beam in terms of flux, coherence and divergence. Secondly, many new experimental techniques have been developed. For example, X-ray imaging can exploit today not only X-ray absorption contrast but also X-ray phase contrast. Lastly, X-rays detectors evolved from photographic films to modern semiconductor detectors, which allow fast recording of many digital images.

As a consequence of the requirements coming from many different X-ray applications, several kinds of detectors have been developed. At synchrotrons, the state-of-the-art detectors for high-resolution imaging (i.e. below 2 μm) are indirect detectors using a single crystal thin film scintillator, microscope optics and a pixelated semiconductor camera. Such detectors and single crystal thin film scintillators are the subject of this thesis. The aim was the study of the performance of indirect detectors and the development of new scintillators, in an attempt to improve the detectors' performance, especially at high energy (20-100 keV).

A general introduction summarizing advantages and limitations of different kinds of X-ray detectors and scintillators is presented in chapter one.

Afterwards, this thesis is divided into two main subjects. The first part (chapters 2 and 3) describes a model to calculate the spatial resolution of indirect detectors.
The second part is focused on materials development. Aluminum perovskite and lutetium oxide have been developed as single crystal thin films using liquid phase epitaxy. The description of the optimization of the crystal growth process, material characterization and imaging performances is presented in chapters 4, 5 and 6.

1.2 Detectors for synchrotron imaging applications

X-ray imaging techniques are powerful tools to investigate 3D structures without using destructive analysis. Currently X-ray imaging techniques can resolve details down to the nanometer scale and allow the investigation of structures with variable absorptions through the combination of absorption and phase contrast. An example is shown in figure 1.1, details can be found in (1). Fossil flowers were imaged using a combination of phase contrast X-ray imaging techniques, with a resolution in the range from 50 nm to 0.75 μm. The breakthrough shown in these results is the 3D investigation of individual pollen grains and their nanometer structures. To achieve this, it was needed to increase the X-ray energy to reduce the sample absorption which is detrimental for the phase contrast. The energy was increased up to 29.5 keV, to reduce the sample's absorption, which is detrimental for the phase contrast.
Applications as the one shown in figure 1.1, require a detector with spatial resolution down to the micrometer or sub-micrometer scale. Moreover, the detector must be efficient at X-ray energies above 20 keV, since these high-energies are often selected to increase the X-ray penetration in the object. Two dimensional (pixelized) detectors are today preferred for many X-ray applications, not only imaging but also crystallography, absorption or scattering experiments. Not only are these state-of-the-art detectors in demand at large experimental facilities as synchrotrons or X-ray free-electron lasers, but they are also often preferred for experiments using X-ray laboratory sources and widely used for medical or security applications.
Depending on the mechanism of detection, X-ray area detectors can be classified into two groups. Direct detectors using semiconductors, which convert X-ray photons directly into an electronic signal, and indirect detectors which first convert the X-ray photons into photons of lower energy which are detected subsequently. The detection mode

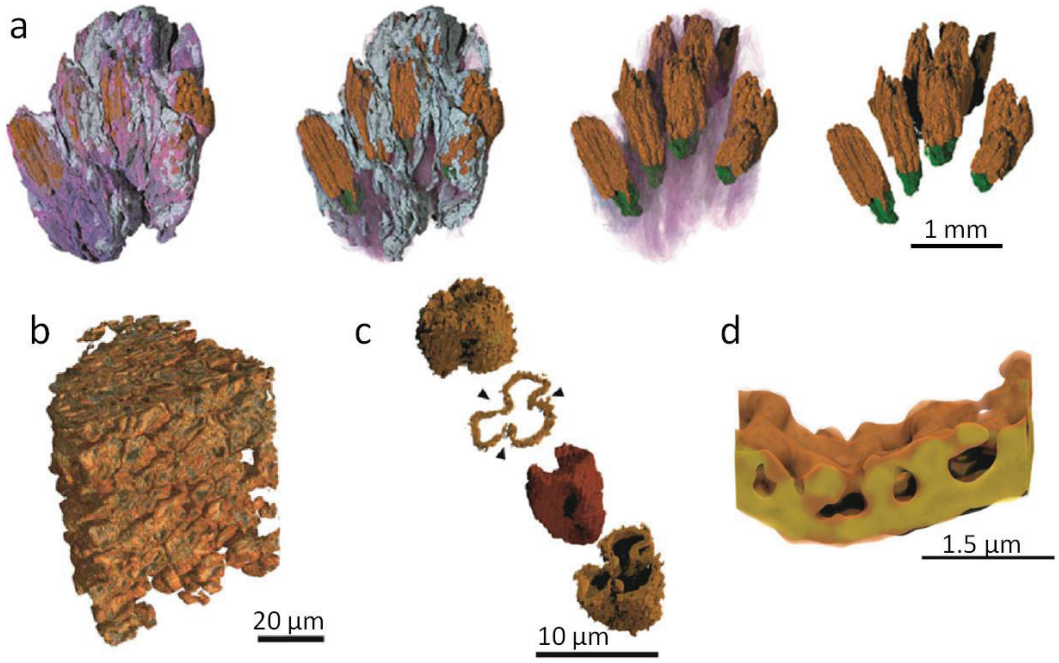

Figure 1.1: Multi-scale 3D X-ray imaging of fossil flowers. (a) X-ray synchrotron micro-tomography showing the spatial organization of the inflorescence. Gray, sediment; purple, inflorescence receptacle and perianth units; orange, pollen sacs; green, staminal filaments. Data recorded at the ESRF beamline BM05, 25 keV. (b, c, d) X-ray nano-tomography of (b) a pollen sac, (c) virtual dissection of a pollen grain (d) sub-micrometer structures inside a pollen grain. Data recorded at the ESRF beamline ID22-NI (today ID16A-NI), 29.5 keV. For more details see (1).

is an other type of classification for detectors. There are two types, photon-counting or integrating detectors. In photon-counting detectors, the pulse generated from an individual X-ray photon is immediately processed and eventually counted. The pulse can give information on the arrival time of the single photon as well as its energy. Integrating detectors accumulate the created charge over a set exposure time and the total signal is read at its completion. The information is the charge generated by the total amount of photons detected during the exposure time.

It is worth to mention that the use of point spectroscopy detectors often remains the best choice when high energy-resolution is required, as is for instance the case of elemental imaging using X-ray fluorescence, where the spatial resolution is obtained by scanning the X-ray beam across the sample.

1.2.1 Indirect 2D detectors

The detectors based on indirect detection can be schematically divided into three elements which can be chosen to optimize the detector for a specific task.
The first element is the converter screen, called the scintillator. Many converter screens, produced using different materials and technologies, are available today. For example for X-ray imaging, single crystalline film (SCF) scintillators are normally preferred as converter screens when micrometer or sub-micrometer resolution is required (2, 3), micro-structured crystalline scintillators are selected to improve efficiency at high X-ray energies and powder or ceramic phosphors are often the most viable solution when a large field of view is required.
The second element is an optical guide or projection system which couples the converter screen with the imaging camera. This part can be made using lenses or optical fiber bundles. The latter are normally more efficient, but resolution below a few micrometers can only be obtained using microscope optics (4, 5).
The last element is the imaging camera. Two main technologies are available, CCD (Charge-Coupled Devices), as well as their derivative as EMCCD (Electron Multiplying CCD), and CMOS (Complementary Metal Oxide Semiconductor) sensors. In a CCD camera, each pixel is associated to a potential well, where the electrons are accumulated. At the end of the exposure the charge of each pixel is transferred from well to well in a sequence and finally amplified and converted into a digital signal. In a CMOS camera, additional electronics process the signal at each pixel. The reading can be done line by line without stopping the acquisition (rolling shutter mode) allowing higher frame rates as compared to a CCD. However, the additional electronics also limit the smallest achievable pixel size. Currently many different imaging cameras have been developed, and both CCD and CMOS detector types are mature and reliable technologies.
A drawback of 2D indirect detectors is their noise, due to the camera but also due to the additional step in the detection chain. The maximum attainable dynamic range is limited on one side by the noise and on the other side by the full-well capacity. However, the only viable way to reach sub-micrometer scale resolution is through the use of indirect detectors which as an added benefit can be used efficiently at very high energies, if a proper converter screen is selected, and in high synchrotron fluxes. Moreover, indirect detectors are cheaper than pixelized direct detectors (especially if compared to detec-

tors based on high-Z semiconductor materials as CdTe) and their configuration is more flexible, meaning they can be adapted to a broader range of experimental conditions.

1.2.2 Direct 2D detectors

Direct X-ray detectors convert X-rays directly in electronic charge. Two technologies have been developed for direct X-ray detection: hybrid pixel array detectors ad monolithic detectors.

Hybrid pixel array detectors (HPADs) are made of two layers. A pixelized sensor layer, where the X-rays are absorbed and converted into electron-hole pairs, and a second layer responsible for the signal processing. Each pixel in the first layer is micro-soldered to a chip in the second one through a so-called "bump". The advantage of hybrid pixels is the possibility to separately optimize the two layers. To enhance the absorption at high X-ray energies, CdTe or GaAs can be selected for the sensor layer while silicon can still be used for the electronic circuits. The drawback is the delicate and expensive operation of interconnection of the two layers, which also limits the smallest obtainable pixel size.

Most of HPADs work only in photon-counting mode which means that each time a photon is detected, the signal is immediately processed, compared with a threshold and counted or rejected. This mode allows noise-free performance and energy discrimination, but the main limitation is the maximum X-ray flux that these detectors can manage ($10^6 - 10^8\,\mathrm{ph/mm^2/s}$). If the flux is higher, an easy feat at synchrotron sources, the arrival time between two photons is lower than the detector's dead time and the two photons get counted as one. Today some HPADs working in integration mode are under development, as for example the MÖENCH detector (6).

Monolithic detectors (MDs) have both the absorbing sensor and the readout circuits on the same chip. The advanced circuits needed for the readout chip are currently only made using silicon which immediately limits the application of MDs to applications using relatively low X-ray energies as the absorbing sensor, also made of silicon, will become transparent for energies above 20 keV. Monolithic detectors with pixels as small as $20 \times 20\,\mu m^2$ can be fabricated, which is smaller than the limit today attainable for commercial HPADs, as for instance the MAXIPIX HPAD which has pixels of $55 \times 55\,\mu m^2$ (7)). However, HPADs with smaller pixel size are under development: the MÖENCH prototype has pixels of $25 \times 25\,\mu m^2$. Two kinds of monolithic detectors have

been developed and are currently investigated: passive-pixel MDs, that can be seen as direct-detection CCDs, and active-pixel MDs, which correspond to direct detection CMOS chips (8).

1.2.3 Some 2D detectors at the ESRF

Compared to laboratory sources, the X-ray fluxes at modern synchrotrons are much higher. This can be seen in figure 1.2, where the brilliance of laboratory sources is compared with others. While the brilliance of X-ray laboratory sources is well below 10^{10} ph/s/mrad^2/0.1%bw, for most modern synchrotrons, it can reach values above 10^{21} ph/s/mrad^2/0.1%bw, which is more than 10 orders of magnitude higher. The

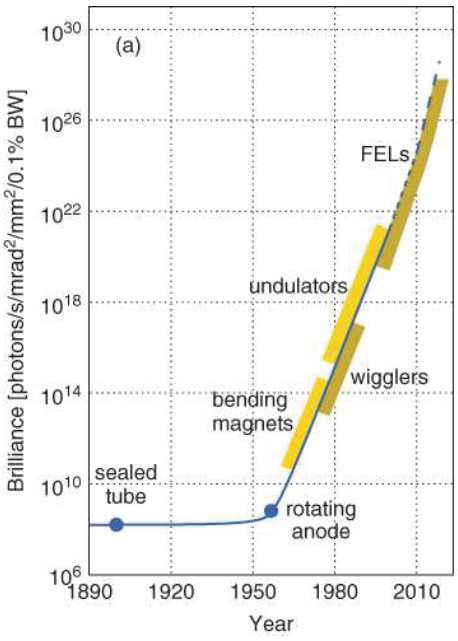

Figure 1.2: Brilliance of different X-ray sources (9).

photon flux available at the sample position depends on the X-ray energy and beamline configuration, but fluxes above 10^9 ph/s/mm^2 (typically $10^{12} - 10^{13}$ ph/s/mm^2) are easily attained. Due to the required dead time in HPADs the maximum photon flux is approximately $10^4 - 10^6$ photons per pixel per second, which for a $100 \times 100\,\mu m^2$ pixel corresponds to a maximum photon flux of 10^8 ph/mm^2/s. Consequently HPADs can only be used for applications where the X-ray beam does not imping directly on

the detector as is the case with diffraction or inelastic scattering experiments. However, even in this case, the flux is often too high and still needs to be attenuated, as for example close to some intense Bragg reflection peaks.

The ESRF as well as several other synchrotrons (see figure 1.3) can deliver high-energy X-ray photons, far above 20 keV. Such high energies are needed to increase the penetration of X-ray photons into matter and allow the investigation of thick and highly absorbing samples. Unfortunately, due to their higher penetration length, high-energy photons are also more challenging to detect. Since silicon sensors are not sufficiently absorbing above 20 keV, the solution has to be sought in indirect detectors or HPADs with high-Z sensors (e.g. CdTe, CdZnTe and GaAs).

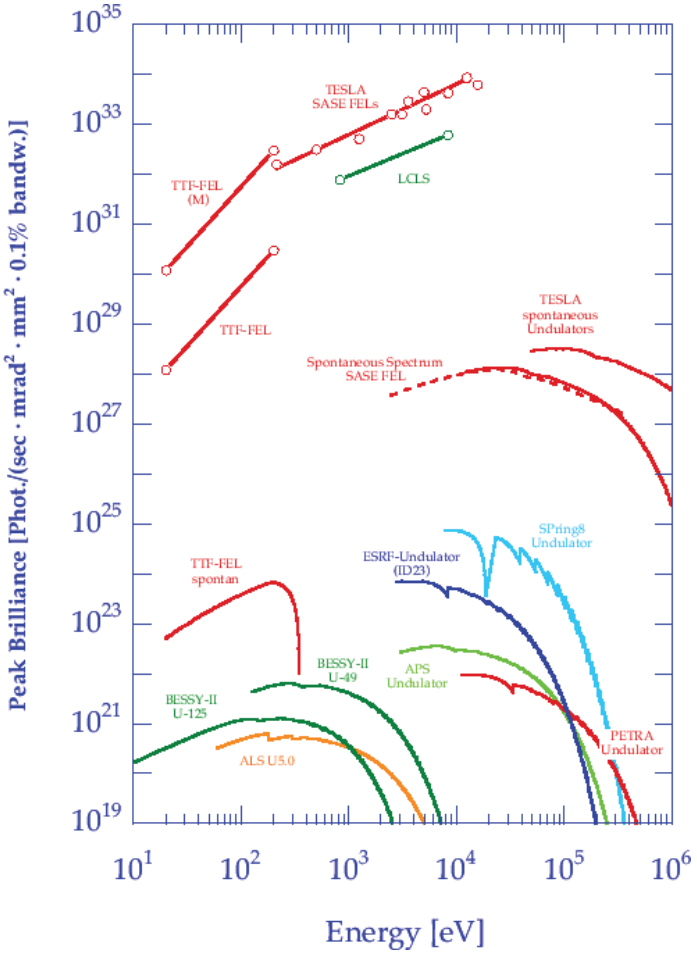

Figure 1.3: X-ray energy spectra of different synchrotrons and free electron lasers (10).

HPADs are the state-of-the-art detectors for crystallography and inelastic scattering

experiments. The newest HPAD is the EIGER detector developed at PSI and commercialized by DECTRIS (11). This detector was recently installed at two ESRF beamlines, ID30 and ID13 where it can only be used for low energy experiments since it is currently only available with a silicon sensor layer. For these beamlines this is however not problematic. The ID30 beamline is dedicated to structural biology applications where crystals made of macromolecules are investigated using X-ray diffraction. Since the absorption of biological samples is low, the experiments are performed at X-ray energies below 20 keV. In fact, the EIGER detector is mounted in a setup for X-ray diffraction working at a fixed energy of 12.8 keV. Approximately the same energy (13 keV) is used at beamline ID13 which delivers a small focal spot used for diffraction and small angle X-ray scattering (SAXS).

A different HPAD system is the MAXIPIX detector, which was developed at the ESRF, based on the Medipix chip (7). MAXIPIX detectors are widely used at the ESRF, for example at the beamlines ID01 for nano-diffraction and ID03 for surface diffraction. Both beamlines are optimized to work below 25 keV, therefore, the MAXIPIX detector with silicon sensor is still acceptable in term of efficiency.

However, the same experiments can be performed at higher energies, for example at ID31, where a monochromatic X-ray beam up to 140 keV can be delivered. Such high-energies are used for material investigations where high-penetration is required, for example in the study of deeply buried interfaces. Due to the interest from medical imaging and homeland security much progress in high-Z sensors made of CdTe, Cd(Zn)Te and GaAs has been seen in the last years. Although the homogeneity, the quality and the radiation hardness of these high-Z materials is not yet as good as silicon, some HPADs based on these materials have already been developed. For example, some HPADs used at the ESRF are available with a CdTe sensor layer, e.g. the MAXIPIX (12, 13), the Dectris Pilatus (ID31) and the Pixirad (BM05) detectors. An alternative for the sensor layer is GaAs which is being used in the LAMBDA detector (14).

In X-ray absorption and phase contrast imaging experiments part of the direct X-ray beam impinges on the detector, leading to X-ray fluxes that are too high to be managed for the photon counting mode and can even damage the detector. As there are more advantages, imaging experiments often prefer indirect detection techniques over HPAD technology. Several advantages are listed below. Firstly, the radiation damage of the camera can be avoided by modifying the detector design. Secondly, in integration mode

higher fluxes can be managed by adjusting the integration time. Thirdly, the indirect detectors are more flexible than direct detectors as the visible image emitted by the converter screen can be magnified to obtain smaller pixels or demagnified for a larger field of view. And lastly, indirect detectors are normally cheaper than HPADs. Typical prices for 4 megapixel commercial products are in the order of 100 k€ for indirect 2D detectors, 600 k€ for HPADs with Si sensor and 1 M€ for the ones with CdTe sensor. A few examples of beamlines at the ESRF which use indirect detector technology are ID19, ID17 and ID16.

ID19 is a beamline mainly dedicated to micro-tomography. The detectors are based on indirect detection and they can be configured to optimize the performance depending on the demands of the experiment. Different converter screens, optics and cameras are available and the scientists can quickly change the detector configuration (15). For sub-micrometer spatial resolution, single crystal thin film scintillators are combined with high numerical aperture microscope optics and pixelized cameras, for example the FreLon camera (16). Thicker scintillators doped with Ce are preferred to improve the efficiency at high X-ray energies or for time-resolved experiments.

ID17 is a beamline for biomedical and paleontology applications. The peculiarity of imaging experiments performed on this beamline is the large field of view (up to 15 cm), while the resolution is normally limited to few hundreds of micrometers. In this case, configurations using powder phosphors (Gadox) and fiber optic coupling have been implemented (17).

ID16 is a beamline dedicated to nano-imaging and nano-analysis and is specialized in X-ray techniques to investigate materials down to the nano-scale. Varying detectors are used depending on the experiment. For absorption and phase contrast imaging, the detector is based on indirect detection with a configuration similar to ID19. For pthychography, a technique based on X-ray diffraction, a MAXIPIX detector is used in combination with a Frelon camera in indirect mode. The central part is detected by the indirect detector and the ring by the MAXIPIX.

1.2.4 Spectroscopy detectors

X-ray imaging synchrotron techniques for elemental mapping, e.g. X-ray fluorescence (XRF) imaging, mainly use point detectors which are sensitive to the X-ray energy. The spatial resolution is obtained by focusing the X-ray beam down to the nanometer scale

and moving the sample across the beam.
A first example at the ESRF is the nano-XRF setup at the beamline ID16B, which can exploits X-ray energies up to 70 keV (18). The element discrimination is based on energy dispersive (ED) detectors: silicon drift detectors (SDDs) are used up to 25 keV, while at higher energies, they are replaced by Germanium based detectors.
A second example is the micro-XRF setup at the beamline ID21 (19). The detection system includes a wavelength dispersive (WD) spectrometer. The fluorescence X-ray photons are guided with polycapillary optics on a monochromator and are detected using a gas-flow proportional counter. Compared to energy dispersive SDDs, which have an energy resolution limited to hundreds of eV, the WD spectrometer enhance the energy resolution to tens of eV. Additionally, they are more efficient in the low X-ray energy range (1-10 keV), allowing a more precise and unequivocal elemental identification.

1.3 Detector characterization for high-resolution X-ray imaging

Many parameters need to be taken into account in the evaluation of a detector. Because of this, the optimization of one parameter often comes at the expense of an other. The design of a detector is thus a compromise. A first example is the compromise between spatial resolution and efficiency. High-resolution requires thin film scintillators, leading to weak absorption. Additionally, the acquisition speed will be reduced due to the time needed to integrate the signal. A second example is the camera's frame rate (speed) which can be improved at the price of the dynamic range and the number of pixels. Hybrid pixels detectors outperform indirect detectors in terms of sensitivity and low noise, but the flux which can be detected is lower. Consequently, the experiments to be performed need to be carefully evaluated in order to understand which detector parameters have to be optimized for a successful experiment. In addition it is important to keep the cost of the detector manageable. HPADs are much more expensive than indirect detectors, which are for this reason often the preferred choice in many fields. A brief introduction of some important detector parameters is presented in the following sections.

1.3.1 Detective quantum efficiency

Every detector used to record a signal inherently introduces an uncertainty in the measurement. One of the most widely accepted parameters to quantify this uncertainty is the detective quantum efficiency (DQE). The DQE value ranges from 0 for a detector which does not detect any signal, to 1 for an ideal detector which perfectly localizes the full energy of every incident X-ray photon. In reality a DQE equal to 1 can not be obtained, since any statistical process, background noise or loss of events involved in the detection process lowers the DQE value. Moreover, a compromise has to be made between the DQE and other properties as the readout speed and the dynamic range.
The DQE is defined as the square of the output signal-to-noise ratio divided by the input signal-to-noise ratio:

$$\mathrm{DQE} = (\mathrm{S_o}/\sigma_\mathrm{o})^2/(\mathrm{S_i}/\sigma_\mathrm{i})^2 \ , \tag{1.1}$$

where $\mathrm{S_{o/i}}$ and $\sigma_{\mathrm{o/i}}$ are the average value and the standard deviation of the output/input signal. If the input signal is described by a Poisson distribution, equation 1.1 becomes

$$\mathrm{DQE} = 1/(\mathrm{N_i\,R}) \ , \qquad \mathrm{R} = (\sigma_\mathrm{o}/\mathrm{S_o})^2 \ , \tag{1.2}$$

where $\mathrm{N_i}$ is the number of incident X-ray photons and R is the relative variance of the output signal.
In the detection process the signal generated from the detected X-ray photon propagates trough the different elements of the detector, resulting in a signal at the output. Therefore, it is necessary to include the elements and processes involved if one wants to calculate the DQE. From the gain (or efficiency), statistical distribution and noise of each process involved, the relative variance of the entire system (R) is given by

$$\mathrm{R} = \mathrm{R_o} + \frac{\mathrm{R_1}}{\mathrm{m_o}} + \frac{\mathrm{R_2}}{\mathrm{m_0\,m_1}} + ... + \frac{\mathrm{R_n}}{\prod_{\mathrm{i=1}}^{\mathrm{n-1}} \mathrm{m_i}} \ , \tag{1.3}$$

where $\mathrm{m_o}$ is the number of incident X-ray photons, $\mathrm{R_o}$ is its relative variance, $\mathrm{m_i}$ and $\mathrm{R_i}$ are respectively the gain and relative variance of each of the processes involved in the detection cascade (20). It is clear that for an increasing number of involved processes in the detection, the DQE will reduce.
Many models have been developed to estimate the DQE of the several kinds of detectors

and configurations used for different applications. Following the approach reported in (20) and (21) we can estimate the DQE evaluated at low frequencies for indirect high-spatial resolution X-ray detectors. A cascade of processes is involved in the detection, each one with a statistical distribution:

- X-ray absorption in the scintillator $\quad m_0 = N_i\,\eta_{abs} \quad R_0 = \frac{1}{N_i\,\eta_{abs}}$
- Scintillator light emission $\quad m_1 = \eta_{LY} \quad R_1 = \frac{1}{\eta_{LY}} + R_s$
- Light transmission through the optics $\quad m_2 = T_l \quad R_2 = \frac{1}{T_l} - 1$
- Camera quantum efficiency $\quad m_3 = \eta_{QE} \quad R_3 = \frac{1}{\eta_{QE}}$
- Camera noise $\quad R4 = \frac{n_{eff}^2}{N_i}$.

N_i is the incident photon flux, η_{abs} and η_{LY} are the scintillator absorption efficiency and light yield. R_S depends on the scintillator, it is approximately 0 for a transparent single-crystal and is higher for a powder phosphor because of the scattered and re-absorbed light which broadens the statistical distribution. Trapping of light due to total internal reflection is included in the evaluation of η_{LY}. T_l is the transmission of the optical path. As first approximation, the transmission of the optics can be assumed equal to its upper limit which is given by the efficiency collection $\eta_{col} = \frac{1}{4}(NA/n)^2$. η_{QE} is the quantum efficiency of the sensor at the emission wavelength of the scintillator, while η_{eff} is the camera noise. The absorption of the X-ray window before the scintillator is neglected. Equation 1.3 can be re-written as:

$$R = \frac{1}{\eta_{abs}\,N_i}\left[1 + \frac{1}{\eta_{LY}} + \frac{1}{\eta_{LY}}\left(\frac{1}{T_l} - 1\right) + \frac{1}{\eta_{LY}\,T_l}\,\frac{1}{\eta_{QE}} + \frac{1}{\eta_{LY}\,T_l\,\eta_{QE}}\,\frac{n_{eff}^2}{N_i}\right] . \qquad (1.4)$$

The last term is negligible for high fluxes, which is often the case for synchrotron radiation. Therefore, as reported in (4), the DQE for indirect X-ray detectors, configured with a thin film scintillator and microscope optics, can be estimated as:

$$DQE = \eta_{abs}\left[1 + \frac{1 + 1/\eta_{QE}}{\eta_{col}\,\eta_{LY}}\right]^{-1} . \qquad (1.5)$$

1.3.2 Dynamic Range

The dynamic range (DR) of a detector is generally defined as the saturation level of the detector divided by the noise level.
Imaging sensors in indirect detectors work in integration mode. The DR is limited by the full-well capacity and the noise. In the case of the Frelon camera, a CCD widely used for X-ray imaging at the ESRF, the noise is approximately 20 electrons/pixel/s and the full-well capacity is $3 \cdot 10^5$ electrons/pixel/s, leading to a dynamic range of 15000 gray levels, or 83.5 dB (16). The scientific CMOS pco.edge has a noise of 1.6 electrons/pixel/s and a full-well capacity of $3 \cdot 10^5$ electrons/pixel/s, hence, the DR is 85.4 dB. However, the dynamic range can be further reduced depending on the conditions for the experiment. For example, fast imaging increases the noise, due to the increase of the camera readout noise when used at high speed, and thus reduces the DR. Additionally, the dynamic range for indirect detection is depending heavily on the uniformity of the scintillator and its optical quality. For instance, in a region of the scintillator where the light emission is significantly higher compared to the average, the exposure time needs to be reduced to avoid saturation of the camera, leading to a reduction of the DR.
Since HPADs count every X-ray photon individually, they can be practically noise free if the energy threshold is properly set and the saturation is only limited by the readout dead time. The DR is, therefore, higher than for sensors working in integrating mode and does not depend on the experimental conditions.

1.3.3 Spatial resolution and Modulation Transfer Function

The ideal pixelized detector response to a point-like object is a Dirac function. Therefore, two separate objects are always discernible in the image. In a real detector the response to a point-like object is a broader distribution, known as the Point Spread Function (PSF). For two PSF to be discernible a minimum distance between the two point-objects has to exist. This minimum distance defines the spatial resolution limit, but there is a certain ambiguity in the degree of separation accepted as sufficient to distinguish two separate PSFs.
The concept of contrast removes this ambiguity. Considering two objects with the same

intensity, the contrast or modulation (M) is defined as

$$M = \frac{I_{Max} - I_{Min}}{I_{Max} + I_{Min}} , \tag{1.6}$$

where I^{Max} is the maximum intensity and I^{Min} the minimum intensity measured in between them (22). For example, when we say that a system has 1 μm spatial resolution, the value of the contrast for which the spatial resolution is defined and if the limit is determined by the camera pixel size should be specified.

The Modulation Transfer Function (MTF) describes the spatial response of a system completely since it includes both the concepts of resolution and contrast. It is defined as the ratio between the modulation of the image M^{image} and the modulation of the object M^{object} at different spatial frequencies ν:

$$MTF(\nu) = \frac{M^{image}(\nu)}{M^{object}(\nu)} . \tag{1.7}$$

Evaluation of the MTF

Three methods to evaluate the MTF will be described.

A first way to determine the MTF is to calculate the contrast in the image of a periodic grating made of X-ray absorbing and non-absorbing lines as displayed in figure 1.4. Compared to the resolution of the detector, a high enough spatial frequency causes the overlap of the intensity distributions of the images of different lines, thereby reducing the contrast. The MTF is the curve describing the measured contrast as a function of the spatial frequency of the periodic grating.

From a mathematical point of view, we can describe the MTF by first looking at the irradiance distribution g(x,y) of an image obtained with an optical system, which is as the convolution of the source distribution f(x,y) with the impulse response h(x,y):

$$g(x, y) = f(x, y) \otimes h(x, y) . \tag{1.8}$$

The impulse response h(x,y) is the smallest image detail that the system can form. When the source f(x,y) is an ideal point-source distribution, i.e. a two-dimensional Dirac delta function, the impulse response corresponds to the PSF of the system:

$$g(x, y) = h(x, y) \equiv PSF(x, y) . \tag{1.9}$$

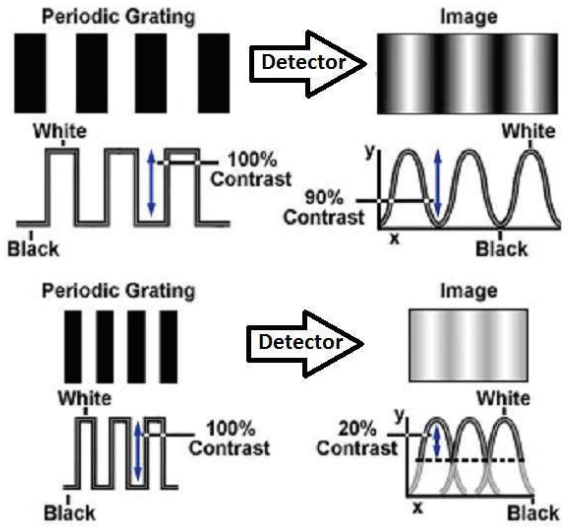

Figure 1.4: A Periodic grating is a series of objects separated by a finite distance. Their images are larger than the real object sizes due to the finite resolution of the detector. The images start to overlap when the distance between two objects is close to the spatial resolution limit, reducing the contrast.

Equations 1.8 describes the image formation in the spatial domain. Applying the Fourier transform $\mathscr{F}$ and using the convolution theorem, the convolution in the spatial domain becomes a multiplication in the frequency domain:

$$\mathscr{F}[\mathrm{g(x,y)}] = \mathscr{F}[\mathrm{f(x,y)} \otimes \mathrm{h(x,y)}] \,, \tag{1.10}$$

$$[\mathrm{G}(\xi,\eta)] = \mathrm{F}(\xi,\eta) \cdot \mathrm{H}(\xi,\eta) \,. \tag{1.11}$$

$\mathrm{F}(\xi,\eta)$, $\mathrm{G}(\xi,\eta)$ and $\mathrm{H}(\xi,\eta)$ are the Fourier transforms of f(x,y), g(x,y) and h(x,y) respectively.
$[\mathrm{H}(\xi,\eta)]$ is the optical transfer function (OTF), which is a complex function composed by a real part, the modulation transfer function MTF $= |\mathrm{H}(\xi,\eta)|$ and a complex part, the phase transfer function PTF $= \theta(\xi,\eta)$:

$$\mathrm{OTF} \equiv \mathrm{H}(\xi,\eta) = |\mathrm{H}(\xi,\eta)| \;\; \mathrm{e}^{[-\mathrm{j}\theta(\xi,\eta)]} \,. \tag{1.12}$$

Mathematically the MTF corresponds to the modulus of the Fourier transform of the PSF, which is obtained applying the Fourier transform in equation 1.9:

$$\mathrm{MTF}(\xi,\eta) = |\mathscr{F}[\mathrm{PSF(x,y)}]| \ . \tag{1.13}$$

Since the width of a function is inversely proportional to the width of its Fourier transform, a sharper PSF results in a broader MTF, which means that a larger range of spatial frequencies can be imaged with high contrast. The ideal detector MTF is a flat curve where the MTF is equal to 1 for every spatial frequency.
The second way to evaluate the MTF is hence from the Fourier transform of its PSF. The PSF can be measured by acquiring the image of a point object, i.e. a point-object with dimensions much smaller than the resolution of the system.

Alternatively, the MTF can be calculated from the Line Spread Function (LSF), obtained from a line-object which has one dimension much smaller than the PSF of the system while the other dimension is much bigger. The line-source is defined as a delta function along x and a constant along y:

$$\mathrm{f(x,y)} = \delta(\mathrm{x})\ \mathrm{C(y)} \ . \tag{1.14}$$

Following equation 1.8 and 1.9, the image g(x,y), i.e. the LSF, is a two dimensional convolution of the PSF:

$$\mathrm{g(x,y)} \equiv \mathrm{LSF(x)} = [\delta(\mathrm{x})\ \mathrm{C(y)}] \otimes \mathrm{PSF(x,y)} = \int \mathrm{PSF(x,y')dy'} \ . \tag{1.15}$$

The LSF hence only depends on the variable x. From the one-dimensional Fourier transform, we obtain the MTF:

$$\mathrm{MTF}(\xi,0) = |\mathscr{F}[\mathrm{LSF(x)}]| \ . \tag{1.16}$$

Compared to the PSF, the limitation of the LSF is that it provides information about the spatial resolution along only one direction, perpendicular to the length of the line-object. If the spatial resolution does not vary with the direction, the PSF is equal to the LSF, otherwise the LSF has to be measured in multiple directions.

Finally, a third way for the MTF evaluation is the slanted edge method (23, 24). The Edge Spread Function (ESF) is acquired as the image of a knife edge object. The ESF is described by a step function s along x and a constant along y:

$$\mathrm{f(x,y) = s(x)\ C(y)\ .} \tag{1.17}$$

Mathematically, we can obtain the LSF as:

$$LSF(x) = \frac{d}{dx} ESF(x)\ , \tag{1.18}$$

and therefore calculate the MTF. For more mathematical details, see (22).
The slanted edge method is widely used to characterize the response of imaging systems to hard X-rays since the fabrication of high frequency gratings with sufficient absorption is not trivial.

1.3.4 Frame rate

The detector's frame rate is the frequency at which consecutive images can be taken. It is defined as the inverse of the time needed to acquire the image and read the data, leading to an expression in frames per second (fps) or Hertz. Considering commercial products today the CMOS sensors can work at higher frame rate than HPADs, for the same number of pixels and dynamic range. For example, the PCO.dimax CMOS camera can record up to 7039 frames per second (1 Megapixel, 12-bit dynamic range), while the EIGER HPAD for the same conditions is limited at few hundreds Hz. To be able to exploit such a fast frame rate, a fast scintillator has to be selected. Because of the short decay time of Ce-doped scintillators, these crystals are normally preferred over Eu- or Tb-doped ones if fast imaging is required. Additionally, the integration time needed to acquire an image with enough signal has to be taken into account to evaluate the frame rate. The integration time can be reduced using a thicker scintillator, but this comes at the cost of a reduced spatial resolution.

1.4 Scintillators for X-ray area detectors

1.4.1 The physics of the scintillation process

The scintillation process in wide band gap materials can be divided into three steps: conversion, transport and luminescence (figure 1.5).

Firstly, in the conversion step, the X-ray photon interacts with the crystal lattice and transfers energy via the photoelectric effect and inelastic Compton scattering. This energy transfer creates a hot primary electron and deep hole, which are subsequently multiplied through a cascade of ionization processes (electron-electron inelastic scattering and Auger emission) which continues until their energy is too low to create further excitations. When the energy is below the forbidden gap E_g electrons and holes interact with phonons. This stage is called thermalization. The overall process leads to low energy electrons and holes located at the bottom of the conduction band and at the top of the valence band.

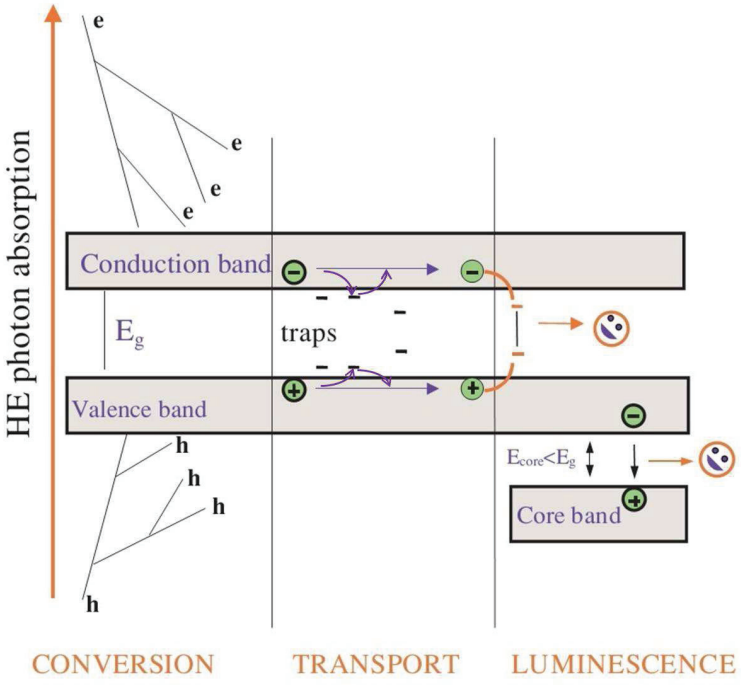

Figure 1.5: Scheme of the scintillation process in a wide band-gap material. The process is divided in three step: conversion, transport and luminescence (25).

Secondly, the thermalized electrons and holes are transferred to the luminescence centers. During the transport, electron and holes migrates through the material and due to the presence of defects, they may recombine through non radiative processes and be trapped and detrapped, leading to a delayed luminescence (afterglow).
Finally, the emission center is excited by the capture of a hole and an electron and ideally

returns to the ground state through a radiative process (luminescence). Alternatively, the emission center can return to the ground state through non-radiative processes.

1.4.2 Performance of the scintillators for X-ray area detectors

Some important parameters often considered in the scintillators characterization for area detectors are:

- the X-ray absorption efficiency,
- the light yield (LY),
- the timing performance, defined by the decay time and the afterglow,
- the emission wavelength, which has to match the camera's quantum efficiency,
- the linearity of the response with the X-ray energy and flux,
- the optical quality,
- the homogeneity of the response,
- the stability of the response,
- the properties of the substrate.

Figure 1.6 shows that the performance of the detector is affected by several scintillator properties.
The overall efficiency of the detector and its DQE depend on the absorption efficiency, the light yield, and the matching between scintillator emission spectra and the camera's quantum efficiency, as seen in equation 1.5.
The spatial resolution obtained using high-resolution detectors is ultimately limited by the light diffraction through the detector's optics and, therefore, depends on the emission wavelength of the scintillator. Additionally, the spatial resolution can be further degraded by the spread of the energy deposited in the scintillator and by the diffusion of light. As a consequence, the optical quality of the scintillator, and its stopping power also play a role in the spatial resolution. The type of scintillator (powder, single crystal, micro-structured) as well as the material have, therefore, a significant effect on the spatial resolution.
The speed of the detector is limited by the speed of the conversion process in the scintillator, i.e. the decay time. In addition, the speed of the detector is affected by the afterglow of the scintillator since a new image can only be taken when the afterglow of

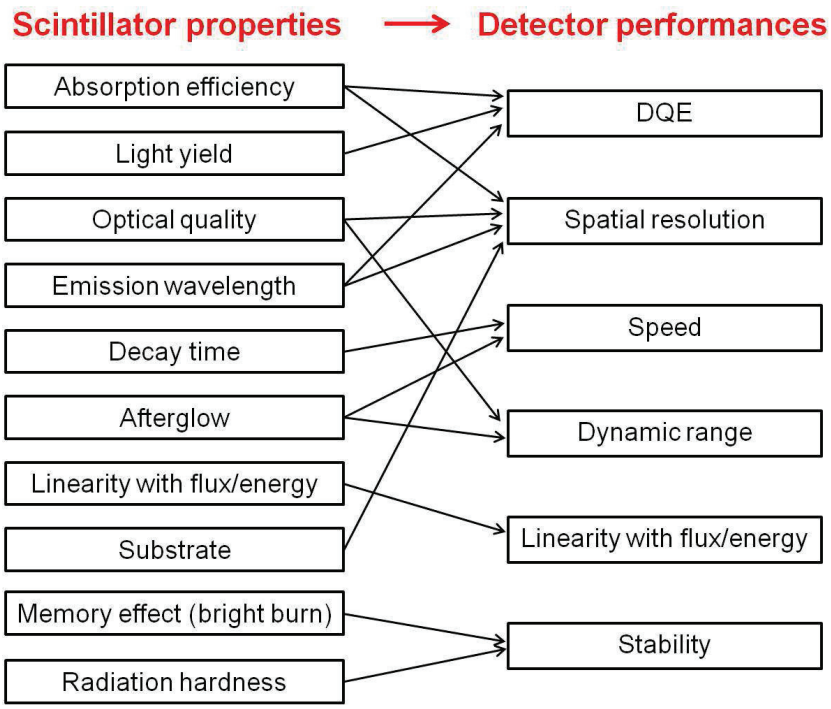

Figure 1.6: Dependence of the detector performances on the scintillator properties.

the previous image is reduced below the noise levels.

The afterglow as well as the optical quality also limit the dynamic range, reducing the number of exploitable signal levels of the camera sensor (see section 1.3.2).

Recently, the scintillator's linearity and stability are becoming a concern in X-ray imaging due to the demand of quantitative measurements. Therefore, a linear dependence of the detector's response on the X-ray photon flux and energy, as well as its stability after long exposures are required. These performances obviously depend in the first place on the linearity and stability of the scintillator. Variation of the light yield with the X-ray energy (non-proportionality) or during the exposure (radiation damage and memory effect) are therefore, becoming an important subject of research in the scintillators field (26, 27).

As last example, in the case of thin film scintillators on a substrate, the substrate can influence the performances of the scintillator. Firstly, the optical and crystalline quality of the substrate affects the quality of the film and, therefore, its imaging and scintillating properties. Secondly, any optical absorption of the photons from the film in the substrate reduces the scintillator's efficiency. Thirdly, light emission from the substrate

reduces the image quality that can be obtained. Lastly, X-ray fluorescence in the substrate degrades the spatial resolution. This final aspect is introduced in chapters 2 and 3.

1.4.3 Scintillators: materials and forms

The investigation of materials able to enhance the efficiency of X-ray detectors based on photographic films started immediately after the discovery of X-rays in 1895. The first optimized converter screens were made of $CdWO_4$ powder phosphors, which were already available in the beginning of the 20^{th} century. In the seventies more efficient oxysulfide materials were discovered (28). In particular Tb doped Gd_2O_2S, known as GOS or Gadox or P43, stood out for its high stopping power and light yield (29, 30). Today, different scintillator forms (single crystal, transparent ceramic, and structured scintillators) and different materials which outperform Gadox powder phosphors in many fields have been developed. However, Gadox screens are still widely used in medical and security applications, mainly because they can be produced as large area sheets at relatively low cost. Since powder screens are made of a grained phosphor mixed with a binding agent, the emitted light spreads in every direction due to scattering at the grain surfaces (see figure 1.7(a)). If the screen thickness increases, the spatial resolution decreases since the light is scattered by more grains before exiting the screen. In fact, the spatial resolution is approximately equal to the thickness of the scintillator (31).

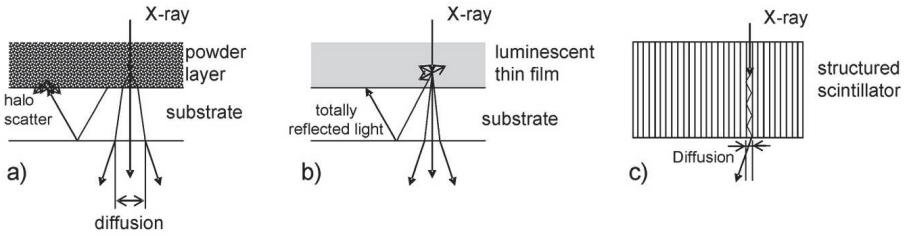

Figure 1.7: Light is transmitted differently depending on the structure of the scintillator. (a) In powder scintillators it is scattered at the grains boundaries, resulting in a spreading of the light distribution and a degradation of the spatial resolution. Transparent ceramic scintillators are affected by a similar phenomenon. (b) In single crystals, the light travels up to the surface without being scattered. Only the fraction of light below the critical angle can exit the scintillator. (c) Structured scintillators act as a light guide, enhancing the light collection outside the scintillator (32).

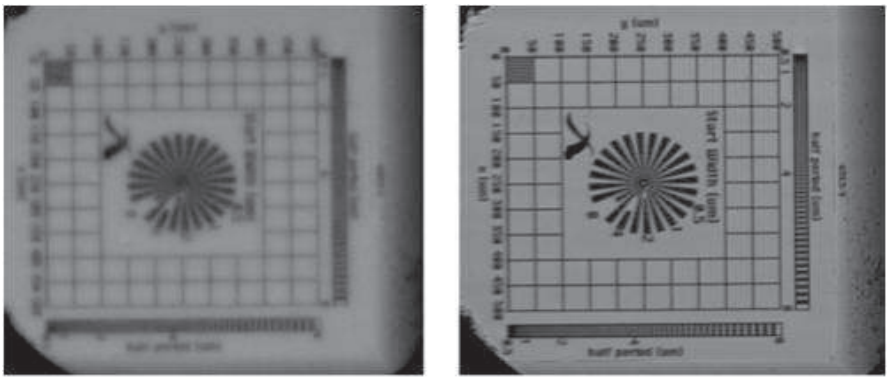

(a) Gadox powder 5µm (b) LSO:Tb SCF 48µm

Figure 1.8: Comparison between the image of an X-radia resolution chart obtained using a 5 μm Gadox powder scintillator and a thicker single crystal LSO:Tb scintillator (38).

Single crystal scintillators have higher densities and, therefore, higher absorption efficiencies than powder phosphors, for which the filling factor is approximately 50%. Additionally, since the light is not scattered inside the scintillator, compared to powder phosphors a better spatial resolution and contrast can be obtained for the same film thickness (figure 1.7). A comparison between an image obtained with a powder phosphor and a single crystal film is shown in figure 1.8.

A disadvantage of single crystal scintillators is their total internal reflection which lowers the fraction of light able to exit at the surface and thus reduces the light to be collected. The light collection can be enhanced by surface treatments which increase the roughness, but they as a consequence also degrade the resolution. The first materials to be developed as single crystals were NaI:Tl and CsI:Tl in the late nineteen-forties (33) after which many other materials followed. For example, to improve the absorption efficiency, research focused on materials with high density and high-effective Z-number. This resulted in, amongst others, Ce-doped LSO (Lu_2SiO_5), LYSO ($Lu_xY_{1-x}SiO_5$) and GSO(Gd_2SiO_5) (34, 35). It is worth noting that many efforts have been made in the development of the technologies to produce lutetium oxide (Lu_2O_3), one of the most dense known phosphors (30). This material shows good luminescence properties when doped with Eu or Tb activators, but the growth of single crystal Lu_2O_3 presents many problems due to its high melting point, above 2400 °C. However, progresses has been reported (36, 37).

Transparent ceramic scintillators are polycrystalline materials made of tight randomly

oriented micro grains. Compared with their single crystal scintillator counterparts, the density is almost as high, the cost is inferior and larger samples can be produced. Many cubic materials can be prepared as transparent ceramic and they show good homogeneity, as it is reported for Ce or Nd-doped YAG ($Y_3Al_5O_12$) or Lu_2O_3:Eu (39, 40). A disadvantage of ceramic scintillators is the degradation of the spatial resolution due to the scattering at the grain boundaries, as is also the case for the powder phosphors. Grain boundaries may also contain excessive amounts of defects leading to traps and thus afterglow.

The so-called structured scintillators are made of pillars (figure 1.7(c)) that act as a light guide. CsI:Tl and CsI:Na for example, can be prepared with this structure. In the case of medical applications, structured scintillators are coupled directly to the photodiode. Many pillars are coupled to the same pixel and the ultimate spatial resolution limit is the photodiode pixel size. For high-resolution detectors, even if the camera's pixel size is reduced well below the light diffraction limit using microscope optics, the diameter of the pillar is the detector's ultimate spatial resolution limit. Nevertheless, because of the optical waveguide properties, the resolution, remains constant for increasing film thicknesses, while the absorption efficiency is higher. Additionally, light collection from structured scintillators is more efficient compared to collection from single crystals, because less light undergoes total internal reflection at the exit surface. Today the minimum diameter of the pillars is a few micrometers, and hence they are not suitable for sub-micrometer spatial resolution imaging. Films made of sub-micrometer diameter Lu_2O_3 pillars are currently under development, but they are not sufficiently homogeneous yet (41). In figure 1.9, a comparison between an image obtained using a sub-micron structured Lu_2O_3:Eu film from RMD and a GGG single crystal film is reported. In the inserts the flat field images are shown. In the case of the micro-structured scintillator, some inhomogeneities result in bright spots, which saturate the sensor and thus reduce the dynamic range of the detector. In addition, even if the exposure time is chosen so that these bright spots are not saturated, they are not completely eliminated through a flat-field correction.

A summary of the resolution limits for X-ray imaging using different kinds of screens is reported in figure 1.10. Today, single crystals are still the only viable solution for sub-micrometer spatial resolution X-ray area detectors. Their thickness must match the depth of field of the microscope optics, otherwise the resolution is degraded. The use

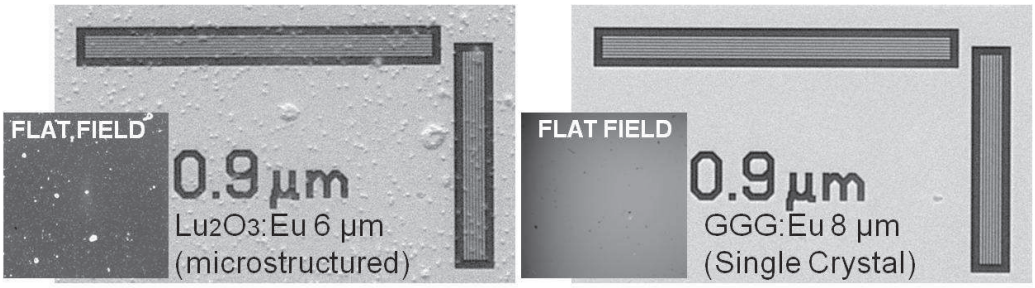

Figure 1.9: Comparison between the image of a grid pattern (detail size 0.9 μm) obtained with (left) a sub-micrometer structured 6 μm thick Lu_2O_3:Eu scintillator and (right) a single crystal 8 μm thick GGG:Eu scintillator. In the inserts the flat field images are reported.

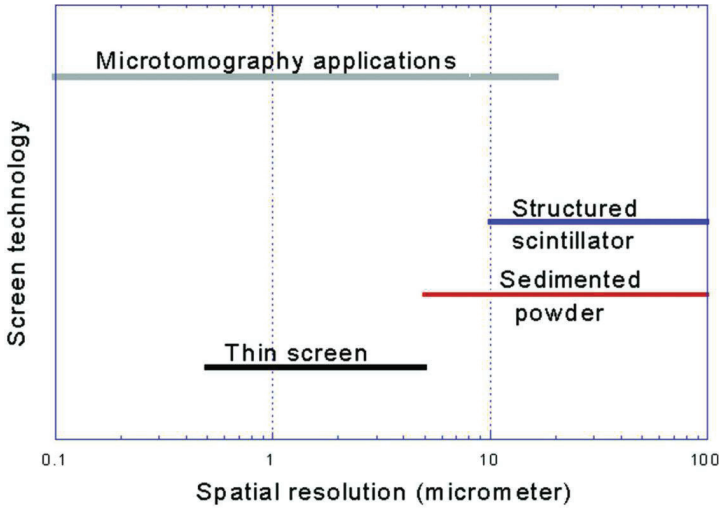

Figure 1.10: Scintillator requirements for high-resolution detectors (32).

of structured scintillators is currently still limited for applications that do not require resolutions below several micrometers. The main advantage of structured scintillators is the light guide effect, which allows the use of a thicker screen without significantly reducing the spatial resolution. For this reason structured scintillators are good candidates for hard X-ray imaging.

Compared to single crystals, the use of powder phosphors and transparent ceramics reduces the obtainable resolution due to the light scattering on the grain boundaries. Sub-micrometer resolution can not be obtained with these technologies. The main advantages of powder phosphors are the low cost and the possibility to fabricate materials

that can not be grown as single crystals. Currently however, transparent ceramics are sometimes superseding powder phosphors because of their higher absorption efficiency.

1.4.4 Single crystal thin film scintillators for micro tomography

Currently only single crystal scintillators have been able to successfully reach spatial resolutions of 1 μm or below with uniform image quality, in X-ray area detectors. Due to the limited depth of field of the microscope optics used to magnify the visible image, the scintillator's thickness has to be within 1 and 20 μm.
Different techniques have been investigated to deposit or grow thin film scintillators on a substrate. Molecular beam epitaxy (MBE) was used for example to deposit rare-earth trifluoride scintillators on silicon substrates (42), while Eu-doped Lu_2O_3 and Gd_2O_3 were obtained using sol-gel coating (SGC) and Pulsed Laser Deposition (PLD) on amorphous carbon and SiO_2/Si substrates (43). The main drawback of the aforementioned techniques is the maximum thickness of the obtained films, which is of the order of hundreds of nanometers for good optical quality films.
So far only the liquid phase epitaxy technique (LPE) (44, 45), i.e. the growth on a substrate from a super cooled melt solution, was successfully applied to grow several micrometer thick scintillating films with high optical quality. The LPE growth process was optimized for different scintillating materials and is today used to produce the state-of-the-art SCFs used for high-resolution imaging at synchrotrons (2, 3).
Alternatively, thin single crystal scintillators can be produced thinning a bulk crystal by the mechanical-chemical polishing method (46). The use of a bulk crystal presents some advantages. No contaminations from the melt enter in the film and polishing does not require a specific substrate. Some drawbacks are, however, present. Firstly, the minimum thickness that can be obtained is limited. Free-standing crystals can be thinned down to approximately 20-25 μm while crystals glued on a substrate are limited to a thickness between 5 and 10 μm. The depth of field of a microscope objective with a numerical aperture higher than 0.6 is less than 1 μm. Consequently, combining a 10 μm thick SCF with high numerical aperture optics will degrade the spatial resolution because of the defocused image. Additionally, not every material can be polished down to 10-20 μm. Today, the polishing process is well optimized only for YAG and LuAG crystals. Secondly, due to the high temperature, an oxygen-free atmosphere is required for bulk growth and the scintillators polished from bulk crystals often present some

anti-site defects and oxygen vacancies, which lead to the presence of a slow component in the luminescence (afterglow)(47).

Scintillating screens down to hundreds of nanometers can be produced using the LPE technique which is, in addition, not limited to small sample areas. Next to that, for some materials, LPE films show fewer structural defects compared to bulk crystals. This is caused by the lower growth temperature and leads to a reduction of the afterglow. This effect has been reported for example for $Lu_3Al_5O_{12}$ (LuAG) and for some aluminum perovskites (48, 49). Moreover, using the LPE technique, the dopant concentration can be precisely tuned to maximize the conversion efficiency and the dopant concentration in the film is very homogeneous.

LPE also presents some drawbacks. Firstly, some unwanted impurities from the flux used for the LPE growth can enter in the film. Depending on the nature of these impurities, the quality and the scintillation properties of the film can be degraded. Tous et al. (50) as well as Zorenko et al. (51) have studied the effect of different fluxes on garnet SCFs. The films obtained with a BaO-based flux show better conversion efficiency with respect to the films obtained using a PbO-based flux. However, when a BaO-based flux is used, the optical quality and surface morphology are not as good as compared to a PbO-based flux. Secondly, LPE requires the availability of a non luminescent substrate with the same crystalline structure and low lattice mismatch compared to the film.

The first commercially available single crystal thin films for imaging were YAG:Ce ($Y_3Al_5O_{12} : Eu$) and LuAG:Eu ($Lu_3Al_5O_{12} : Eu$) on undoped YAG substrates. Thereafter, the technology to produce GGG:Eu ($Gd_3Ga_5O_{12} : Eu$) on GGG substrates was developed at the CEA (Commissariat à l'énergie atomique et aux énergies alternatives) which was followed by the development of GGG:Tb ($Gd_3Ga_5O_{12} : Tb$) at the ESRF(2). LSO:Tb ($Lu_2SiO_5 : Tb$) was developed during the ScintTax project, an european collaboration for the development of new thin film scintillators (3). LSO:Tb SCFs are grown on YbSO or LYSO:Ce substrates. In the case of LYSO:Ce, an optical filter has to be used to cut the Ce luminescence from the substrate.

LSO:Tb and GGG:Eu are today the state-of-the-art scintillators used at synchrotrons for sub-micrometer spatial resolution detectors. At the ESRF, a laboratory for the LPE based production of LSO:Tb, GGG:Eu and GGG:Tb SCFs scintillators has been operational since 2010. The customers are mainly the ESRF imaging beamlines, other synchrotrons and a few companies. Next to the production activity, other materials

have been recently under investigation: Ce-doped materials to exploit the faster decay time (52), UV-emitting materials, to increase the resolution limit due to light diffraction, aluminum perovskite (53) and lutetium oxide scintillators, of which the results are presented in chapters 4, 5 and 6 of this work, to improve the stopping power at high energies.

Chapter 2

Modelling of the scintillator's spatial response

2.1 Introduction

High spatial resolution detectors used at synchrotrons exploit single crystal thin films. Few scintillating materials are today available in this form, mainly because of the high development and production cost as well as the small market. LuAG:Ce and YAG:Ce bulk scintillators polished down to a few micrometers are produced by Crytur, while LSO:Tb, GGG:Tb and GGG:Eu are grown on a substrate by liquid phase epitaxy at the ESRF. New scintillators optimized for various applications are required, as for example fast scintillators with low afterglow for time resolved micro-tomography or denser materials to improve the spatial resolution at high X-ray energies. The light yield and the afterglow are the most difficult parameters to predict when developing a new scintillator, since these parameters often depends on the technique which is used to produce the scintillator. On the contrary, the distribution of the energy deposited by X-ray photons in the scintillator, which limits the spatial resolution at high energy, can be accurately predicted down to a sub-micrometer scale thanks to the advancements of Monte Carlo (MC) techniques. A model to evaluate the detector's Modulation Transfer Function (MTF) and guide the development of new scintillating materials is presented in the next two chapters.

2.2 A mixed approach to simulate indirect detection

The detectors used for X-ray micro-imaging at synchrotrons are based on indirect detection, and can schematically be composed of three parts:

- A scintillator, which absorbs the X-rays and converts the energy into a visible image;
- Microscope optics, eventually combined with an eyepiece, which magnify the visible image and project it onto the imaging camera;
- A 2D imaging camera (i.e. a CCD or a CMOS) that converts the visible image into an electronic digital signal.

Depending on the configuration of the detector and on the conditions of the experiment, a combination of different phenomena can limit the spatial resolution and the contrast of the image. These phenomena are:

- **Scintillator response.** When an X-ray photon interacts with a material, it can be deflected (elastic or inelastic scattering) and generate secondary X-rays or electrons through atomic ionization. These electrons can relax through X-ray fluorescence and Auger emission. Consequently a fraction of the incoming energy spreads from the initial interaction position. In applications which demand micrometer and sub-micrometer spatial resolution, this energy spread is non-negligible.
- **Light diffraction.** When a wave (i.e. the visible light emitted by the scintillator) goes through an aperture (i.e. the microscope optics) diffraction occurs. The best focal spot that can be obtained, and consequently the highest spatial resolution that can be achieved, depends on the size of the diffraction pattern after the aperture. The spatial resolution of a diffraction-limited system depends on the numerical aperture and the wavelength of the light.
- **Out-of-focus light.** If the thickness of the image source along the optical axis (here corresponding to the thickness of the scintillator) is larger than the depth of field (DoF) of the microscope optics, part of the light is projected as a defocused image on the camera and degrades the quality of the recorded image. Using a

scintillator which is thicker than the DoF, therefore, results in a system that is not diffraction limited.

- **Camera resolution.** According to the Nyquist-Shannon sampling theorem (54, 55), the highest spatial resolution achievable with a 2D camera is approximately twice the pixel size. Since the visible image is magnified (or demagnified) in the case of an indirect detector, an estimate of the spatial resolution limit due to the camera is determined by dividing the camera's pixel size by the optical magnification or demagnification.

The main goal of the calculations presented in chapters 2 and 3 is to estimate the MTF of the detector as a function of the combination of the scintillator (composition and thickness) with the microscope optics (numerical aperture), in the case of optical magnification, i.e. the camera pixel size is reduced below the light diffraction limit.
The model we developed includes Monte Carlo and analytical calculations. The first enables to determine the scintillator response and the latter estimates the effects of diffraction and out-of-focus light. We assume to be in a configuration where the camera does not influence the spatial resolution, which is the case when the pixel size is approximately half of the diffraction limit or smaller.
Nevertheless, the bottleneck of the experiment is not always the spatial resolution. It could be, for example, the speed (e.g. time-resolved experiment) or the maximum allowed dose on the sample (e.g. biological samples). Sometimes, it is more convenient to magnify the X-ray image and reduce the detector's spatial resolution, choosing a configuration which optimizes other properties. Hence, the assumption regarding the pixel size of the camera may not be valid and the choice of the scintillator is based on different criteria (e.g. the best DQE, the shortest decay time, the lowest afterglow, the highest light yield).
Hence, we focus here on the configurations demanding micrometer to sub-micrometer resolution, and we neglect the imaging camera by assuming that its spatial resolution is always well below the diffraction limit and thus not a limiting factor.
An overall scheme of the model is reported in figure 2.1. The Monte Carlo code, based on the Geant4 (G4) Monte Carlo toolkit (56) simulates an X-ray pencil beam impinging on the scintillator. The scintillator is made of a thin scintillating film deposited on a non-scintillating substrate. When a photon interacts with the scintillator or with

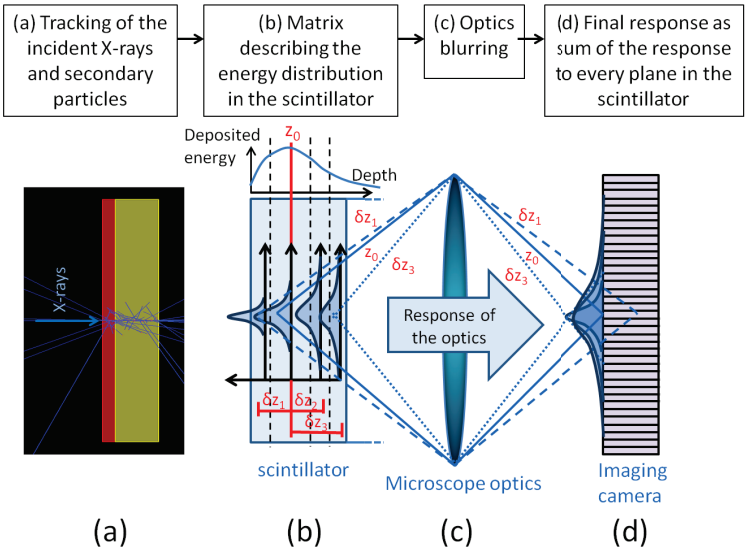

Figure 2.1: Overall scheme of the simulation principles. The scintillator response is calculated by Monte Carlo simulations (G4), which gives the energy distribution in the material. Afterwards, the output of the Monte Carlo calculation is used as input for analytical calculations, which keep into account the microscope optics blurring.

the substrate, it can change momentum, deposit energy, or, if the energy is above a certain threshold, it can generate secondary electrons or X-rays. The primary X-ray photons as well as the secondary particles are tracked down to zero energy. A snapshot of a short Geant4 simulation is reported in figure 2.1(a). The output of the Monte Carlo simulations is a tridimensional matrix which describes the energy distribution deposited in the scintillator. The LSF and MTF at every depth in the scintillator, as well as the curve describing the energy deposited as a function of the depth ($E_{dep}(z)$), are calculated from MC (fig.2.1(b)). The optics are included following the analytical approach of H. H. Hopkins (57), who describes the response of an aberration-free system to a defocused point source. For a given numerical aperture NA and light wavelength λ, a matrix describing the MTF response of an optical system as a function of the distance δz from the focal plane is calculated (fig.2.1(c)). The results are combined: every slice in the depth of the scintillator acts as a light image source, blurred by the optics as a function of the defect of focus δz and of the light diffraction. The final response of the full detector is calculated as the sum of the images projected on the camera from every depth z of the scintillator (fig.2.1(d)). The position of the focal plane z_0 has been

selected by maximizing the MTF of the full detector.

2.3 Monte Carlo Geant4 toolkit

Monte Carlo refers to a broad class of algorithms that use random sampling to find a quantitative solution to a problem. The method is widely applied in many fields (physics, finance, engineering, etc.) to solve problems not trivial to study with other techniques. The development of the Monte Carlo methods started in the 1940s as part of the *Manhattan project* at the *Los Alamos National Laboratory* and since then knew a fast development thanks to the increase of computing power.
Geant4 (56, 58) is a Monte Carlo toolkit developed at the *European Organization for Nuclear Research* (CERN) to simulate the tracking of particles generated in high-energy experiments. Afterwards, it was extended to include low energy physics (down to 250 eV) and it is now widely used for different applications: not only nuclear physics but also astrophysics, medical physics, radio-protection, etc. The first Geant4 version was released in 1998; since then, many updates were released and a team of around one hundred scientists from all over the world works on its development and maintenance. Every user can freely access the whole code, but modifications of the core part of the software are not recommended.
Since Geant4 is written in the C++ programming language, its object oriented nature allows the user to customize and extend the tool building his own application upon an existing framework. Additionally, the structure is modular and allows the user to load only the components needed for the application.
The application that is presented here has been developed using the version Geant4.9.6.

2.3.1 Our Geant4 application

Different classes have been implemented to develop the application: three mandatory classes describing the geometry and materials (*G4VUserDetectorConstruction*), the physical model (*G4VPhysicsList*) and the primary particles generator (*G4VPrimaryGenerator*). Note that several other classes were used to define the scorers needed to extract the energy distribution and the other quantities of interest.
The geometry of the simulation, as well as the axis convention that will be used in the rest of the discussion, is shown in figure 2.2. The scintillator is defined as a rectangular

box of thickness t_S and a lateral size of 1.4 cm, free standing or lying on a second 150 μm thick box representing the substrate. The scintillator has a surface normal along the z-axis. A one-dimensional X-ray pencil beam distributed along the y direction hits the scintillator orthogonally to its surface. Every primary X-ray and the secondary particles generated in the cascade are tracked individually down to zero energy.

Due to the broad range of applications covered by Geant4, different physical models were developed and validated for different conditions. For the here described application, the low energy Livermore model has been selected, which has been validated for electrons and X-ray or gamma photons in the energy range from 250 eV to 1 GeV (59, 60). The production threshold for the secondary particles was set to 250 eV. Note that the limit of 250 eV is not critical for our model since we are studying a diffraction-limited resolution, which is larger than the attenuation length of electrons at 250 eV.

The materials used for the scintillator and the substrate are defined by the density and the elemental stoichiometry. Depending on these two parameters the software assumes that a particle traveling in the material has a certain probability to interact with a specific kind of atom, while the concepts of crystal and electronic band structure as well as phonons are not included. The list of all the materials used for the calculations are summarized in table 2.1.

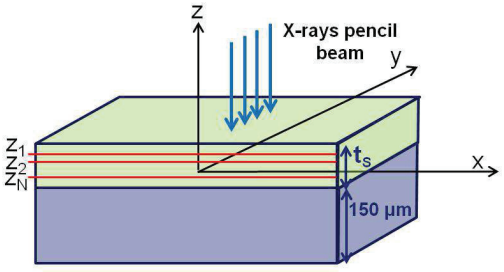

Figure 2.2: Geometry and axis convention in the Geant4 application.

Once the geometry, the physical model and the primary particle generator have been defined, the Geant4 application is ready to run. However, the simulation runs silently, meaning that the software does not keep track of every single step. Integrated quantities need to be calculated while the simulation runs to get useful output. Hence a *sensitive detector* (i.e. a scorer implemented inheriting from the class *G4VSensitiveDetector*) has been coupled to the scintillator, meaning every time a particle moves a step in the scintillator this scorer is called by the software. The sensitive detector defines a tridimensional matrix in the scintillator, calculates the bin associated with the position of the step and increments a counter associated with the bin. Different counters can be incremented simultaneously. A first one accumulates the energy deposited in every

Table 2.1: Materials and their used names, chemical formula and single crystal densities used in the Geant4 simulations (AP = aluminum perovskite, G = garnet)

name	short name	chemical formula	density [g/cm^3]
Yttrium AP	YAP	$YAlO_3$	5.35 (61)
Gadolinium AP	GdAP	$GdAlO_3$	7.50 (62)
Lutetium AP	LuAP	$LuAlO_3$	8.40 (61)
Gadolinium lutetium AP	GdLuAP	$Gd_{0.5}Lu_{0.5}AlO_3$	8.00
Lutetium orthosilicate	LSO	Lu_2SiO_5	7.40 (63)
Ytterbium orthosilicate	YbSO	Yb_2SiO_5	7.40
Gadolinium gallium G	GGG	$Gd_3Ga_3O_{12}$	7.10 (64)
Lutetium oxide	Lu_2O_3	Lu_2O_3	9.50 (65)
Yttrium aluminum G	YAG	$Y_3Al_5O_{12}$	4.55 (66)
Gadolinium aluminum G	GdAG	$Gd_3Al_5O_{12}$	5.97 (66)
Lutetium aluminum G	LuAG	$Lu_3Al_5O_{12}$	6.73 (66)
Cesium iodide	CsI	CsI	4.51 (67)

bin to obtain the energy distribution in the scintillator, which corresponds, considering the whole detector system, to the light source distribution projected through the optics. At the same time other counters can be coupled to the scintillator (or the substrate) to calculate for example the energy deposited by a single kind of particle (e.g. only electrons), by a specific phenomenon (e.g. only Compton scattering), or to count the number of interactions, the number of secondary particles, etc.

Due to the symmetry of the geometry, in the y-direction a single bin has been considered. We can therefore, describe the output of the simulation as a two dimensional matrix M_{G4} where every line is a LSF curve calculated at a different depth z_j in the scintillator (figure 2.3(a)). From M_{G4} different results can be extracted: the matrix of the MTF curves as function of the z coordinate (fig.2.3(b)), the total LSF and the total MTF of the scintillator (without any consideration of the optical effects), the energy deposited in the scintillator as function of z, etc.

The size of the bins is 0.1 μm in the x direction and 0.2 μm in the z direction. The bin sizes have been selected as a compromise between resolution and noise: increasing the bin size will degrade the MTF and decreasing it requires more statistics (i.e. longer computational time).

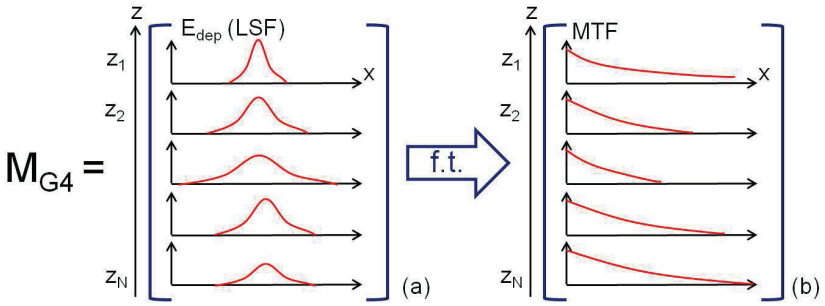

Figure 2.3: Geant4 output: the energy distribution in the scintillator is a matrix where each line corresponds to the LSF calculated at a specific z in the depth of the scintillator (a). The matrix of the MTFs calculated at every depth z can be calculated by the Fourier transform of the LSF(b).

2.4 Results

2.4.1 Material and X-ray energy dependence

The Modulation Transfer Function (MTF)

The effect of the X-ray energy (between 5 and 80 keV) on the energy distribution has been studied for various scintillators with a thickness of 5 μm. In figure 2.4 the PSF and MTF curves for different X-ray energies and various scintillators are reported. The results are shown for the state-of-the-art thin film scintillators (a LSO film on an YbSO substrate and a GGG film on a GGG substrate) and for two candidate materials to be developed (a Lu_2O_3 film on a Lu_2O_3 substrate and a GdAP film on a YAP substrate). The simulated substrates correspond to the ones that are actually used for the SCFs. Undoped GGG is relatively easy to produce as a bulk single crystal (SC) bulk and is commercially available as a substrate. It is therefore, ideal for Eu-doped GGG film growth, since the film-substrate lattice mismatch is close to zero. A drawback is the luminescence of the substrate due to elemental contaminations which can vary depending on the lot and on the supplier. LSO:Tb films are grown on YbSO or LYSO:Ce substrates. YbSO was developed specifically for LSO film growth and has no emission in the visible range. The drawback of YbSO is that it is only produced in small quantities and that it is expensive. Alternatively, LSO:Tb films are grown on LYSO:Ce bulk SCs, which are widely available since they are used themselves as scintillators. In this case, the cerium visible emission has to be suppressed using an optical filter. Undoped YAP

single crystals are available and relatively cheap. The crystal structure is the same as GdAP, LuAP and GdLuAP and the lattice mismatch can be reduced by optimizing the Gd/Lu ratio, as presented in chapter 4. Also in this case, an emission which varies with the supplier and with the lot is observed, and has to be suppressed using optical filters. Lu_2O_3 bulk SCs are difficult to grow, but many progress has been made recently. Substrates are starting to be available, although the crystalline and optical quality are not fully optimized.

At low energy (15 keV, figure 2.4(a)) no significant differences among the response of LSO, GGG, GdAP and Lu_2O_3 scintillators are observed, but these materials all present high density, from GGG with a density of 7.1 g/cm^3 up to Lu_2O_3 with a density of 9.4 g/cm^3. As comparison the CsI scintillator which has a density of 4.5 g/cm^3, has also been reported in figure 2.4(a). It shows a broader PSF and a contrast in the MTF at least 10% worse than the other denser considered materials, for spatial frequencies above 500 lp/mm.

At 20 keV (figure 2.4(b)), the MTFs are lower than at 15 keV. Additionally, the curve obtained for GdAP presents a sharp decrease at the low spatial frequencies which, compared with the other investigated materials, leads to a contrast reduction of $\approx 20\%$. No significant difference is observed in the width of the central peak of the PSF, but significantly higher tails appear in the PSF calculated from GdAP. These tails are not due to the scintillating film itself, but due to the yttrium X-ray fluorescence produced in the substrate that interacts with the scintillator and creates an offset in the PSF. Similar tails are visible for a GGG film on GGG substrate in figure 2.4(a) and 2.4(b), caused in this case by the gallium K-edge at 10.4 keV. To confirm that the reduction of the contrast is due to the substrate, the results for 5 μm free-standing GdAP and GGG are also plotted in fig 2.4(b), in blue and red dashed lines respectively. Compared with GdAP on YAP and GGG on GGG (blue and red continuous lines respectively) no offsets in the PSFs and no low-frequency drops for the MTFs are observed. The contrast degradation due to the substrate is smaller for a GGG substrate than a YAP one, due to the lower fluorescence yield of gallium compared to yttrium. Although the atomic density of gallium in GGG is higher than the one of Y in YAP ($2.11 \cdot 10^{22}\ Ga_{atoms}/cm^3$ vs $1.97 \cdot 10^{22}\ Y_{atoms}/cm^3$, the fluorescence yield for the K-shell (ω_K) sharply increases with the atomic number Z in the range Z=20 to Z=40 ($Ga_{\omega_K} \approx 0.45$ vs. $Y_{\omega_K} \approx 0.7$). Since the absorption efficiency is approximately the same at 20 keV, the number of

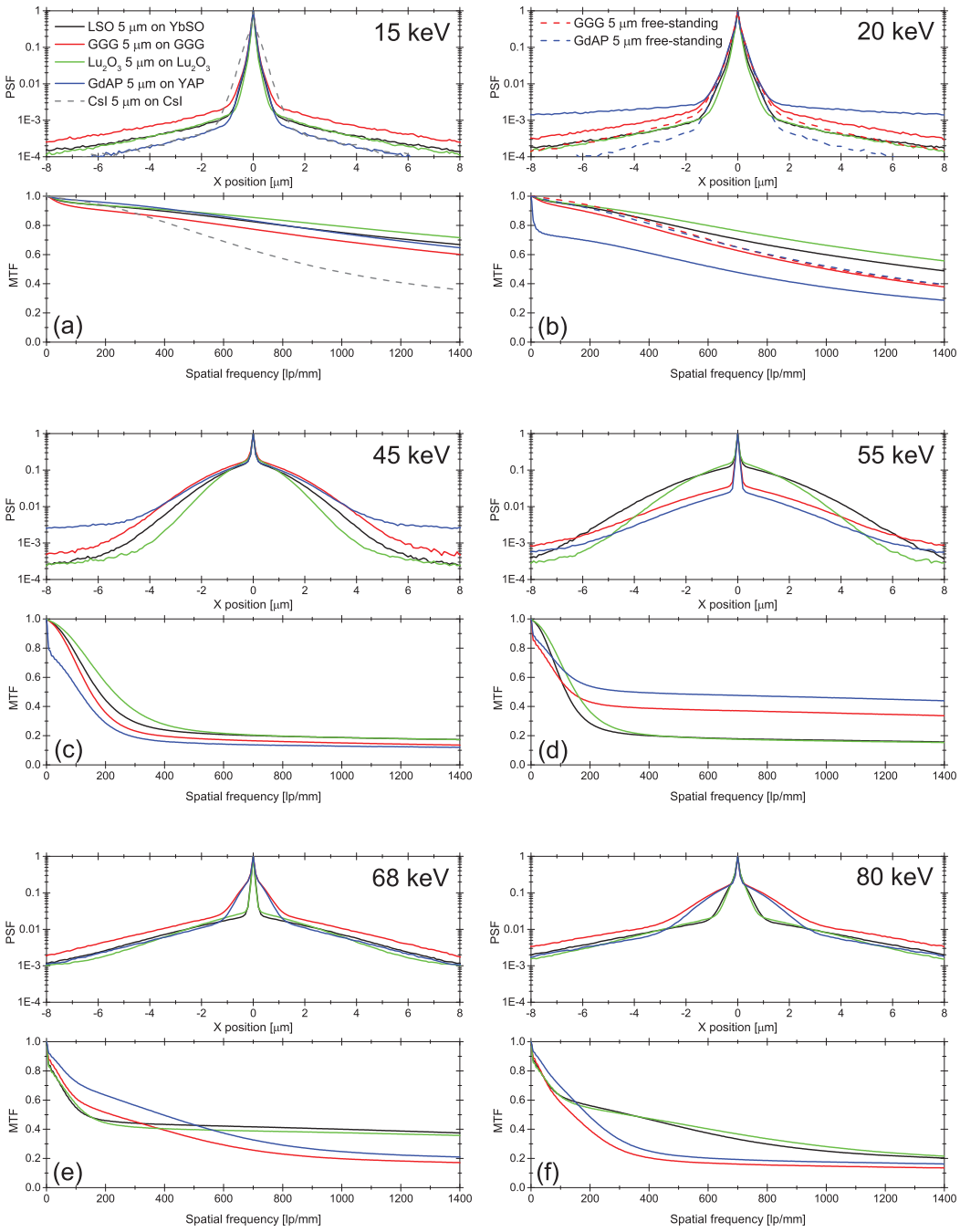

Figure 2.4: PSFs and MTFs calculated from the simulation of the deposited energy in a 5 μm thick scintillator by a 1D X-ray source. The scintillator is supported by a 150 μm thick substrate. The scintillator and substrate materials, as well as the X-ray energies, are indicated in the figures.

X-ray fluorescence photons produced in YAP can be thus roughly estimated to equal 1.5 times the number of the ones produced in GGG.

By increasing the X-ray energy the PSFs become broader and the MTFs are degraded. The calculated contrast at 500 lp/mm decreases from 85 % at 20 keV to 25 % at 45 keV for Lu_2O_3 and from 57 % to 17 % for GdAP (figure 2.4(c)). At the same time, a significant broadening of the PSFs is observed. However, once the energy is above the K-edge of the high-z element contained in the scintillator, a higher contrast is obtained. For example at 55 keV, approximately 5 keV above the gadolinium K-edge, the contrast of GdAP at 500 lp/mm goes up to 50 % and the PSF broadening is less significant (fig.2.4(d)). Similarly, the contrast calculated for Lu_2O_3 at 500 lp/mm increases from 20 % at 55 keV up to 40 % at 68 keV (fig.2.4(e)).

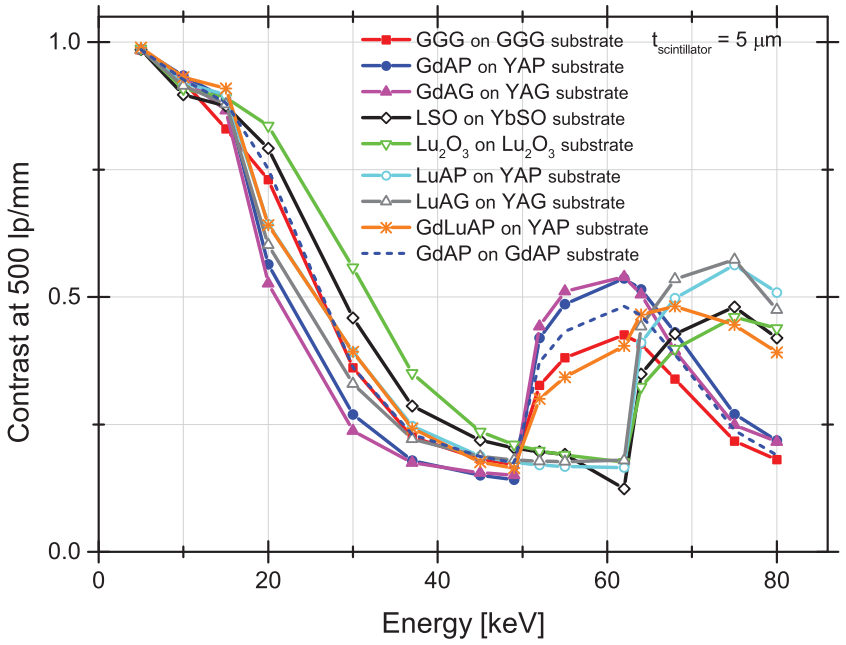

Figure 2.5: Contrast at 500 lp/mm as a function of the incident X-ray energy, for different scintillators. The values are extracted from the MTFs calculated using the MC model. The thickness of the scintillating film and substrate are 5 and 150 μm, respectively.

To summarize the results obtained as a function of the X-ray energy and the material, the value of the MTF at 500 lp/mm (1 μm resolution), is reported in figure 2.5 for the

different scintillators. Lutetium and mixed gadolinium-lutetium aluminum perovskite, as well as lutetium and gadolinium aluminum garnets have been added for comparison in addition to the materials already discussed above. GdAP on GdAP is shown to illustrate the effect of a different substrate compared to GdAP on YAP. We can divide the considered energy range in few intervals, where different phenomena play the crucial role and different scintillators show the best spatial response.

At low X-ray energy, below the yttrium K-edge (**5-17 keV**) the considered materials, which all have a density above 7 g/cm^3, show high contrast (more than 80 % at 500 lp/mm). Between 10 and 17 keV the GGG SCFs are slightly less performant due to gallium fluorescence.

In the energy range between the Y and Gd K-edge (**17-50 keV**), the contrast calculated for materials on Y-based substrates (i.e. YAP and YAG substrates) is 15-35 % lower compared to the values obtained for scintillators on yttrium-free substrates (i.e. Lu_2O_3 and LSO SCFs). The effect is caused by the fluorescence of the substrate which is partly reabsorbed in the SCF. As a reference, the results are compared for GdAP, both on YAP and GdAP substrates (continuous and dashed blue lines respectively). The contrast at 20 keV is 56 % for GdAP on YAP and 75 % for GdAP on GdAP.

In the energy range **50-80 keV** the major role is played by the Gd K-edge and the Lu K-edge. Gd based materials show higher contrast in the 52-65 keV range, Lu-based ones in the 65-80 keV range, while GdLuAP shows a flatter response as a function of the energy and could compete in terms of contrast both with GGG and LSO state-of-the-art thin film scintillators. Once again the substrate plays an important role due to the fluorescence photons which reduce the contrast at low frequencies. YAP and YAG substrates have a lower absorption at high-energy and a lower fluorescence rate compared to the Lu_2O_3, GGG and YbSO ones. Consequently, the scintillators on Y based substrates show better contrast compared with the other investigated materials because of the lower number of fluorescence photons produced in the substrate. In this case the contrast for GdAP SCFs is higher when a YAP substrate is selected over a GdAP one (54 % vs. 48 % at 62 keV).

Considering these results, it should be kept in mind that the optical quality of the film, and therefore the spatial resolution of the detector, is affected by the lattice mismatch between film and substrate. The considerations made in this chapters about the sub-

strate influence on the MTF are valid only if the optical quality of the films grown on different substrates is comparable.

Absorption efficiency

Up to this point we only focused on the energy spread in the materials and the consequential limitations on the spatial resolution. An additional limitation of thin film scintillators is their low absorption, especially at high energy, which affects the whole detector efficiency.

By considering the different atomic cross sections, for example by using the NIST database, the percentage of incoming photons that interact with a scintillator of a certain thickness can be calculated. The result of this calculation is shown in figure 2.6(a), for different materials of 5 μm thickness. However, the interaction of an X-ray photon with the scintillator does not always lead to the deposition of energy and light emission. The photon can be deflected by Compton and Rayleigh scattering or generate secondary particles, which may be able to escape from the scintillator. Since the scintillator is a few micrometers thick, the probability that the energy of the primary photon is not completely deposited is non negligible. Therefore, the attenuation in the material may not be a good approximation for the absorption efficiency, especially at high X-ray energy.

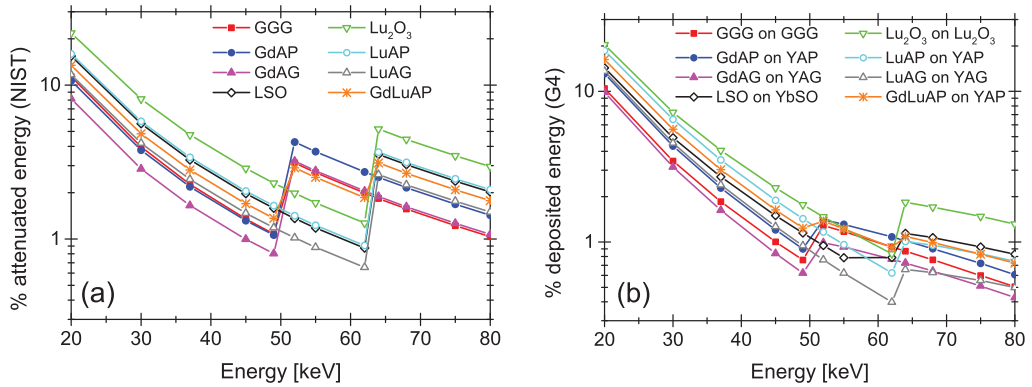

Figure 2.6: (a) Percentage of the incident energy attenuated by 5 μm thick scintillators, calculated using the NIST database (68). (b) Percentage of the incident energy deposited in 5 μm thick scintillators on 150 μm thick substrates, calculated tracking all the secondary X-rays and electrons using Geant4.

We therefore used Monte Carlo calculations to evaluate the real amount of energy deposited in the scintillator: the results are reported in figure 2.6(b). The attenuation is a good approximation of the absorption in the material at low energy, but it becomes less precise as the energy increases. In particular, above the K-edge, the gain in absorption can be significantly lower than what is expected from the attenuation due to the creation of a large amount of high energy fluorescence photons which can escape the scintillator easily. For example, while the Lu_2O_3 attenuation increases of approximately a factor 4 from 61 keV to 64 keV, the simulated deposited energy only increases of a factor 2.5.

The substrate can also play a role. In figure 2.7, the percentage of attenuated energy calculated by NIST (black line), the energy deposited simulated by Geant4 (black dotted line) and the ratio E_{dep}/attenuation (blue line) are reported for a 11.4 μm thick GdLuAP scintillator on a YAP substrate.

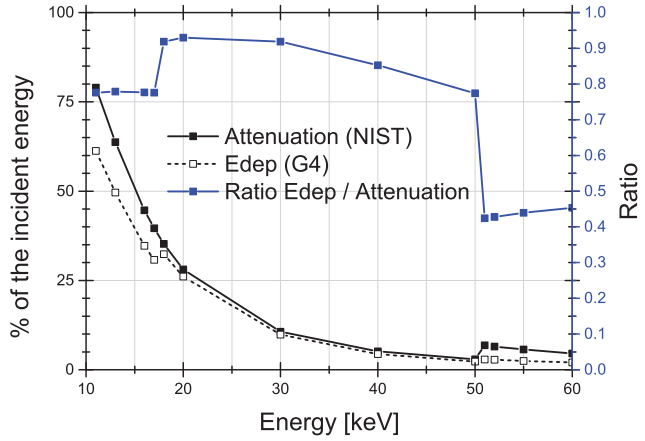

Figure 2.7: Attenuation of the scintillator calculated using NIST database and compared with the energy deposited in the scintillator which was calculated using Monte Carlo calculations, for a 11.4 μm thick GdLuAP film on a YAP substrate.

The ratio E_{dep}/attenuation is always lower than 1 and decreases slowly for increasing energy. In fact, while increasing the X-ray photons energy, secondary particles with higher energy and therefore, higher probability to escape the film, are produced.

When the energy is above the K-edge of yttrium the ratio sharply increases because part of the fluorescence photons produced in the substrate are re-absorbed in the film, which as discussed above, degrades the resolution. When the energy is high enough to cause the fluorescence in the scintillator, the ratio reduces due to the florescence photons that can easily escape the thin film scintillator. The lower ratio is obtained above the scintillator K-edge, and then starts to increase slowly.

Figure of merit

To achieve the sub-micrometer spatial resolution demanded in some X-ray imaging experiments, thin film scintillators are selected. However, the low absorption of the selected thin films reduces the detector's efficiency. For example, 50 μm of LSO attenuates at least 8 % of the incoming radiation up to 80 keV, while for 5 μm of LSO the attenuation already reduces to 8 % at 25 keV. To evaluate the best compromise between a sharp image and an efficient detector, we defined a figure of merit (FoM):

$$\mathrm{FoM(E)} = \mathrm{MTF}^{\mathrm{G4}}_{\mathrm{500\ lp/mm}}\mathrm{(E)} * \mathrm{E_{dep}(E)} \tag{2.1}$$

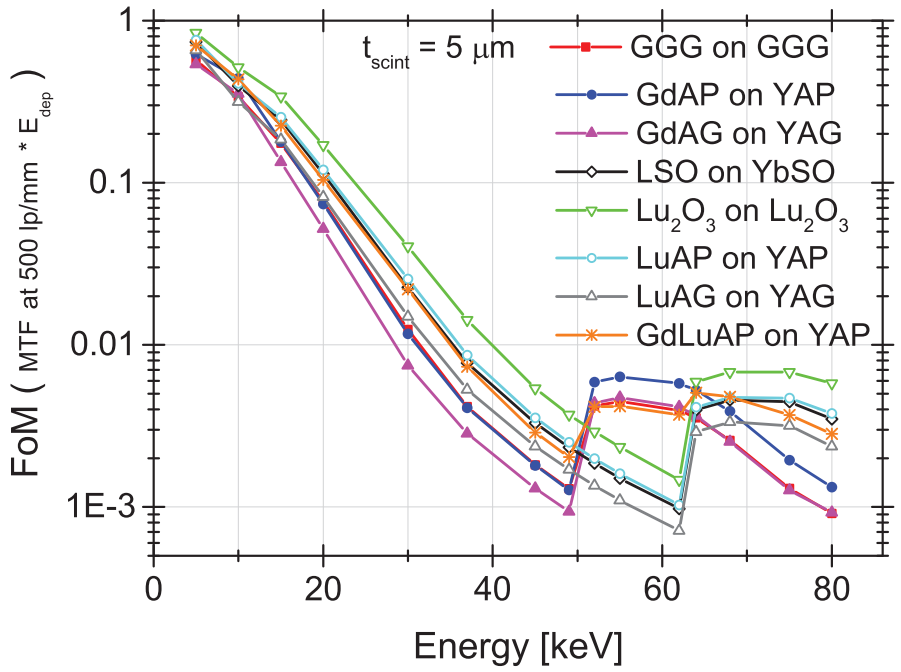

Figure 2.8: Figure of merit defined as value of the MTF at 500 lp/mm by the energy deposited in the scintillator, calculated for different 5 μm scintillators on a substrate.

The results are plotted in figure 2.8. This figure allows us to evaluate the best material to use in every energy range, while considering the spatial resolution, contrast and efficiency. The assumption that LuAG and LuAP are comparable above 63 keV, arising from figure 2.5 is wrong as we now know that LuAP is a better compromise

due to the higher absorption. LSO and Lu_2O_3 have a slightly lower MTF due to the substrate fluorescence background, but their FoM is better than the other materials considered. We can therefore conclude that below 50 keV and above 64 keV, Lu_2O_3 is the most performant material, while between 50 keV and 64 keV GdAP is the best. A mixed composition as GdLuAP can compete both with the existing GGG and LSO in the 50-75 keV range.

It is important to keep in mind that here only the absorption in the matrix of the scintillator is considered. To get more precise results, other parameters should also be included.

Firstly, the light yield (LY), that may change the overall scintillators efficiency. However, this parameter is difficult to evaluate for the materials that have not been developed and carefully optimized yet. Therefore, the different scintillators are assumed to have the same LY. Additionally, the LY may depend on the X-ray energy, due to non-proportionality phenomenon (26), presented in section 3.3.2. Secondly, the effect of the microscope optics and emission wavelength of the scintillator, which depends on the choice of the dopant. The resolution is ultimately limited by the light diffraction: the smallest spot that the optics can focus depends both on the wavelength λ and on the numerical aperture NA. Moreover, both the wavelength λ and NA define the depth of field of the optics, meaning the maximum thickness of the scintillator which can be projected as a focused image. This part of the calculation will be described in detail in chapter 3.

A more precise evaluation of the figure of merit as a function of the energy E should therefore be:

$$\mathrm{FoM(E)} = \mathrm{MTF}^{\mathrm{G4+Optics}}_{500\ \mathrm{lp/mm}}(\mathrm{E}) * \mathrm{E_{dep}}(\mathrm{E}) * \mathrm{LY}(\mathrm{E}) \tag{2.2}$$

2.4.2 What happens at the K-edge?

In this section the improvement of the MTF curve above the scintillator K-edge energy is investigated. To avoid confusion with effects that may come from the substrate, the results are reported for free-standing scintillators.

Energy distribution along the film thickness

The energy distribution and the MTF were studied as a function of the coordinate z along the thickness of the scintillator.

Figure 2.9(a)-top shows the percentage of the incoming energy deposited in the scintillator (E_{dep}) as a function of z, for 5 and 50 μm thick GdAP free-standing films, below and above the Gd K-edge. In the case of 5 μm thick GdAP, the curve increases going from the surfaces (z = 0 and z = 5 μm) to a maximum located approximately half way into the scintillator. The shape is similar at 49 keV and 55 keV, although the values are higher above the K-edge. This trend is far away from what we could expect from the Beer-Lambert law, which describes the energy attenuation along the thickness t of a material as an exponential decay depending on a certain attenuation coefficient μ, which depends on the energy E:

$$I = I_0 \, e^{-\mu(E) \, t} \tag{2.3}$$

For a 50 μm thick scintillator, once again $E_{dep}(z)$ decreases close to the two surfaces, but in the central part it can be described as an exponential decay.

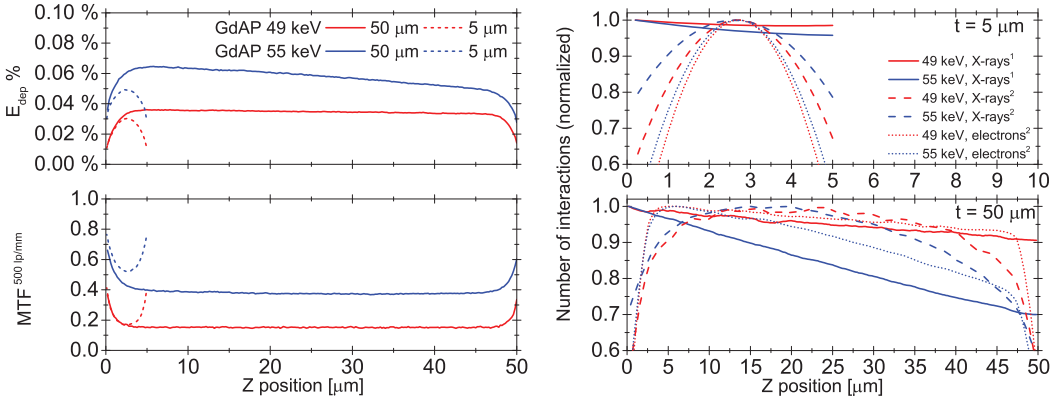

(a) (b)

Figure 2.9: (a)-top Energy deposited, (a)-bottom MTF and (b) number of interactions for secondary electrons (electrons^2), primary and secondary X-ray photons (X-rays^1, X-rays^2) as a function of the depth z in the scintillator, at 49 and 55 keV, for 5 μm and 50 μm free-standing GdAP scintillators.

To understand the curve $E_{dep}(z)$ obtained from the Monte Carlo calculation one has to

remind that the Lambert-Beer law only keeps the cross section for primary interactions of the incident X-ray photons into account. In the case of incident X or gamma rays, the attenuation can not always be considered as a good approximation of the the dose deposited in the material, as we discussed above, due to the secondary particles cascade. If we imagine to divide the scintillator along z in slices of thickness dz, to calculate the energy deposited in the j^{th} slice in the scintillator (E^{j}_{dep}) we have to sum the energy deposited by the primary X-ray photon interactions in the j^{th} slice ($E^{j}_{dep^1}$), the energy deposited by the secondary particles produced in the j^{th} slice ($E^{j}_{dep^2}$) and the energy deposited by the secondary particles produced in the other slices that can reach the j^{th} slice ($E^{\neq j}_{dep^2}$):

$$E^{j}_{dep} = E^{j}_{dep^1} + E^{j}_{dep^2} + E^{\neq j}_{dep^2} \tag{2.4}$$

In reality, the X-rays do not deposit the energy directly, but generate secondary electrons, that eventually deposit energy. In the Monte Carlo model, an energy threshold is defined for the production of the secondary particles, meaning that secondary particles with an energy lower than the threshold are not generated. The remaining energy is hence counted as deposited by the X-ray in the position of the interaction. The energy threshold is user defined and was set at 250 eV. This approximation is sufficiently accurate since the attenuation length for electrons at 250 eV in GdAP is below the spatial resolution range which is studied. It is important to keep in mind that the energy deposited by X-rays depends on the production threshold. In our case, it corresponds to the amount of energy deposited by electrons with a diffusion length shorter than the size of the voxel defined in the simulation.

For a certain value of the production threshold, an incident X-ray photon interacting with GdAP deposits a fraction C_1 of its energy and transfers the remaining $(1 - C_1)$ to secondary particles. A fraction C_2 of the secondary particles is re-absorbed in the thickness dz of the slice. The first and the second components of the equation 2.4 can be simply re-written as a function of the primary X-ray photons able to reach the j^{th} slice (located at $z = d$):

$$E^{j}_{dep^1} \propto C_1 \, e^{-\frac{1}{\ell^{X}_{1}} d} \tag{2.5}$$

$$E^{j}_{dep^2} \propto (1 - C_1)\,(C_2)\,e^{-\frac{1}{\ell^X_1}\,d} \tag{2.6}$$

ℓ^X_1 is the attenuation length of the incident X-ray photons in the material and it is inversely proportional to the attenuation coefficient μ. The last component in equation 2.4 is the sum of the secondary particles produced in every i^{th} slice (where $i \neq j$) and not re-absorbed in the same slice, attenuated as a function of the distance $\mid d_i - d \mid$ between the i^{th} and j^{th} slice. Defining ℓ^X_2 and ℓ^{el}_2 as the attenuation lengths of the secondary X-ray photons and electrons respectively, we can write:

$$E^{\neq j}_{dep^2} \propto= \sum_{i=1}^{N,i\neq j} e^{-\mu\, d_i}(C^{el}_3\, e^{-\frac{1}{\ell^{el}_2}\,|d_i-d|} + C^X_3\, e^{-\frac{1}{\ell^X_2}\,|d_i-d|}) \tag{2.7}$$

For the primary X-ray photons in GdAP $\mu = 21.3\ cm^{-1}$ at 49 keV and $\mu = 75.4\ cm^{-1}$ at 55 keV, corresponding to an attenuation length of 469 μm and 133 μm respectively. For electrons in GdAP the attenuation length calculated from the the CSDA (Continuous Slowing Down Approximation range) in the energy range 1-55 keV is 1-10 μm (69). The secondary X-ray photons will mostly have the energy of the L and K-shell of Gd, corresponding to an attenuation length of 5 and 100 μm respectively. Additionally, the fluorescence rate for the K-shell in Gd is approximately six times the fluorescence rate of the L-shell. The first two components of equation 2.4 are therefore almost a constant along the depth of the scintillator. This is also the case for the decay describing the high energy secondary X-ray photons. Defining ℓ_2 as the average attenuation length of the secondary electrons and secondary low energy X-ray photons we finally rewrite equation 2.4 as:

$$E^{j}_{dep} = K + C_4 \sum_{i=1}^{N,i\neq j} e^{-\frac{1}{\ell_2}\,|d_i-d|} = K + \int_0^t e^{-\frac{1}{\ell_2}\,|z-d|}\,dz \tag{2.8}$$

This function has a maximum at $z = t/2$ and decreases going toward 0 or t, in agreement with the results for the 5 μm thick scintillator in figure 2.9(a)-top. The shape of $E_{dep}(z)$ describes, therefore, the flux of secondary particles at different depth in the scintillator, that is lower at the surfaces. However, when the thickness is larger than ℓ, all the slices at the center, located at higher distance than ℓ_2 from the surfaces, will be reached by about the same flux of secondary particles. The particles generated above a certain

distance from the considered slice, in fact, do not contribute to the flux. In figure 2.9(a)-top $E_{dep}(z)$ is reported for a 50 μm thick scintillator. The variation of the secondary particles flux is observed close to the surfaces of the scintillator, while in the central region the curve is well described by the Beer-Lambert law.
The curves describing the number of interactions of the different particles as a function of z reported in figure 2.9(b) confirm what is described above.
Firstly, the number of interactions of the primary X-rays (X-rays[1]) is reduced of a value corresponding to the attenuation calculated using the NIST database reported in table 2.2. The number of interactions of the primary X-ray photons therefore simply follows the exponential decay $e^{-\mu(E)z}$ as defined in the equation 2.3.

Table 2.2: Attenuation in GdAP calculated using the NIST database.

material	E^{att} at 49 keV	E^{att} at 55 keV
GdAP 5 μm	1.1%	3.7%
GdAP 50 μm	10.1%	31.4%

Secondly, the number of interactions of the secondary electrons (electrons[2]) describes the same curve as seen in figure 2.9(a), which is showing that the electron flux follows the distribution described above. Additionally, it confirms that most of the energy is deposited by electrons.
Lastly, the curve describing the interactions of the secondary X-rays (X-rays[2]) is similar to the one of the electrons, but the slopes close to the surfaces are less steep, due to the longer attenuation length of the X-ray photons.
In addition to its contribution to the effective energy deposition, the diffusion of the secondary particles plays a crucial role for the MTF. Indeed it degrades the MTF due to the energy being deposited far from the position of the first interaction. In figure 2.9(a)-bottom the MTF is reported as a function of z. It can be seen that the contrast is higher close to the surfaces, and decreases going to the center of the scintillator where the secondary particles flux is higher.
For the 5 μm thick GdAP, the complete PSFs and MTFs calculated at different z are reported in figure 2.10. All the MTF curves at 49 keV show lower contrast than the MTFs calculated at 55 keV, and all PSFs are less sharp. For the 50 μm thick scintillator, the value of the MTF at 500 lp/mm is approximately constant in the central part of the scintillator ($z \approx 3$ μm to $z \approx 47$ μm) both at 49 and 55 keV (figure 2.9(a)-bottom). We can therefore conclude that the MTF improvement at the K-edge is not just caused

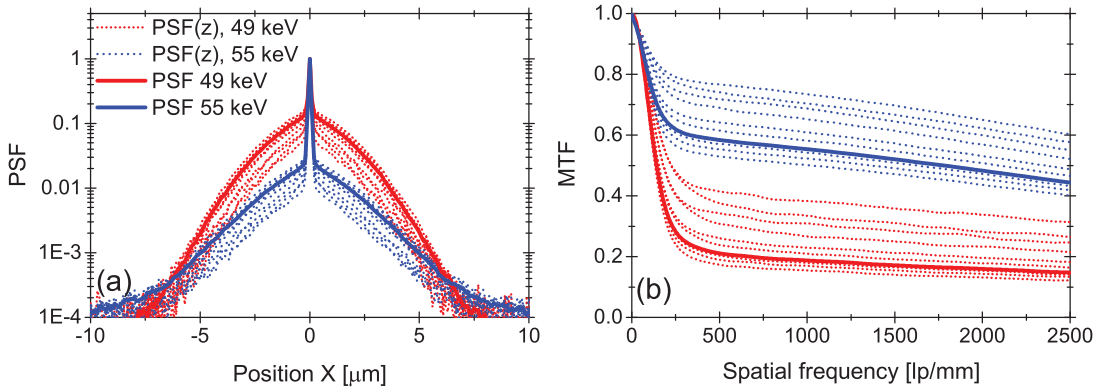

Figure 2.10: PSF and MTF curves at different z in the depth of the scintillator, for a free-standing 5 μm thick GdAP scintillator at 49 and 55 keV.

by a different energy distribution and PSF broadening along the depth of the scintillator.

Contribution of the different interactions

The contribution of the different particles to the energy deposition was studied below and above the K-edge. Although the MTF is calculated from the energy deposited, for simplicity only the number of events for every kind of interaction was considered. In fact, to really compute the energy deposited by every different interactions, the energy deposited by all the secondary particles produced should be kept into account. However, even doing so, the result is not trivial to interpret as a consequence of the fact that different kind of interactions take place in the same cascade.

The spatial distribution of the number of events for the X-ray and electronic interactions is reported in figure 2.11(a-e) for 5 μm thick free-standing GdAP film at 49 and 55 keV. For X-rays, the distributions of the photoelectric effect, Rayleigh and Compton scattering are considered separately. The PSFs evaluated from the total energy deposited in the film are reported in figure 2.11(f) as a reference.

The distribution of the X-ray interactions, including both primary and secondary X-rays, (X-rays^{1+2}, fig. 2.11(a)) is almost completely defined by the photoelectric effect (X-rays^{1+2}, fig. 2.11(b)). This result is not unexpected since X-ray photons in the energy range 1-100 keV interacting with such a high-Z material do so mainly through

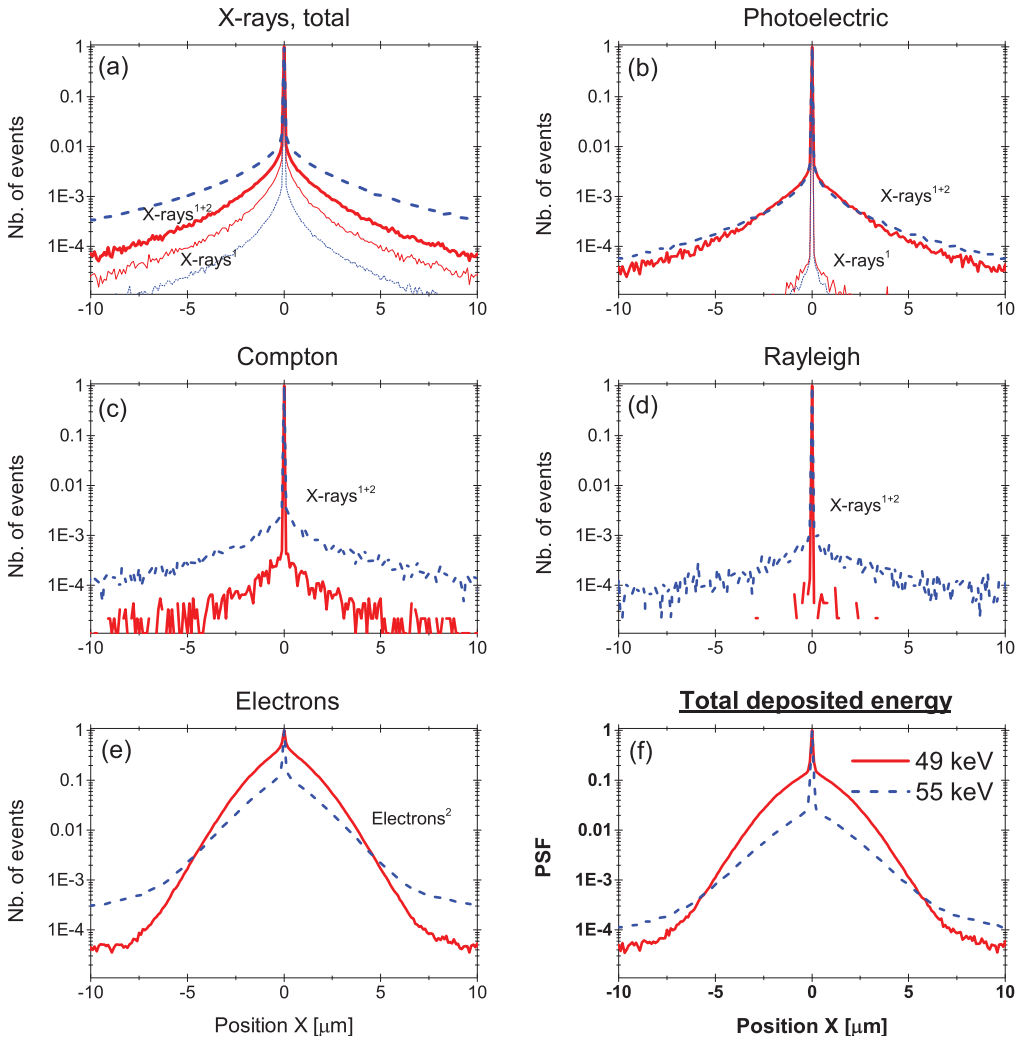

Figure 2.11: Normalized distributions of the number of events for the different kinds of interactions: (a) all the X-ray interactions, (b) photoelectric effect, (c) Compton scattering, (d) Rayleigh scattering, (e) all the electronic interactions. (f) PSF calculated from the total deposited energy. In (a) and (b) the curves counting the primary or secondary X-rays (X-rays^1, X-rays^2) are also reported. Scintillator: GdAP 5 μm free-standing. Energy: 49 and 55 keV.

photoelectric interaction (more than 80 % of the interactions) than Rayleigh or Compton scattering.

The scattering events define to the tails of the distribution (figure 2.11(c,d)). Their contribution is more important at 55 keV than at 49 keV, in contradiction to both the MTF improvement and the increase of the photoelectric effect cross-sections above the

K-edge. For example for GdAP, the photoelectric effect probability increases from 84 % at 49 keV to 97 % at 55 keV. This contradiction can be explained by considering the primary X-ray interactions separately (X-rays[1], fig. 2.11(a)). The spatial distribution resembles a Dirac function with tails due to the X-ray scattering. These tails are lower at 55 keV, in agreement with the lower scattering probability. When the X-rays[2] interactions are included, the tails are higher at 55 keV, due to the higher number of secondary X-rays produced by K-shell fluorescence.

The improvement of the MTF above the K-edge can therefore be partially attributed to a different distribution of the interactions of the incident X-rays due to the increase of the number of photoelectric interactions, which reduce the probability of the primary X-rays to diffuse in the tails. More electrons are generated in the central peak of the distribution, at X=0.

However, to completely explain the improvement of the MTF at 55 keV, the electrons diffusion has to be taken into account. The distribution of the electron interactions is reported in figure 2.11(e). Although the electrons are produced where the X-rays interact with the atoms, the X-ray interaction distribution differs from the one of the electron. The last resembles the PSF (fig.2.11(f)) and is narrower at 55 keV, in agreement with the MTF improvement. This can be explained by considering the electron attenuation length below and above the K-edge. Most of the energy is transferred to electrons through a photoelectric interaction. The X-ray photon is completely absorbed and a core electron is ejected, leaving the atom in an excited state, which relaxes through Auger of fluorescence emission. The photoelectron is ejected with an energy E_{el}^{kin}:

$$E_{el}^{kin} = E_X - E_{binding} \ , \tag{2.9}$$

where E_X is the the energy of the incoming X-ray and $E_{binding}$ is the binding energy of the electron. For a given $E_{binding}$, the photoelectron energy and, therefore, the attenuation length increases with E_X. However, above the K-edge, the electrons can, in addition to the M and L shells, also be emitted from the Gd K-shell with a lower energy because of the stronger binding energy with the atom.

The energy spectra of the secondary electrons at the creation are reported in figure 2.12(b), for X-ray energies equal to 35, 49 and 55 keV. The peaks due to the L and M-shell electrons are located in the energy range 25-55 keV. Their positions move to higher energy for increasing X-ray energy and can be calculated from equation 2.9. For

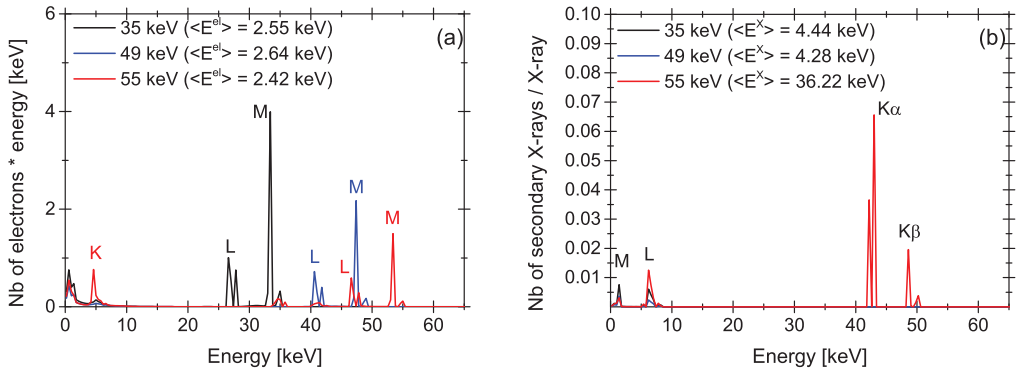

Figure 2.12: Energy spectra of the (a) secondary electrons and (b) secondary X-rays generated per incident X-ray in 25 μm of free-standing GdAP. The average energy of the secondary electrons and X-rays is reported in the legend.

Gadolinium, the binding energies for the M and L shells are approximately 1.5 and 7.5 keV respectively. At 55 keV, the peak due to the K-shell appears at $\approx$ 5 keV (binding energy 50.2 keV). The average electron energy, reported in the legend, decreases above the K-edge. The additional smaller peaks visible in the spectra are due to Auger electrons or photoelectrons produced by secondary particles, as well as interactions with aluminum atoms.

In the considered energy range the attenuation length in GdAP for the K-shell photoelectrons is a few hundred nanometers, while for the M and L-shells photoelectrons is 3-11 μm. The fraction of energy transferred to K-shell photoelectrons reduces the average electron diffusion length and hence the energy spread, which explains the sharper PSF above the K-edge.

On the contrary, the energy of the secondary X-rays increases, due to the K-shell fluorescence. The energy spectra of secondary X-rays is reported in figure 2.12(b). However, the K-shell fluorescence X-ray photons are in the energy range 43-50 keV, which corresponds to an attenuation length above 100 μm in GdAP. Consequently, the spatial resolution is not strongly degraded by these photons, since they mostly escape without interacting and thus without depositing energy in the film. Their influence is visible in the tails of the PSF, which are more intense at 55 keV (figure 2.11(f)).

2.4.3 Substrate effect

The choice of the substrate is critical from the point of view of the performance of the thin film scintillator. Firstly, the crystalline structure of the substrate has to be the same as that of the film and the lattice mismatch has to be sufficiently small to be able to grow a scintillator with good optical quality, a mandatory criterion to ensure a good image quality. Secondly, a substrate which is non-scintillating at the same emission wavelength as the scintillator is required. In the simulations these first two constraints are not considered, and all the scintillators are supposed to have the same optical quality and no visible luminescence from the substrate. However, the substrate fluorescence can also affect the image quality, since the fluorescence photons can interact with the film creating an offset in the PSF which reduces the MTF at low spatial frequencies.

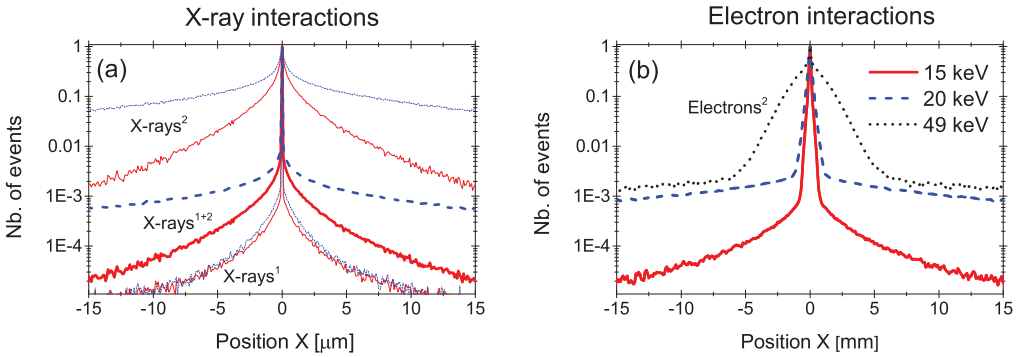

Figure 2.13: Spatial distribution of the (a) X-ray and (b) electron interactions, calculated for 5 μm of GdAP on a YAP substrate at 15 and 20 keV.

This effect has been introduced in section 2.4.1. In figure 2.4(b), the MTF at 20 keV calculated for a GdAP film on a YAP substrate shows a 20 % reduction of the contrast at low spatial frequencies, which is not observed for the free-standing GdAP. In figure 2.13 the spatial distribution of the X-ray and electron interactions in the GdAP film at 15 and 20 keV is reported. From 15 to 20 keV, almost no difference is observed for the primary X-ray interactions (X-rays^1), while the secondary X-ray interaction distribution (X-rays^2) presents tails which are significantly higher at 20 keV than at 15 keV. The same tails are visible in the electron interaction distributions, due to the production of electrons by secondary X-ray interactions far from the central part of the distribution (x = 0). On the contrary, the central part of the distribution remains

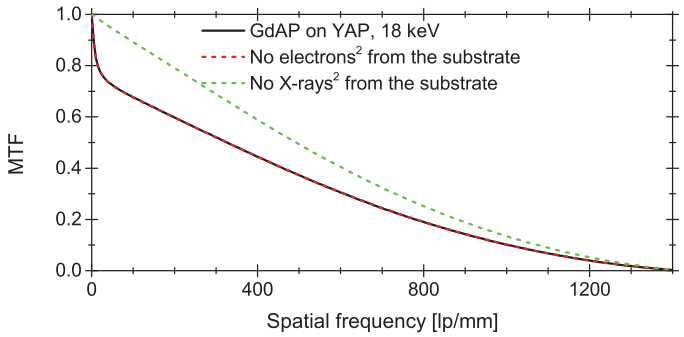

Figure 2.14: MTF calculated for 5 μm of GdAP on YAP at 18 keV, tracking all the particles (black) or killing the secondary electrons (dashed red) or X-rays photons (dashed green) produced in the substrate.

unchanged, mainly due to electron diffusion, as no significant variation is expected in the electron attenuation length. As reference, the electron interaction distribution is reported at 49 keV. The central part of the distribution is broader, due to the higher energy photoelectrons produced in the film, while the tails are only slightly higher.
The reduction of the MTF values at low frequencies is due to the tails in the interaction distribution and in the PSF. They originate from the secondary X-rays produced in the substrate which interacts with the film, creating a cascade which deposits energy far from the position of the first interaction. Their number increases significantly above the substrate K-edge causing the loss of contrast in the MTF.
To confirm this hypothesis, the MTF was calculated removing the secondary electrons or X-ray photons generated in the substrate (figure 2.14). When the substrate's secondary electrons are removed, the obtained MTF is the same as the one obtained after tracking all the secondary particles. Moreover, when the substrate's secondary X-ray photons are removed, the low frequency contrast reduction disappears.

2.4.4 Thickness dependency

For a high resolution experiment, a thin film scintillator is required. The resolution degrades when the film thickness increases due to the distribution of the energy deposited in the scintillator and due to the out-of-focus light that is collected by the optics. The effect of the out-of-focus light is not included in this chapter's results. Therefore, the effect of the thickness on the MTF described in this chapter is only due to the energy distribution in the scintillator.

The MTF calculated from the energy distribution in different thicknesses of free-standing GdAP and GdAP on a YAP substrate is reported in figure 2.15 for different X-ray energies.

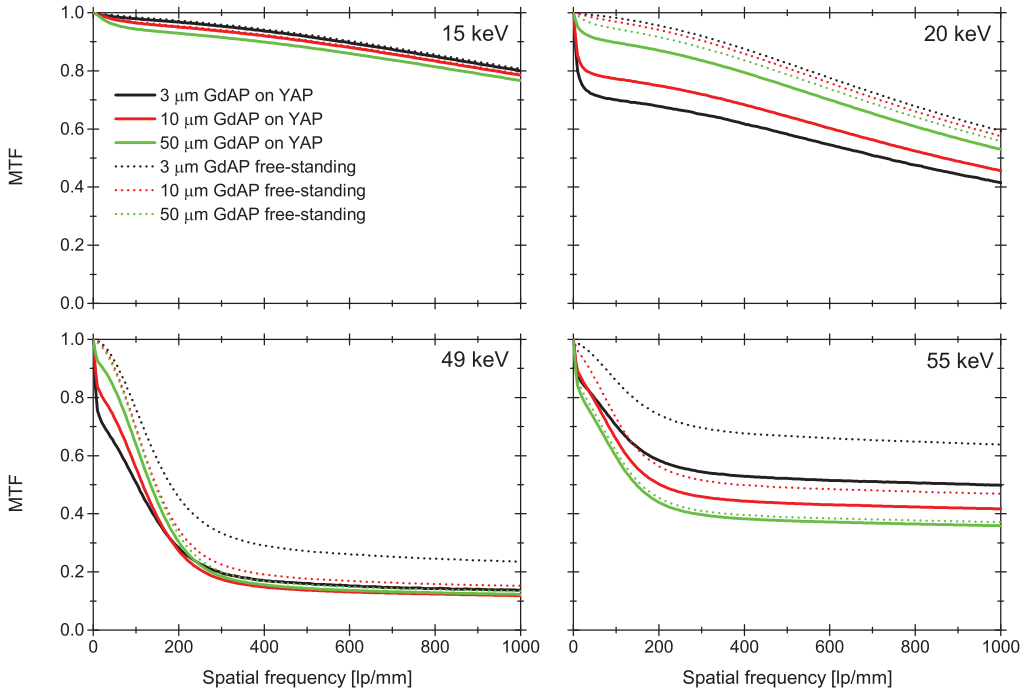

Figure 2.15: MTF calculated from MC simulations for different thicknesses of free-standing GdAP or GdAP on a YAP substrate, at different energies.

Increasing the thickness has only a negligible effect on the MTF if we consider free-standing scintillators. For the free-standing scintillator, at low energy (15-20 keV) no significant differences can be observed for thicknesses in the range 3-50 μm. At 49 keV, the MTF is degraded if the thickness is increased from 3 to 10 μm, but remains almost unchanged from 10 to 50 μm. These results can be explained using the discussion in section 2.4.2 about the MTF variation as a function of the depth z along the thickness in the scintillator: the MTF is degraded by the flux of secondary electrons. However, only the electrons produced at a distance smaller than the attenuation length contribute to the flux. For X-ray photons at 15-20 keV, the electrons ejected from the gadolinium M and L shells have an energy in the range 8-18 keV, corresponding to an attenuation length shorter than 2 μm. Therefore, the MTF is not degraded when the thickness is larger than 2 μm. On the other hand, at 49 keV, the L and M electrons will be ejected

with an energy of 42-47 keV, corresponding to a 7-9 μm attenuation length. Therefore, when the thickness is increased from 3 to 10 μm the MTF is degraded, while from 10 to 50 remains constant.
At 55 keV, above the Gd K-edge, even tough the MTF is degraded by the X-ray fluorescence photons, the attenuation length of the electrons decreases because of the lower energy electrons emitted from the Gd K-shell. For larger thicknesses, the probability that these fluorescence photons interact with the film degrade the resolution becomes higher. A contrast reduction at low frequencies is in fact observed for the 50 μm GdAP film.
Considering GdAP scintillators on a YAP substrate (figure 2.15 continuous lines) the behavior is similar to the free-standing GdAP. However, a thicker scintillator can improve the MTF by reducing the amount of fluorescence from the substrate. In fact, at 20 keV, a better MTF is predicted for the 50 μm scintillator as compared to the thinner ones. For increasing energy, this effect starts to compete with the longer attenuation length of the secondary electrons. At 49 keV, for example, better contrast is observed for the thickest investigated scintillator at low frequencies, due to the substrate fluorescence, while at high frequencies the contrast is approximately the same for the different considered thicknesses.

2.5 Conclusions

A Monte Carlo application based on the Geant4 toolkit has been developed to study the distribution of the energy deposited in free-standing or substrate-based few micrometer thick SCFs. The obtained distribution was used to evaluate the absorption efficiency and MTF response of the films.
Different scintillating film compositions have been studied as a function of the X-ray energy, in the range 5-80 keV. The MTF decreases with the X-ray energy, but a significant improvement is predicted above the K-edges. The improvement is attributed to the increase of the probability of the photoelectric effect and to the reduction of the ejection energy and attenuation length of the photoelectrons.
The substrate also plays a crucial role. The X-rays not absorbed in the film interact with the substrate and, depending on the energy, generate X-ray fluorescence. These secondary photons can deposit energy in the film and create an offset in the energy

distribution, corresponding to a drop in the contrast at low spatial frequencies.
The total amount of energy deposited in the scintillator was also evaluated. For a thin film, the attenuation calculated from the cross section of the interactions of the primary X-ray was found to be a good approximation of the absorption efficiency only at low energies. It becomes less precise at high energy and in particular above the K-edge, where the absorption efficiency is overestimated due to the escape of secondary particles from the thin film.
A figure of merit based on the MTF response and absorption efficiency have been evaluated to select the most promising materials. Lutetium oxide is, due to the high absorption efficiency, the most promising among the simulated materials at X-ray energies in the range 5-51 keV and 64-80 keV. Compared to the state-of-the-art LSO SCF, the MTF response of Lu_2O_3 is higher in the 5-50 keV range and approximately the same in the 64-80 keV range. In the 51-64 keV range, the highest figure of merit was predicted for gadolinium perovskite. These results do not keep into account the optical quality and the light yield of the SCFs, which can not be precisely evaluated before the development of the materials.
Lastly, the effect of the scintillator thickness was also evaluated. For free-standing scintillators, increasing the thickness was found to be detrimental for the MTF only up to a thickness which corresponds to the attenuation length of the secondary electrons. Above this value, the MTF remains constant. On a substrate a thicker scintillator could be beneficial for the MTF response since less photons are able to reach the substrate and produce X-ray photons which degrade the MTF. However, the MTF variation with the film thickness presented in this chapter does not keep into account the microscope optics used in high-spatial resolution detectors. This aspect is introduced in the next chapter.

Chapter 3

The indirect detector model

3.1 Blurring of the microscope optics

The energy distribution calculated using Monte Carlo corresponds to the light source that is produced by the scintillator, which is not necessarily equal to the light distribution measured by the high-resolution detector. In fact the light source, while projected on the camera by the microscope optics, is also blurred. Further calculations are therefore needed to estimate the spatial resolution and the MTF of the detector system in a realistic way, comparable with the experimental data.

The best achievable spatial resolution is related to the numerical aperture (NA) of the microscope objective and to the scintillator's emission wavelength (λ). Even in the case of an ideal aberration-free optical system, a perfect point source is always focused as an interference pattern, due to light diffraction. The central maximum of this interference pattern is called the Airy disk. If we define the spatial resolution limit according to the Rayleigh criterion, it can be estimated as the distance $R_{Rayleigh}$ between two point sources such that the maximum of the Airy disk of the first one occurs at the minimum of the second one. $R_{Rayleigh}$ and the corresponding spatial frequency $f_{Rayleigh}$ can be estimated as (70):

$$R_{Rayleigh} \approx \frac{0.61\ \lambda}{NA}\ ; \qquad f_{Rayleigh} \approx \frac{0.82\ NA}{\lambda}\ . \tag{3.1}$$

The cutoff frequency f_C, which is the spatial frequency where the MTF contrast value

reduces to zero, can be calculated as (70):

$$f_C \approx \frac{2\,NA}{\lambda}\,. \tag{3.2}$$

The depth of field (DoF) is defined in optics as the distance between the nearest and farthest object that appears in focus. For a microscope objective, the DoF also depends on NA and λ (71):

$$DoF = \frac{\lambda\, n}{NA^2} + \frac{n}{NA\, M}\, e\,, \tag{3.3}$$

where n is the index of refraction (n = 1 for a dry objective, n ≈ 1.5 for an immersion objective), e is the camera pixel size and M is the total magnification of the optical system, which considers both the microscope optics and the eyepiece.
In figure 3.1 the DoF (dashed lines) and the $f_{Rayleigh}$ (continuous lines) are calculated as a function of NA, for different λ. Shorter wavelengths, as well as higher numerical apertures, increase the resolution limit. However, they also reduce the depth of field, making it harder to optimize the detector to be a diffraction limited system. A thinner scintillator, as well as a sub-micrometer precision focusing system is required to achieve that.

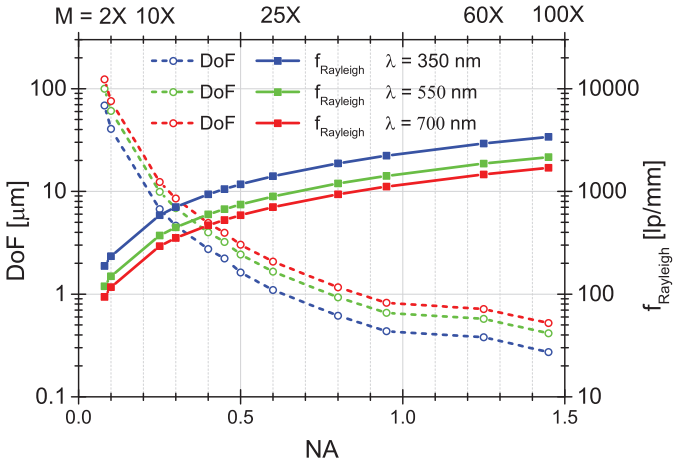

Figure 3.1: Depth of field and Rayleigh frequency as a function of the numerical aperture and of the wavelength. The magnification M associated with the NA is reported in the top X-axis.

If a 1 μm spatial resolution is required (i.e. 500 lp/mm spatial frequency) the numerical aperture of the optics has to be higher than 0.3 for visible light. However, such a microscope objective has a DoF of 5-10 μm. If the scintillator is thicker than the DoF, only the light produced within a certain depth dz in the scintillator is projected as a

focused image on the camera, while the light produced outside this region is projected as a defocused image. Since the focused and defocused images contribute to the total signal on the camera, the overall image quality is degraded.
An analytical model to calculate the response of an aberration-free optical system was described by Hopkins (57). Taking into account the light diffraction and the defect of focus δz, the optical transfer function (OTF) of a defocused optical system is calculated as a convergent series of Bessel functions:

$$
\begin{aligned}
&OTF(f,\delta z) = \\
&\quad \frac{4}{\pi a} cos\left(\frac{a|f^{\sim}|}{2}\right)\{\beta J_1(a) + \frac{sin(2\beta)}{2}[J_1(a) - J_3(a)] - \frac{sin(4\beta)}{4}[J_3(a) - J_5(a)] + ...\} \\
&\quad - \frac{4}{\pi a} sin\left(\frac{a|f^{\sim}|}{2}\right)\{sin\beta[J_0(a) - J_2(a)] - \frac{sin(3\beta)}{3}[J_2(a) - J_4(a)] + \\
&\quad + \frac{sin(5\beta)}{5}[J_4(a) - J_6(a)] - ...\}
\end{aligned}
$$

$$
a = \frac{2\pi n}{\lambda}|f^{\sim}|sin^2(\alpha)\,\delta z)\,, \qquad \beta = \arccos\left(\frac{|\mathrm{f}|}{2}\right), \qquad \mathrm{f}^{\sim} = \frac{\lambda}{\mathrm{nsin}\alpha}\,, \tag{3.4}
$$

where f is the spatial frequency in the object plane, n the refractive index of the scintillator and α the acceptance angle of the scintillator. For a symmetrical pupil function of the lens, the OTF is equal to its modulus, which is the MTF.
The image on the camera is the sum of superimposing signals originated at different positions along the thickness of the scintillator. Koch et al. (4), therefore, using equation 3.4, approximate the system response to the response of a defocused optical system, keeping the thickness of the scintillator into account:

$$
\mathrm{MTF(f)} = |\mathrm{OTF(f)}| = \left|\int_{-\mathrm{z_0}}^{\mathrm{z}-\mathrm{z_0}} \mathrm{OTF(f},\delta\mathrm{z})\mathrm{exp}^{-\mu(\delta\mathrm{z}+\mathrm{z_0})}\mathrm{d}\delta\mathrm{z}\right| \tag{3.5}
$$

where z_0 is the distance of the plane where the system is focused from the scintillator surface.
Following this approach the resolution can be evaluated as a function of the scintillator thickness and the optics' numerical aperture. The resolution, evaluated from the spatial frequency where the MTF contrast is 50 %, is reported in figure 3.2, as a function of NA. For every thickness, there is a minimum in the curve corresponding to the numerical aperture which gives the best resolution, i.e. the numerical aperture with a DoF equal to the thickness of the scintillator. Increasing NA above that value reduces the resolution due to the contribution of the defocused signal.

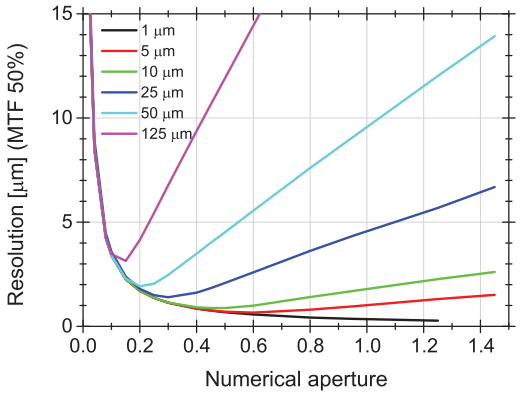

Figure 3.2: Spatial resolution limit as a function of NA calculated including light diffraction and defect of focus due to the scintillator thickness, for $\lambda = 550$ nm. A similar result was already published by Koch et al. in (4).

This approach do not keep the X-ray energy and the scintillator composition into account. It is only a valid approximation of the response of the detector if the energy spread in the scintillator is negligible compared to the optics blurring.

3.2 The detector's response

To keep both the scintillator and the microscope optics responses into account, each plane in the scintillator is considered as a light source. Their light distribution is described by the energy deposition calculated with the Monte Carlo simulations. The image of each plane is blurred by the optics as a function of the position of the plane along the thickness of the scintillator. Assuming the system is focused at a certain position z_0, the planes within a certain thickness dz (equal to the DoF) around z_0 are projected as a focused image and thus only blurred by the light diffraction. The planes outside dz, however, are additionally blurred as a function of the distance from z_0 (δz). For the calculation, the scintillator has been divided along z in bins of size S_z equal to 0.2 μm. S_z is selected to be approximately half of the minimum DoF of the systems that has been investigated in this study. For a dry objective in fact, the maximum NA is equal to 1 and the DoF between 0.4 and 0.5 μm for UV light (350 nm).
The total MTF, assuming that the system is focused on the j^{th} bin in z ($MTF^{tot}_{z_0=j}$), has been calculated as the average of every plane in the scintillator and weighed by the deposited energy:

$$MTF^{tot}_{z_0=j}(f) = \frac{\sum_{i=1}^{N} MTF^{scint}_{i}(f) \cdot MTF^{opt}_{i}(\delta z, f) \cdot E^{dep}_{i}}{\sum_{i=1}^{N} E^{dep}_{i}} , \tag{3.6}$$

where N is the total number of bins along z, $MTF^{scint}_{i}(f)$ is the MTF calculated from the energy deposition in the i^{th} slice and $MTF^{opt}_{i}(f)$ is the optics response calculated

using equation 3.4.
The position of z_0 was selected by calculating the maximum total MTF as a function of the focus position along z:

$$\mathrm{MTF}^{\mathrm{tot}} = \max(\mathrm{MTF}^{\mathrm{tot}}_{z_0=\mathrm{j}})\Big|_{\mathrm{j}=0}^{\mathrm{j}=\mathrm{t}} . \tag{3.7}$$

As a consequence of the out-of-focus light the effect of the thickness is more important than what has been shown in chapter 2, even at low X-ray energy. In figure 3.3, the scintillator response at 15 keV, reported as a reference ($\mathrm{MTF}^{\mathrm{scint}}$), has been combined with microscope optics with numerical aperture 0.4.

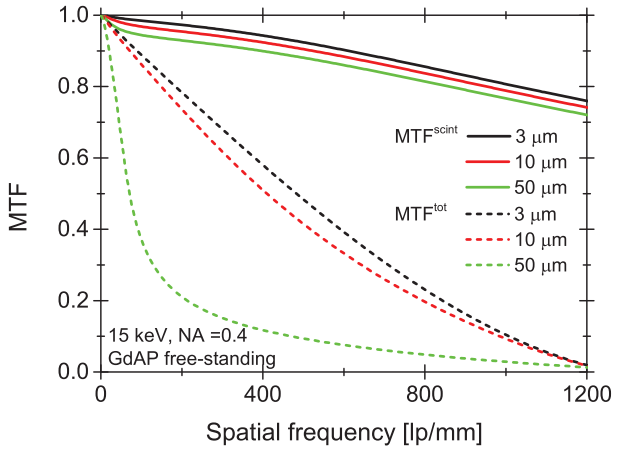

Figure 3.3: Scintillator MTF calculated using Monte Carlo ($\mathrm{MTF}^{\mathrm{scint}}$), and total MTF with NA = 0.4 ($\mathrm{MTF}^{\mathrm{tot}}$), calculated at 15 keV for different thicknesses of free-standing GdAP scintillators.

For $\lambda = 0.6$ μm, DoF ≈ 4 μm (equation 3.3) and $f_C \approx 1200$ lp/mm (equation 3.2). At 15 keV, due to the low average free path of the electrons, the scintillator response is approximately the same for a scintillator thickness between 3 and 50 μm, and the contrast is above 80 % up to 1000 lp/mm.
By adding the microscope optics we observe, firstly, that the system resolution is limited by the light diffraction through the optics, even for a scintillator thinner than the DoF: the value of the MTF calculated using the full model for the 3 μm thick scintillator is reduced to zero at the cutoff frequency.
Secondly, for a scintillator thicker than the DoF, the contrast, compared to a diffraction limited system, reduced due to the contribution of the defocused planes of the scintillator. The contrast at 500 lp/mm decreases from 50 % to 10 % while increasing the thickness of the scintillator from 3 to 50 μm.
In figure 3.4 the MTF including scintillator and optic responses ($\mathrm{MTF}^{\mathrm{tot}}$), as well as the separate contributions of $\mathrm{MTF}^{\mathrm{scint}}$ and $\mathrm{MTF}^{\mathrm{opt}}$, are reported for three different cases

with numerical aperture 0.8. As a reference, the MTF of a diffraction-limited system is also reported.

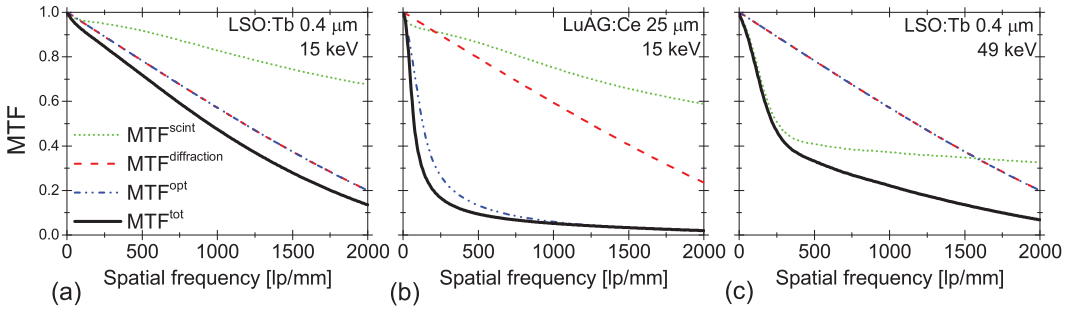

Figure 3.4: Contributions to MTF^{tot} (scintillator + optics) of the different phenomena: energy spread in the scintillator (MTF^{scint}), light diffraction ($MTF^{diffraction}$) and defocus (MTF^{opt}). NA = 0.8, scintillator and energy indicated in the plots.

The first case (fig. 3.4(a)) is almost a diffraction-limited system. Since the scintillator is thinner than the DoF (approximately 1 μm at 550 nm) no degradation due to the defocus is observed ($MTF^{opt} = MTF^{diffraction}$). At low X-ray energy (15 keV) the energy distribution in the scintillator is sharp. Therefore, the MTF^{tot} is mainly defined by the light diffraction. However, due to the energy spread in the scintillator, a degradation of 10 % in the contrast is observed as compared to the diffraction-limited system.
The second case (fig. 3.4(b)) is a strongly defocused system. The MTF is degraded by the defect of focus, due the fact that the scintillator is much thicker than the DoF.
The third case (fig. 3.4(c)) uses the same configuration as the first one. Hence, no defocus contribution is observed. However, the resolution is more degraded by the scintillator response, because at 49 keV the energy distribution in the scintillator is broad due to the diffusion of the high-energy secondary particles. The MTF is limited at low-spatial frequencies by the scintillator response and at high-spatial frequencies by the light diffraction.
In the three examples shown in figure 3.4, the MTF is mainly determined by one of the involved phenomena, i.e. the light diffraction, the defocus of the system and the scintillator response, respectively. However, considering only the most important phenomenon and approximating $MTF^{tot} \approx MTF^{opt}$ at low energy and $MTF^{tot} \approx MTF^{scint}$ at high energy leads to wrong estimation of the MTF.
Moreover, the system often has to be considered in an intermediate situation, where the different phenomena all contributes to the MTF, as for example in the presence of a small defect of focus at medium X-ray energies. In such cases, the evaluation of the

best configuration is not trivial when the whole model is not considered.

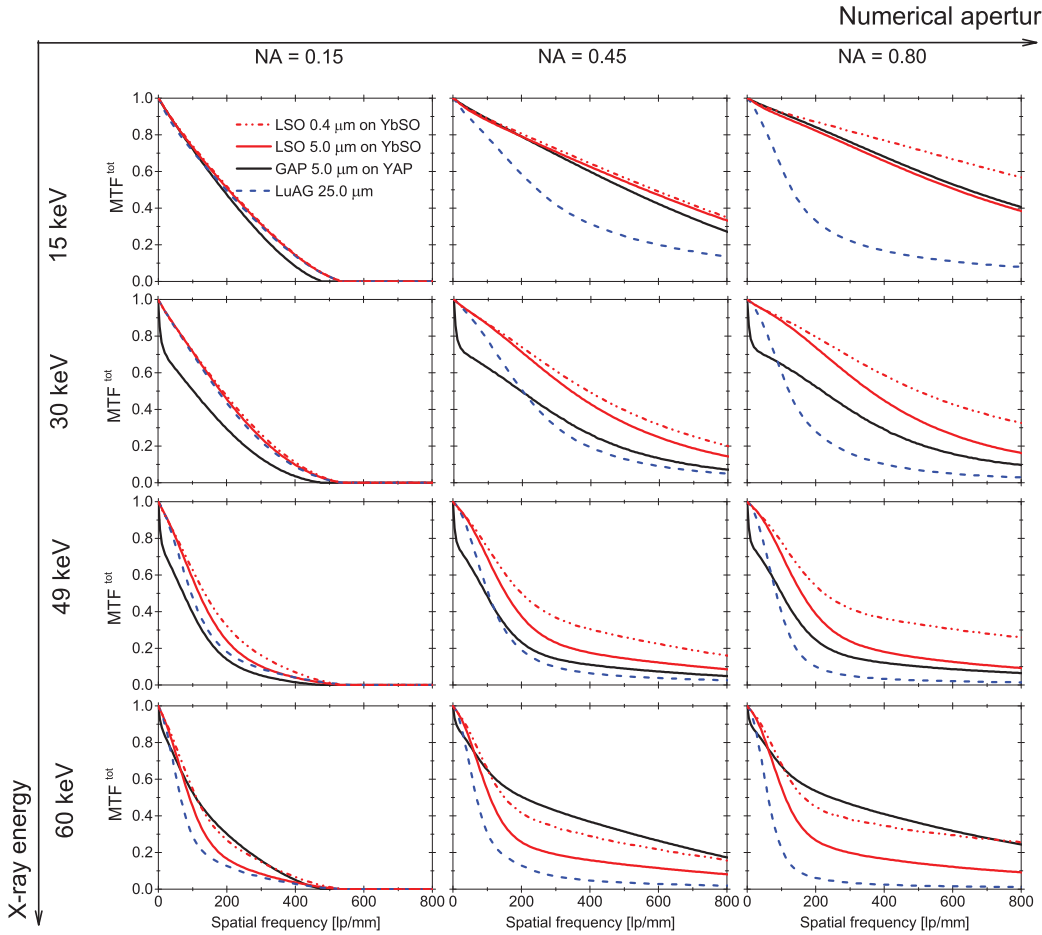

Figure 3.5: MTF^{tot} of 0.4 and 5 μm thick LSO:Tb films on YbSO substrate, a 5 μm thick GdAP:Eu film on YAP substrate and a 25 μm thick LuAG:Ce free-standing crystal, evaluated for different NA and X-ray energies.

In figure 3.5, configurations using different scintillators are evaluated: 0.4 and 5 μm thick LSO:Tb films on YbSO substrates, a 5 μm thick GdAP:Eu film on a YAP substrate and a 25 μm thick LuAG:Ce free-standing scintillator. The MTF^{tot} curves are compared for different X-ray energies and numerical apertures.
At low energy (15 keV) light diffraction and defocus play the crucial role. Hence, as expected, no difference is observed among the scintillators which are thinner than the DoF. At high NA the most performant scintillator is simply the thinner one. For the 25 μm thick LuAG:Ce scintillator the contrast using NA=0.8 is lower than using NA=0.15

for spatial frequencies below 400 lp/mm, due to the strong defocus.
The role of the material becomes crucial, when the energy is increased. At 30 keV the Y K-edge degrades the response of the GdAP scintillator. It is important to note, for NA=0.45, that the contrast calculated for the 25 μm thick LuAG:Ce and the 5 μm thick GdAP films are comparable.
At 49 keV all the MTFs are strongly degraded by the energy spread in the material. Since at high energy MTF^{scint} is degraded by the thickness of the scintillator (see for example figure 2.15), the thinnest scintillator is significantly more performant, even comparing thicknesses lower than the DoF. This is true especially at high NA, where both the defocus and the energy spread degrades the MTF of the thicker scintillators. As discussed in chapter 2, at high-energy the main role in MTF^{scint} is played by the K-edge of the scintillator. For example, at the 60 keV the MTF obtained for the 5 μm GdAP:Eu scintillator is higher than both the MTFs of the 5 and 0.4 μm thick LSO:Tb films.

To summarize, the plot in figure 3.2 was recalculated including the response of the scintillators. The curves are reported for the 5 μm thick LSO:Tb film on YbSO and GdAP:Eu film on YAP (fig. 3.6(a)) as well as for the 25 μm thick LuAG:Ce crystal (fig. 3.6(b)). The curves calculated only considering the optical model are reported as reference (black dashed lines).

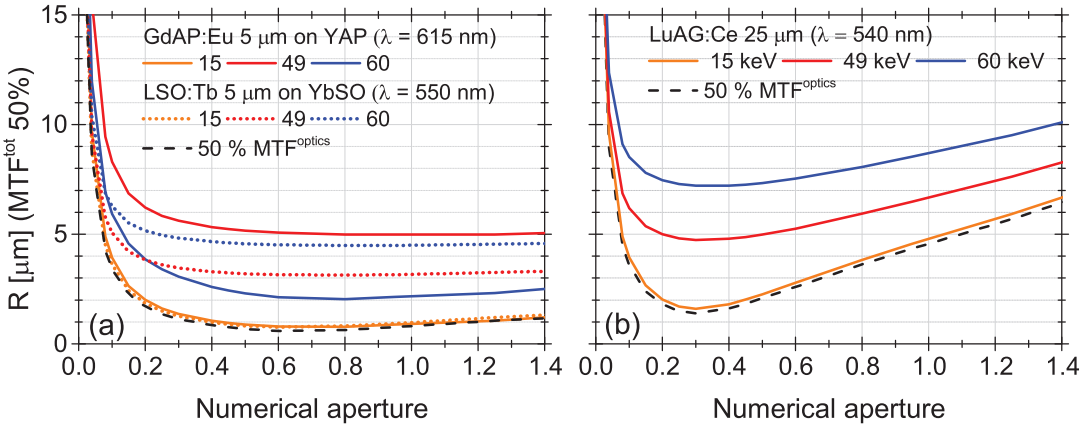

Figure 3.6: Spatial resolution limit (R) calculated as 50 % of MTF^{tot}. As a reference, the spatial resolution from MTF^{opt} (light diffraction and defect of focus) is also reported (dashed black lines). (a) LSO:Tb 5 μm on YbSO and GdAP 5 μm on YAP, (b) 25 μm LuAG:Ce free-standing.

MTF^{opt} correctly approximates MTF^{tot} at 15 keV, but it overestimates the resolution at higher energies.
Up to NA = 0.15 the optics response is the same for all the considered scintillators, since the DoF is thicker than the thicknesses. Consequently, at low energy the response of the system is the same for all the considered scintillators, while at high energy it is determined by the scintillator response. For example at 49 keV, due to the YAP substrate fluorescence a 5 μm thick LSO film outperforms a GdAP film with the same thickness, and a 25 μm thick LuAG film will do so too for low and medium numerical apertures (NA $<$ 0.6). At high numerical aperture the thick LuAG degrades the resolution because of the out-of-focus light, making the thin film more performant, even considering the fluorescence of the substrate.
Due to Gd K-edge GdAP gives, among the investigated scintillators, the best resolution at 60 keV. A spatial resolution of 2 μm can be obtained by choosing a GdAP film, while it is limited between 4.5 and 8 μm choosing 5 μm thick LSO or 25 μm thick LuAG.

3.3 Experimental validation

3.3.1 The detector's modulation transfer function

Measuring the MTF of a high spatial resolution detector is not a trivial task, especially at high X-ray energies. Firstly, the detector system needs to be carefully optimized. For example, the MTF may be degraded by an error in the focus positioning or by a tilt angle of the scintillator with respect to the optics and the camera. Additionally, the MTF measurement requires a test object with details in the size of the spatial resolution limit (≤ 1 μm in our case) which is also sufficiently absorbing.
Resolution chart with sub-micrometer size details are commercially available. These test patterns are useful to get an idea of the spatial resolution and the quality of the image, but their absorption at high energy is limited due to their thickness and they only give a qualitative idea of the contrast as a function of the spatial frequency. For example, a fraction of the JIMA-C006-R:2006 micro resolution chart is shown in figure 3.7. This chart contains details ranging from 0.4 to 15 μm and the absorbing material is made of 1 μm thick tungsten, which attenuates only 10 % of the X-rays at 20 keV.

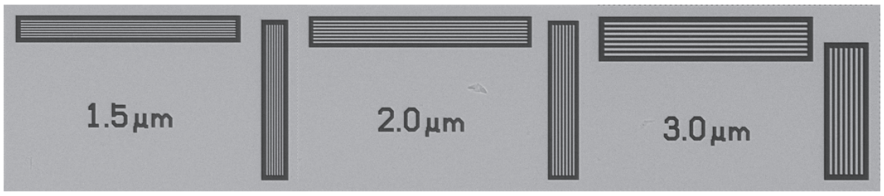

Figure 3.7: Example of an image of the JIMA-C006-R:2006 resolution test pattern obtained by X-ray imaging at 15 keV, using a high-resolution detector.

Alternatively, the MTF can be obtained by the slanted edge method (23, 24) in which the LSF and the MTF are evaluated from the dark-light transition extracted from the image of a sharp edge. For sub-micron resolution, the quality of the edge is extremely important. A cleaved edge should be selected, since even a careful polishing may introduce artifacts (for example, rounding of the edges) which would limit the high-frequency values of the MTF. Moreover, the edge has to be carefully aligned, perpendicularly to the X-ray beam, to avoid that the MTF is affected by the non-complete absorption of incident X-rays at the edge corners. We chose the slanted edge technique to validate the simulation results since it allows us to directly measure the full MTF response and because it is more suitable for higher energies than the resolution chart. A cleaved 0.9 mm thick gallium arsenide edge has been selected for the measurement.

The setup of the experiment including the last set of slits, the edge with its alignment stage and the high-resolution detector are visible in figure 3.8.
The measurements were performed at the ESRF beamline BM05. The X-ray energy is selected in the optical hutch using a multilayer monochromator ($\Delta E/E \approx 10^{-2}$). To reduce the divergence of the beam, two pairs of slits are located before and after the monochromator. A third pair is positioned a few centimeter before the setup (figure 3.8). The edge is positioned as close as possible to the scintillator, at a distance of approximately 2-3 mm, mounted on high precision motors that allow the alignment of the tilt angle and the position of the edge in the X-ray beam. Ideally the edge should be in contact with the scintillator, firstly to reduce the effect of the remaining beam divergence that may degrade the spatial resolution and lastly to remove the phase contrast. However, this is not possible due to the alignment requirement of the edge tilt angle perpendicular to the beam direction. As a consequence, the effect of the phase contrast can enhance the image of the edge, which improves the experimental MTF compared to the calculated one, especially when the detector is configured to be a diffraction limited system.

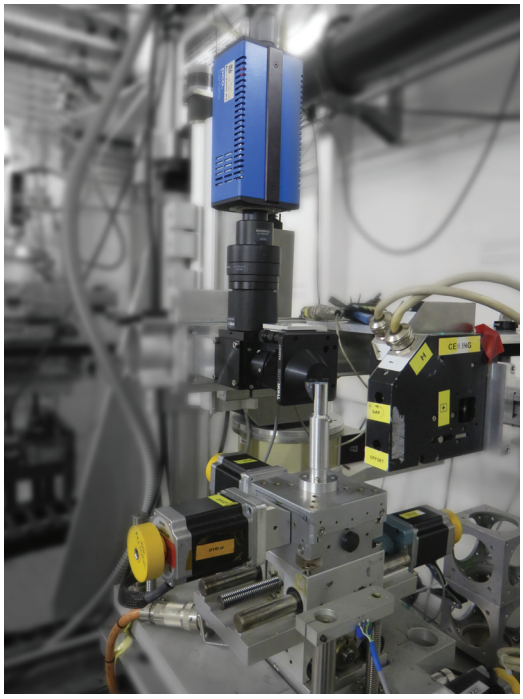

Figure 3.8: Setup for the high-spatial resolution measurement using the slanted edge method.

X-ray energy, scintillator composition and thickness

The measured MTFs at 15 and 30 keV are reported in figure 3.9 (continuous lines) for different scintillators with thicknesses between 1.6 and 25 μm which are combined with microscope optics of numerical aperture 0.45 and 20X magnification. A 3.3X eyepiece is added in the optical path, therefore the final pixel size is 0.11 μm. For $\lambda = 550$ nm, the DoF is 2.3 μm, the resolution limit according to the Rayleigh criterion is 0.74 μm (671 lp/mm) and the cutoff frequency is 1636 lp/mm. The calculated MTFs using the detector's full model, which includes the scintillator response and the optics blurring, are also reported in figure 3.9 (dashed lines). In the case of the thinnest considered

scintillator (LSO:Tb 1.6 μm) the thickness is lower than the DoF, no out-of-focus light degrades the MTF.

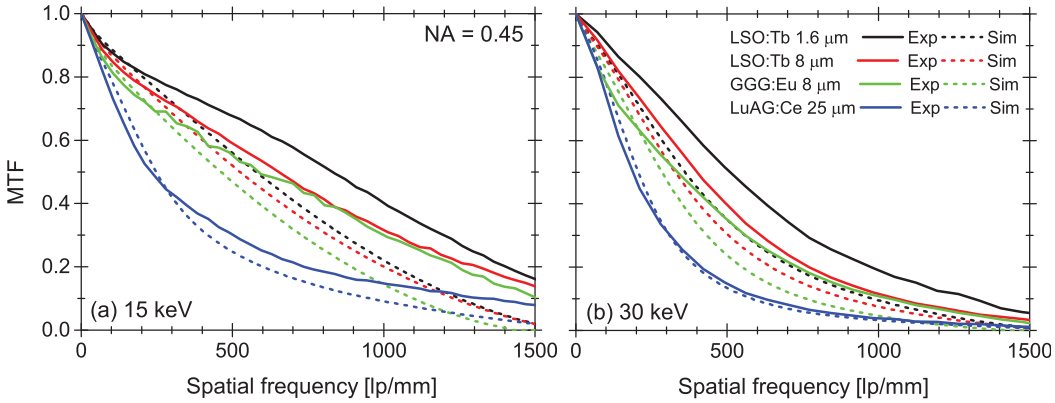

Figure 3.9: Experimentally measured (continuous lines) and simulated (dashed lines) MTFs at (a) 15 keV and (b) 30 keV. Different scintillators are combined with microscope optics of NA 0.45 and the PCO2000 camera. The total magnification is 66X, corresponding to a pixel size of 0.11 μm.

Additionally, the scintillator response of LSO at 15 keV shows much higher values than the MTF calculated by only including light diffraction and therefore, the detector is almost diffraction-limited. This was shown for example in figure 3.4(a) in the case of NA = 0.8. In the case of NA = 0.45, the difference between the scintillator response and the optics response is higher than the difference observed at NA = 0.8, due to the lower cutoff frequency. Therefore, the MTF at 15 keV for the 1.6 μm LSO is mainly limited by the diffraction of light. In fact, the calculated MTF corresponds almost to a straight line approaching zero at the cutoff frequency (1636 lp/mm). However, the measured MTF shows higher values than the calculated one: the resolution limit (contrast equal to 50 %) should be at 0.74 μm (671 lp/mm) according to the Rayleigh criterion, while experimentally it is at 0.60 μm (825 lp/mm). This effect is due to the phase contrast which is not included in the calculation. Due to this the edges in the image are sharper and the contrast is enhanced by approximately 20% at 500 lp/mm compared to the calculated one. By increasing the thickness of the scintillator above the DoF, the out-of-focus light significantly degrades the scintillator's MTF. Although a perfect matching between the calculated MTFs and the simulated ones was not obtained because of the phase contrast, the MTF degradation for increasing thickness is correctly foreseen by the simulations. Additionally, the slight difference between the 8 μm thick LSO and GGG scintillators, due to the different emission wavelength and scintillator response, is

predicted by the simulations and observed experimentally.
At 30 keV (fig.3.9(b)) all the evaluated MTFs are degraded by the scintillator response. Once again, the phase contrast increases the high-frequency MTF values. Therefore the values obtained for the experimental MTFs are higher than for the simulated ones. However, considering the spatial resolution at 15 and 30 keV and calculating the degradation of the spatial resolution ($\Delta R = \frac{R_{15\ keV} - R_{30\ keV}}{R_{15\ keV}}$), as reported in table 3.1, a good agreement between experiments and the simulations can be observed. The difference between experimental and simulated ΔR is ≈ 2 %.

Table 3.1: Degradation of the spatial resolution R from 15 keV to 30 keV. R is evaluated from the spatial frequency where the contrast is 50%, $\Delta R = \frac{R_{15\ keV} - R_{30\ keV}}{R_{15\ keV}}$.

Scintillator	ΔR simulations	ΔR experiment
LSO:Tb 1.6 on YbSO μm	-37.4%	-39.4%
LSO:Tb 8.0 on YbSO μm	-39.1%	-41.8%
GGG:Eu 8.0 on GGG μm	-37.4%	-39.0%
LuAG:Ce 25 free-standing μm	-16.3%	-18.9%

The X-ray fluorescence of the substrate

To further validate our results, the effect of the substrate X-ray fluorescence was experimentally investigated. The MTFs where measured at 16 and 18 keV to observe the differences between the scintillators grown on a Y-free substrate (GGG on GGG and LSO on YbSO) and the ones on substrates containing Y (LuAG on YAG and GdLuAP on YAP). The results are shown in figure 3.10 where the experimental and simulated results are reported using continuous and dashed lines respectively. The high-resolution detector was equipped with microscope optics of 10X magnification and NA 0.4, a 3.3X eyepiece and a PCO2000 camera. The final pixel size is 0.22 μm. As in the previous results, the experimental MTF is enhanced due to the phase contrast. However, as foreseen from the simulations, the MTF curves of all the considered scintillators are similar at 16 keV (fig.3.10(a)) while at 18 keV (fig.3.10(b)) a reduction of the contrast to 80 % in the low frequency range, i.e. below 50 lp/mm, is observed when an Y-based substrate is used. The values of the experimental MTF in this range agree well. For the scintillators that do not contain Y in the substrate, no significant difference can be observed between 16 and 18 keV.

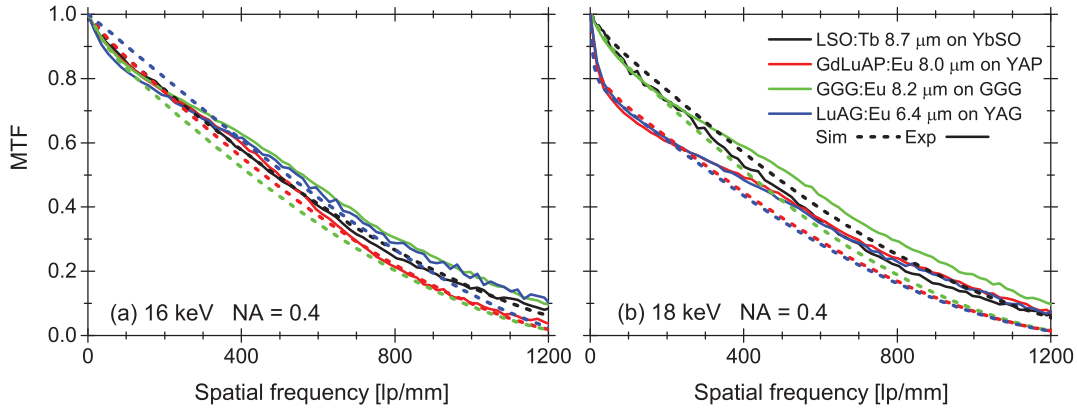

Figure 3.10: Experimentally measured (continuous lines) and simulated (dashed lines) MTFs at (a) 16 keV and (b) 18 keV, for a high-resolution detector equipped with optics of NA 0.4, total magnification 33X, pixel size 0.22 μm.

3.3.2 The non-proportionality of the scintillators

An important parameter in the scintillator characterization is the non-proportionality, which is the nonlinear dependence of the light yield on the X-ray energy (26). Not only does the non-proportionality affect the energy resolution of the scintillator, but it also has to be taken into account for applications that require a quantitative measurement under polychromatic beam conditions, as for example encountered in some fluorescence imaging experiments. Moreover, even for monochromatic beam conditions, the scintillator efficiency should be properly evaluated at the energy that will be selected for the experiment, if the efficiency is strongly non-proportional.

To measure the non-proportionality, the dose deposited in the scintillator needs to be precisely estimated as a function of the X-ray energy. The attenuation coefficient may not be a good approximation of the dose for incident X- and gamma rays, especially when the scintillator size is reduced, as in the case of thin films. In fact, a fraction of the energy of the incoming photons that interact with the scintillator does not contribute to the deposited dose due to the escape of the secondary particles created by the interacting photons. Additionally, the presence of a substrate may increase the dose due to secondary particles that are generated in the substrate and subsequently reach the scintillator where they can be absorbed. Using the developed MC code described in chapter 2, to track the incident X-ray photons and all the secondary particles interacting with the scintillator or with the substrate can give a more precise estimation of the dose. An example of the difference between the attenuation and the deposited dose

was already reported in figure 2.6 for a thickness of 5 μm.
The non-proportionality measurement was performed at the ESRF beamline BM05, where the X-ray energy was selected with a silicon(111) monochromator (ΔE/E $\approx 10^{-4}$). The light yield was evaluated from the average signal from a flat field image (i.e. without objects in the field of view) which was recorded using a high-resolution detector equipped with 2X microscope optics (NA=0.08) and a PCO2000 CCD camera. The 1×1 mm^2 beam size was controlled using a set of slits located a few centimeters before the detector and the X-ray flux was measured using a Canberra 500 μm silicon photodiode. In the energy range 16-64 keV, the photon flux measured on the diode was in the order of 10^9 photons/s/mm^2. Since YAP substrates present a strong emission in the visible range, the GdLuAP samples were measured by placing a bandpass optical filter (central wavelength 634 nm, full width-half maximum 70 nm) in the optical path before the CCD. This ensures the selection of only a part of the Eu emission and removes most of the substrate luminescence. However, a fraction of the substrate emission, corresponding to approximately 10% of the emission intensity of the film, is not filtered and adds to the scintillator emission.
The recorded data for GdLuAP:Eu, LSO:Tb, and GGG:Eu thin film scintillators, as well as YAG:Ce 500 μm bulk scintillators are reported in figure 3.11(a). The spectra are corrected normalized to 1 at 16 keV and corrected by the total amount of incident energy, which is calculated from the measured X-rays flux. The signal intensity for the thin films decreases with the X-ray energy, due to the lower percentage of X-rays that interact with the film, and increases above the K-edges. The signal recorded for YAG:Ce increases from 17 keV up to 30 keV, due to the increasing thickness of the scintillator that contributes to the light emission. Above 30 keV, the thickness of the YAG sample is not sufficient to attenuate the X-rays completely. Therefore, the signal intensity decreases for increasing energy above 30 keV.
The attenuation of the film is calculated using the NIST database (68) and it is used to correct the data reported in figure 3.11(b). The data corrected by the dose deposited in the scintillator calculated using Monte Carlo are reported in figure 3.11(c). Additionally, in the case of GdLuAP, the experimental data has been corrected by subtracting the signal originating from the substrate. This signal has been calculated (1): from the fraction of X-rays not attenuated in the scintillator that are attenuated by the substrate (fig.3.11(b)) or (2): from the dose deposited in the substrate (3.11(c)). As a reference, the uncorrected data are also reported as dashed lines in figure 3.11(b,c).
We can observe that when the data are corrected by the attenuation, the signal sharply increases after the substrate's K-edge (e.g. above 17 keV for GdLuAP and above 61

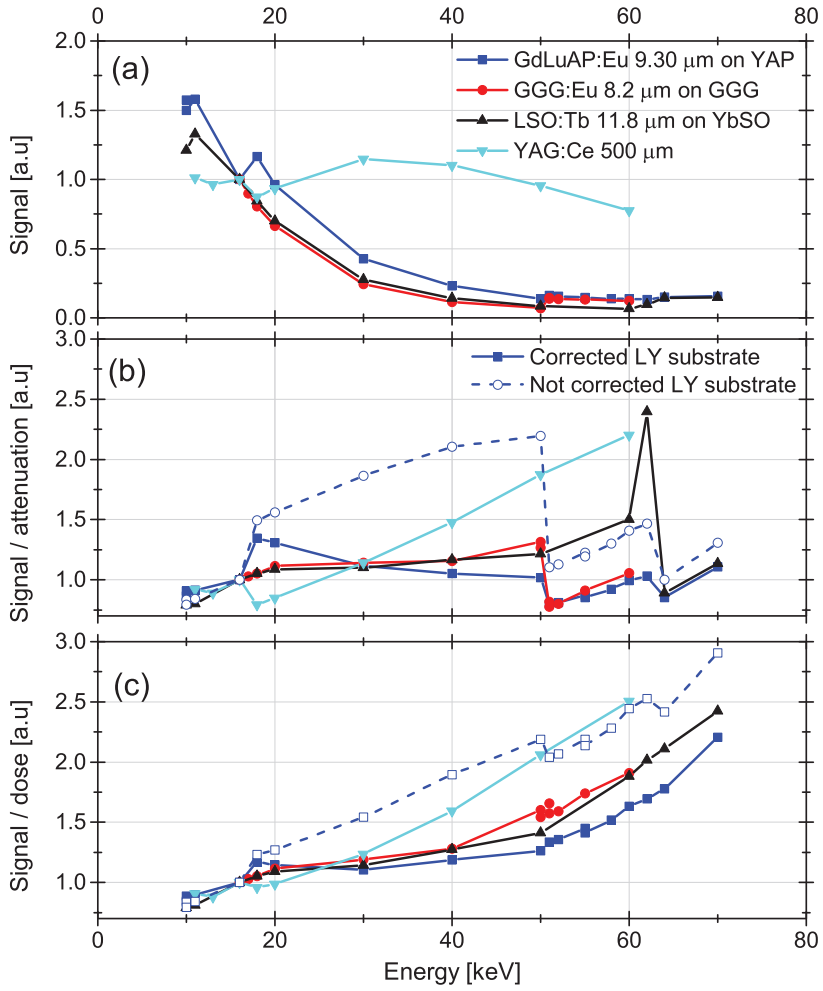

Figure 3.11: (a) LY as function of the X-ray energy, corrected by the X-ray flux and (b) the attenuation of the scintillator (NIST) and (c) the energy deposited (MC, G4). The GdLuAP signal was additionally corrected by the luminescence of the YAP substrate ($LY_{YAP} = 0.1 * LY_{GdLuAP:Eu}$).

keV for LSO) and sharply decreases after the film's K-edge (e.g. above 17 keV for YAG, above 50.2 keV for GdLuAP and GGG and above 63 keV for LSO). These trends are caused, at least partially, by either an underestimation of the dose due to the secondary particles from the substrate, or by an overestimation due to the escape of secondary particles from the thin scintillator. In fact, when the data are corrected by the dose calculated using MC, the jumps in the curve almost completely disappear for YAG, GGG and LSO. In the case of GdLuAP the substrate signal is also subtracted from the data.

Compared to the approximation from the attenuation coefficient, these results confirm the higher accuracy of the dose calculation by Monte Carlo tracking.

3.4 Conclusions

The model presented in chapter 2 was combined with analytical equations describing the optics, keeping the light diffraction and the defocus due to the scintillator thickness into account.

The new model allows, compared to consider separately the scintillator response and the optics blurring, a more precise evaluation of the most convenient detector configuration. This is especially true in the intermediate cases, where none of the involved phenomena prevails. For example, a scintillator thicker than the DoF of the optics can give the same contrast as a thinner scintillator, with the additional benefit of a higher efficiency, if the composition is carefully chosen. Among the considered materials this is the case for a 1 to 10 μm thick scintillator on Y-based substrates compared to thicker free-standing scintillators (10-25 μm), in the energy range 17-50 keV, for low and intermediate numerical apertures (NA < 0.6). The same effect was observed while comparing a 5 μm thick GdAP with a 0.4 μm thick LSO scintillator in the 51-63 keV energy range, even for high NA.
Moreover, reducing the scintillator thickness at high X-ray energy was observed to be beneficial not only to suppress the out-of-focus light, but also to improve the scintillator response. Consequently, the MTF improves while reducing the thickness of the scintillator even below the value of the DoF, which is not the case at low energy.

The detector model was successfully validated experimentally.
The energy deposited in the scintillator calculated using MC was compared with the value of the emitted light at different energies. The model correctly predicts sharp increases or decreases of the LY above the film or substrate K-edges, due to the X-ray fluorescence.
Additionally, the simulated detector's MTF was compared with the experimental data. A good match between experiment and simulations was observed. The experimental MTFs are enhanced by the phase contrast, which is not included in the simulations. However, the degradation of the MTF due to the increase of the X-ray energy, as well as the low frequency drop in the contrast due to the substrate, were correctly predicted.

Chapter 4

Liquid phase epitaxy growth of Gd and Lu aluminum perovskites

4.1 Introduction

Rare-earth aluminum perovskites are good candidates to improve the efficiency of the scintillators while keeping the same spatial resolution because of the high densities and the high effective Z number. In particular, $GdAlO_3$ (GdAP) and $LuAlO_3$ (LuAP) are good scintillator candidates for imaging experiments at relatively high X-ray energies (50-75 keV) due to the position of their absorption K-edges. In chapter 2, Monte Carlo calculations to estimate the absorption efficiency and the MTF response of different SCF scintillators as function of the X-ray energy have been presented. The percentage of the energy deposited by incident X-rays into thin film scintillators has been shown in figure 2.6. The values at 15, 52 and 64 keV are also reported in table 4.1 for perovskites SCFs as well as GGG, LSO and LuAG, highlighting the potential improvement of GdAP based film detectors in the energy range of Gd K-edge.

Table 4.1: Total energy deposited (E_{dep}) in 5 μm thick scintillators calculated for different X-ray energies using Monte Carlo simulations as described in chapter 2.

	GGG on GGG	LSO on YbSO	GdAP on YAP	GdLuAP on YAP	LuAG on YAG
E_{dep} at 15keV	21.11 %	27.85 %	20.13 %	24.73 %	21.02 %
E_{dep} at 52keV	1.28 %	0.94 %	1.40 %	1.38 %	0.76 %
E_{dep} at 64keV	0.87 %	1.14 %	1.02 %	1.09 %	0.75 %

The MTF response has been summarized in figure 2.5. As compared to GGG, GdAP

SCF shows an improvement of approximately 10 % at 500 lp/mm above the Gd K-edge. The contrast obtained for GdLuAP SCF on YAP is almost as high as for GGG on GGG in the range 52-63 keV, and significantly higher in the range 63-80 keV, while it outperforms the contrast obtained for LSO scintillator on YbSO substrate in the range 52-68 keV.

The light yield efficiency of the different scintillator was not kept into account in the model presented in chapter 2, mainly due to the fact that this parameter strongly depends on the growth technology and a precise estimation is not possible before the development of the scintillator. However, an estimation can be done from data found in literature. Rare-earth aluminum perovskites have been reported as good scintillators when doped by appropriate rare-earth ions (72, 73). If comparable light yield to GGG:Eu^{3+} is obtained, increased total efficiency (efficiency = $E_{dep}\times$ light yield) is expected.

GdAP and GdLuAP have therefore been selected for the development as thin film scintillators, on YAP substrates. The bulk growth of YAP is well developed and YAP substrates with good crystalline quality are commercially available at a relatively low price. This condition is required if SCFs are to be used as part of X-ray detectors.

Some results about the LPE growth of $ReAlO_3$ (Re = Y, Lu, Tb) on YAP substrates have been already reported (48). In the frame of X-ray imaging applications, our group at the ESRF has presented results about LuAP SCFs on YAP substrates (74). Optically good GdAP was not successfully grown using bulk techniques (i.e. Czochralsky or Bridgman), but the the possibility of growing GdAP crystals by the flux method has been shown for an other purpose than scintillators (75, 76). The addition of lutetium may play a role in stabilizing the crystal during the growth as well as tuning the absorption efficiency exploiting the K-edges of Lu and Gd. Unlike GdAP, GdLuAP ($Gd_{1-x}Lu_xAlO_3$) has been successfully grown using the Czochralsky method (77, 78).

In the case of the LPE growth the lattice mismatch between the film and the substrate plays a critical role in the crystalline structure and in the luminescence properties of the film. For instance, Kucera at al. (79) report this effect for lutetium and yttrium aluminum garnets, while previously Stringfellow (80) has shown it in the case of $Ga_xIn_{1-x}P$ on GaAs substrates. Since the strategy of this work was the development on YAP substrate, the mixed composition of GdLuAP was also exploited to reduce the mismatch and improve the crystal quality.

The LPE growth process for GdAP and GdLuAP on YAP substrates using a PbO-B_2O_3 flux has been developed. The growth conditions and the crystal structure are presented in this chapter, while the scintillation and X-ray imaging properties will be introduced

in the next one.

4.2 GdAP and GdLuAP liquid phase epitaxy

Experimental

GdAP and GdLuAP epitaxial single crystalline films were grown using LPE on YAP substrates of crystallographic orientation (001), (100) and (011) (defined in the Pbnm space group), produced by the Czochralsky method by MaTeck GmbH, Neyco and Scientific Materials Corp. Several series of samples of undoped and Ce, Tb or Eu doped films were grown from a PbO-B_2O_3 flux using Gd_2O_3, Lu_2O_3, Al_2O_3, Eu_2O_3, Tb_4O_7 and Ce_2O_3 5N pure starting powders. The melt was contained in a Pt crucible and the growth was performed by the isothermal vertical dipping method (81). The sample was attached to a Pt sample holder, which rotated during the growth at a speed of 70 rpm, with alternate direction of the rotation every 5 s. The thicknesses of the films were determined by weight measurement and ranged from 0.3 to 30 μm. The growth was performed at temperatures between 980 and 1080°C resulting in growth rates in the range 0.05 to 2.34 μm/min.
More explanation about the liquid phase epitaxy technique for optical materials can be found in (44) and (45).

Results

Figure 4.1 shows the concentration triangle for the pseudo-ternary system of the melt. The system composed by Pb, B, Al, Gd and Lu is reduced to a pseudo-ternary system on the three axes of which the relative atomic concentration of Pb+B (flux), Al and Gd+Lu is reported. The round marks represent the conditions in which the growth of an aluminum perovskite film covering the overall surface of the substrate was achieved, regardless of the quality of the film (figure 4.2a-4.2b). The color represents the ratio R_{Lu}. The melt is stable when the atomic ratio $\frac{Pb}{B}$ is kept between 5 and 6, meaning that the growth speed is linear with the temperature (and repeatable over different samples) and no spontaneous crystallization at the surface of the melt or on the stirrer is observed. The black crosses indicate the melt concentration where the crystallization of islands (with a different composition with respect to the film) was observed (figure 4.2e-4.2f). Along the vertical orange dashed line the atomic concentration of Al and Gd+Lu in the melt agreed with the stoichiometry of the perovskite phase (i.e. $R_{Al} = 1$).

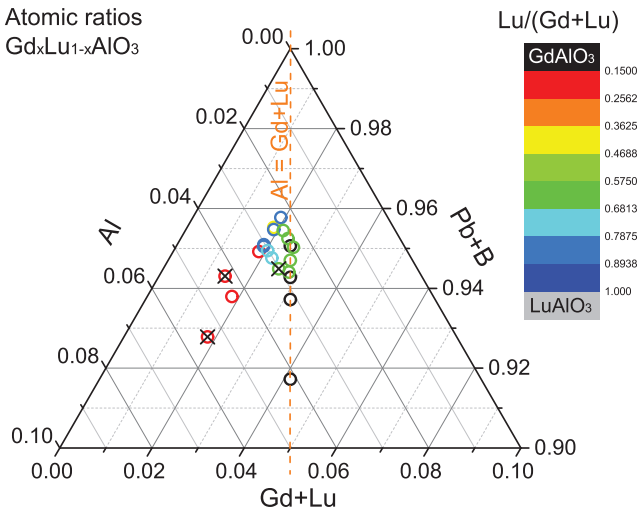

Figure 4.1: Concentration triangle of the pseudo-ternary system Gd + Lu, Al, Pb + B studied for the LPE growth of $Gd_xLu_{1-x}AlO_3$ on $YAlO_3$. The color of the round marks indicated the $\frac{Lu}{Gd+Lu}$ ratio. The black crosses indicate when the crystallization of islands is preferred to the film growth.

The growth parameters and the Al, Gd and Lu relative concentration in the melt are reported in table 4.2. When islands were crystallized together with the film, the thickness and the growth rate is not reported, due to the lack of precise evaluation by the weighing method.

Table 4.2: Atomic ratios between Gd, Lu and Al in the melt ($R_{Lu} = \frac{Lu}{Gd+Lu}$ and $R_{Al} = \frac{Al}{Gd+Lu}$, obtained structure (Str.) (f = film, i = islands), thickness (Th.) and growth rate (G.R.) for LPE growth of $Gd_xLu_{1-x}AlO_3$ on YAP. When islands were crystallized, the thickness and the growth rate is not reported due to the impossibility of a precise evaluation by weighing method.

R_{Lu}	R_{Al}	Str.	Th.[μm]	T[°C]	G.R.[$\frac{\mu m}{min}$]
0	1	f	4.2-27.8	1030±40	0.4-2.78
0.2	1.73-2.38	f	0.4-5.3	1050±10	0.05-0.49
0.2	2.97	f+i	-	1060±10	-
0.4	1.38	f	0.3-21.0	1010±10	0.03-1.38
0.55-0.58	1-1.05	f	1.0-23.0	1015±10	0.15-2.3
0.65	0.95-1.15	f+i	-	1010±20	-
0.85	1.21-1.61	f+i	-	1010±15	-

The best optical and structural morphology was obtained for R_{Lu} between 0.55 and

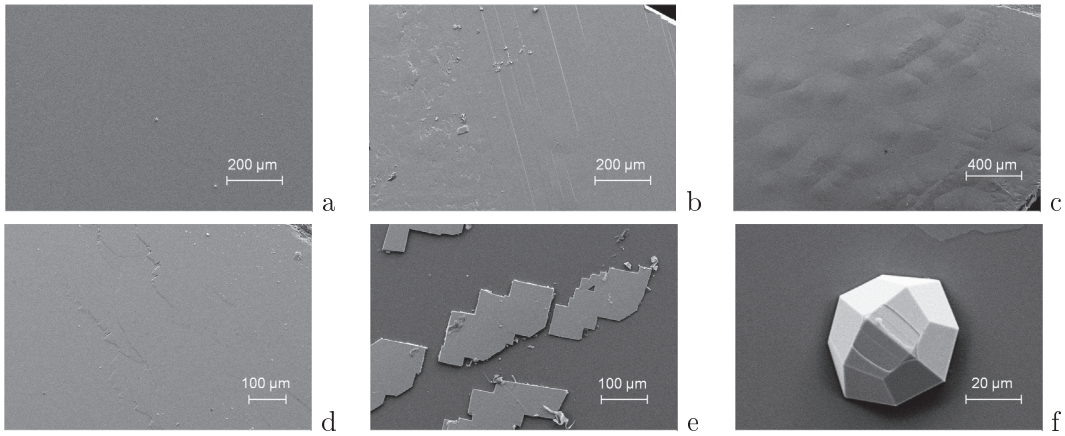

Figure 4.2: SEM images of different surface morphologies obtained for different conditions. (a),(b): $Gd_{.45}Lu_{.55}AlO_3$ film (low lattice mismatch with the substrate) for substrates from different suppliers. (c),(d): $Gd_{.10}Lu_{.90}AlO_3$ film (high lattice mismatch with the substrate) for substrates from different suppliers. (e),(f): Island growth in the case of excess Al concentration in the melt.

0.58. In figure 4.3(a), the growth speed for different substrate orientations is reported as function of the temperature. The samples are grown from the same melt where R_{Lu} was fixed at 0.55. Small variations from the expected linear dependence in the growth speed can be observed: these variations are expected, considering the gradual change of the melt composition, due to its evaporation and due to the Eu_2O_3 additions performed to optimize the dopant concentration.

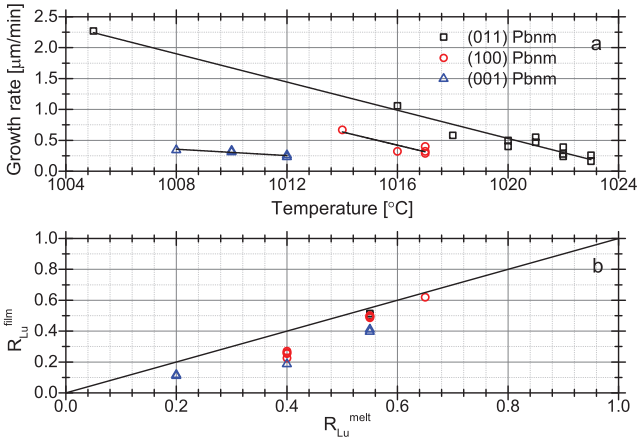

Figure 4.3:
(a) Growth rate of the film as a function of the temperature, for $R_{Lu}^{melt} = 0.55$.
(b) Ratio R_{Lu}^{film} as a function of R_{Lu}^{melt}.

The composition of the film was analyzed using a Castaing Cameca SX50 electron probe micro analysis (EPMA) equipped with tungsten cathode and 4 vertical spectrometers.

The acceleration voltage of the cathode was 22 kV. In figure 4.3(b), the R_{Lu}^{film} (in the film) with respect to R_{Lu}^{melt} (in the melt) is reported for different samples; to highlight deviations, the line corresponds to the case R_{Lu}^{melt} equal to R_{Lu}^{film}. A dependence of the R_{Lu}^{film} ratio on the substrate orientation has been observed. For example, when R_{Lu}^{melt} is equal to 0.55, the Lu concentration in the film is considerably lower for the (001)-oriented samples than for (100) and (011) oriented samples, respectively. We assign this effect to the growth temperature: in order to have a growth rate of 0.3 $\mu m/min$, the required temperature for the (001)-oriented substrates is $\approx 12°C$ lower than for the (011)-oriented samples. In addition, for all the studied samples, R_{Lu}^{film} is always lower than R_{Lu}^{melt}. This effect need to be taken into account in order to control the lattice mismatch and therefore, the film optical quality and crystal morphology.
The concentration of Pb and Pt impurities is close to the EPMA sensitivity, therefore was measured using the X-ray fluorescence technique (XRF), for three different GdLuAP samples grown on YAP substrates (011), (100) and (001) oriented. The three samples were grown from the optimized melt composition (i.e. $R_{Lu} = 0.55$, Pb/B = 5.20-5.30). The measure was performed using a Rigaku Primus II wavelength dispersive XRF system equipped with Rhodium X-ray tube. The results are reported in table 4.3.

Table 4.3: Atomic ratios of the impurities content (Eu, Pb, Pt) in three different GdLuAP thin films, (011),(100) and (001)-oriented respectively. The different ratios are defined as $R_X^{film} = \frac{X}{Gd+Lu+Eu+Pt+Pb}$. The concentration of Eu in the melt $R_{Eu}^{melt} = \frac{Eu}{Gd+Lu+Eu}$ and the ratio $R_{Eu}^{melt}/R_{Eu}^{film}$ are also reported.

	GdLuAP (011)	GdLuAP (100)	GdLuAP (001)
R_{Pb}^{film}	0.04 %	n.d.	0.01 %
R_{Pt}^{film}	0.04 %	0.10 %	0.50 %
R_{Eu}^{film}	1.17 %	1.25 %	1.88 %
R_{Eu}^{melt}	1.33 %	1.33 %	1.73 %
$R_{Eu}^{melt}/R_{Eu}^{film}$	0.88	0.94	1.08

The Pb content was found to be lower than the XRF sensitivity for the (100) oriented sample, while for the other two samples was 0.01 and 0.04%. The Pt contamination is comparable with the Pb content for the (011)-oriented sample and significantly higher for the other two. The highest Pt contamination was found for the (001)-oriented sample, which also corresponds to the orientation showing the lowest light yield efficiency (see next chapter).

4.3 GdLuAP-YAP lattice mismatch minimization

The GdLuAP single crystal films growth was performed by LPE on YAP substrates with different orientations. The lattice parameters of the film were tuned by a careful optimization of the film composition to reduce the mismatch with the substrate. X-ray diffraction techniques were used in combination with electron micro probe analysis and electron microscopy to improve the growth conditions and the film crystallographic and optical quality.

Experimental

The surface morphology was investigated using a LEO 1530 scanning electron microscope (SEM).
The crystallographic structure of the GdAP or GdLuAP films and the lattice mismatch with the YAP substrate have been evaluated using X-ray diffraction (XRD) on a vertical reflectometer at the BM05 beamline at the ESRF (Grenoble). The X-ray energy was set to 15 keV using a double crystal Si(111) monochromator. The diffraction spectra were recorded using a silicon diode. The in-plane diffraction experiments were carried out using a six circle z-axis diffractometer installed at the ID03 beamline of the ESRF (Grenoble) (82). The sample was kept in an Argon flow during the experiment in order to prevent damages induced by oxygen and ozone. In order to be able to penetrate the film and identify the crystallographic orientation of the substrate the energy of the incident beam was 24 keV. The data were acquired using a Maxipix detector, data reduction and analysis have been performed using BINoculars (83).

Results

By varying the Lu percentage in the melt composition, and therefore in the film, different surface morphologies have been observed (figure 4.2). Depending on the substrate orientation, an optimal concentration of Lu and Gd in the melt leads to a homogeneous film surface (figure 4.2a), while for a different melt composition the film surface is wavy (figure 4.2c) and the optical quality of the film is not good enough for imaging. The best results were obtained for R_{Lu} between 0.5 and 0.6.
The optical quality of the film, which is strictly connected to the crystalline quality and to the surface morphology, depends on the lattice mismatch between the substrate and the film. In table 4.4, the lattice parameter values for GdAP (84), LuAP (85) and YAP (86) single crystals are reported: the calculated mismatch between GdAP (or LuAP) and YAP is different in the three crystallographic directions due to the orthorhombic

structure. A significant mismatch reduction can be achieved for $Gd_xLu_{1-x}AlO_3$ for x ≈ 0.5.

Table 4.4: Lattice parameters of GdAP, LuAP and YAP single crystals from literature (84, 85, 86) and calculated lattice mismatch. Lattice parameters in Å.

	a	b	c	cell vol.
GdAP (84)	5.2537	5.3049	7.4485	207.5923
LuAP (85)	5.0967	5.3294	7.2931	198.0957
YAP (86)	5.1803	5.3295	7.3706	203.4895
GdAP-YAP	+1.417 %	-0.462 %	+1.057 %	+2.016 %
LuAP-YAP	-1.614 %	-0.002 %	-1.051 %	-2.650 %
$Gd_{.5}Lu_{.5}AP - YAP$	-0.098 %	-0.232 %	0.003 %	-0.317 %

Figure 4.4 shows the omega-2theta scans at 15 keV around the (400) symmetric reflection for the (100) oriented samples (a) and around the (002) symmetric reflection for the (001) oriented samples (b). The ratio between the diffracted intensities of the substrate and the film is not constant among the different samples, due to differences in film thickness, composition and crystal structure. The lattice mismatch has been evaluated from the distance between the GdLuAP diffraction peak and the YAP diffraction peak: the measured value of the lattice mismatch for different samples is reported in figure 4.5, as a function of the R_{Lu}^{film}. Since the composition was not measured for every samples, the composition of the films grown at the same melt concentration was approximated to the composition of the measured samples. However, a slight difference in the R_{Lu} ratio between different samples can be observed, mainly due to differences in temperature and growth rate. This effect has to be taken into account as source of error for the results reported in this plot.
As expected, the distance between the two peaks reduces going towards $Gd_{0.45}Lu_{0.55}AlO_3$. However, the minimum mismatch in the two directions does not occur at the same film composition.
We can observe in figure 4.4 the broad and asymmetric peaks related to the films. Such a peak shape (asymmetric, broader) is typical for quasi-heteroepitaxial growth with relatively large lattice mismatch (above 1%). It indicates a worse structural quality of films due to some deviations in their content, plane orientation, and formation of the film/substrate transition layer. Thus, the SCF is still single crystalline but possesses a worse structural quality than in the homo-epitaxy case (figure 4.4, left column, graphs for $Lu_{0.55}Gd_{0.55}AlO_3$: Eu sample). In the right column for this R_{Lu} the peaks from the substrate and the film strongly overlap and resemble as a broader peak. Together with

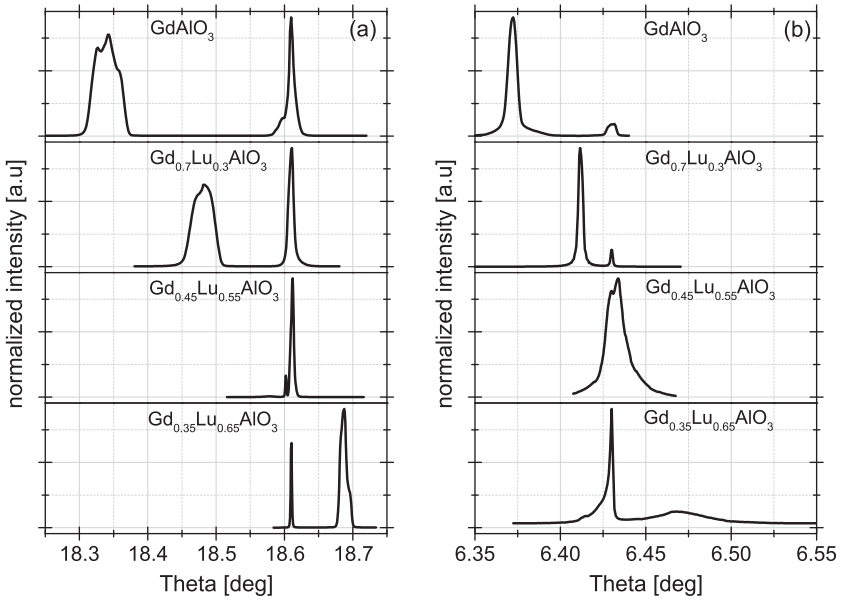

Figure 4.4: Omega-2theta scans for different films of $Gd_xLu_{1-x}AlO_3$. (a): scans around the 400 reflection, YAP substrate (100)-oriented, substrate peak at 18.56°. (b): scans around the 002 reflection, YAP substrate (001)-oriented, substrate peak at 6.43°. The approximate composition of the film is reported in the legend, 15 keV X-ray energy.

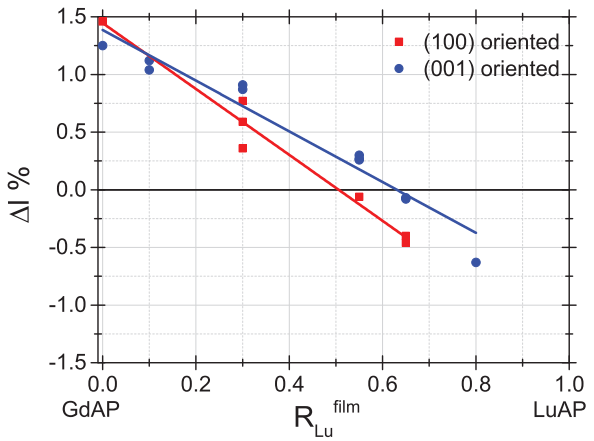

Figure 4.5: Lattice parameter mismatch between the YAP substrate and the $Gd_xLu_{1-x}AlO_3$ film ($\Delta l = \frac{l_{film}-l_{substrate}}{l_{substrate}}$), evaluated along the direction perpendicular to the surface by XRD; the composition was measured by EPMA.

the reduction of the lattice mismatch, a reduction of the width of the diffraction peak of the film was observed, indicating an improvement of the film's crystal structure. This effect is confirmed by the evaluation of the rocking curve (RC): in figure 4.6, the RC for the substrate and the film is reported for two different samples, grown on the

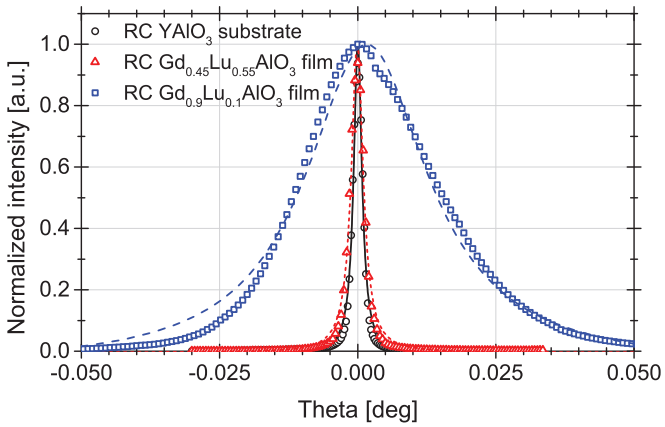

Figure 4.6: Rocking curves around the (002) reflection for GdLuAP films and YAP substrates,(001)-oriented. The spectra have been shifted to set the maximum of the peak at 0°. Red triangles correspond to the case of the low lattice mismatch ($Gd_{0.45}Lu_{0.55}AlO_3$) and the blue squares to the high lattice mismatch case ($Gd_{0.9}Lu_{0.1}AlO_3$).

same kind of substrate and at the same conditions, except for the different R_{Lu} ratios. In the case of $Gd_{0.9}Lu_{0.1}AlO_3$, R_{Lu} is equal to 0.2 in the melt, $\Delta c \approx +0.8\%$ along the (001) direction and the observed peak for the film is much larger than the substrate, indicating that the crystallinity is deteriorated with respect to the one of the substrate. On the contrary, the RC of $Gd_{0.45}Lu_{0.55}AlO_3$, R_{Lu} is equal 0.55 ($\Delta c \approx +0.25\%$) and the diffraction peak width is similar to the one of the substrate, indicating a similar crystallinity. The setup mounted on the beamline BM05 only allows the study of the symmetric Bragg reflections, i.e. the families of planes parallel to the crystal surface. To confirm that the film is a single crystal and not a polycrystal with a preferred grains orientation perpendicularly to the surface, in-plane Bragg reflections were also studied, using the diffractometer at the beamline ID03. The X-ray beam impinges on the sample with a small angle respect to the sample surface (grazing incidence geometry). To separate the potential contribution of the substrate and the film X-ray diffraction response, out of plane diffraction experiments were repeated at different incidence angles. The results are presented in figure 4.7. Since lower incidence angles favor the film response, the film diffraction peak originating from the film can be clearly identified. Diffraction rings or additional peaks were not observed, demonstrating that the film is a single crystal and is oriented as the substrate.

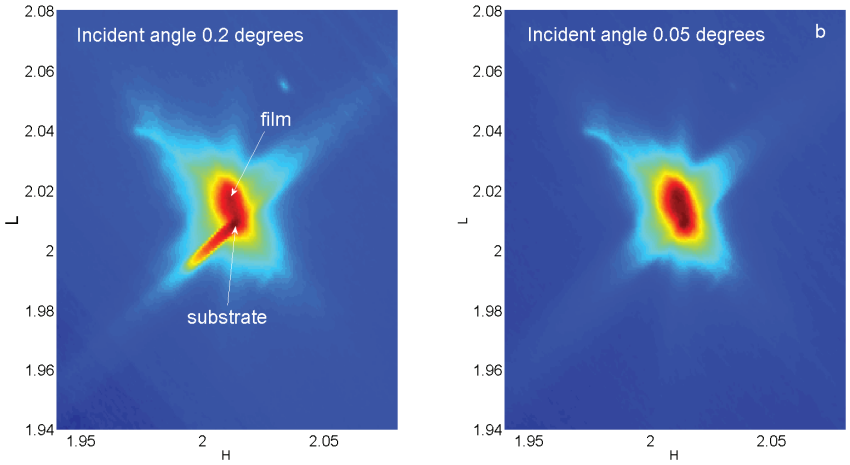

Figure 4.7: Reciprocal space map around the (212) reflection for $Gd_{0.45}Lu_{0.55}AlO_3$ film on YAP substrate (001)-oriented, recorded at 24 keV. To enhance the substrate and the film contribution the maps have been recorded at incident angle 0.2° (left) and at incident angle 0.05° (right).

4.4 Film thickness evaluation

In the LPE process many films are grown from the same melt. Between the growths of two samples, the melt is homogenized using a Pt stirrer for at least two hours. Afterwards, the melt requires approximately 1 hour to stabilize the temperature. The lifetime of the melt, the number of films grown and the delay between two growth processes depends on many parameter as for example the temperature, the melt composition, the crucible size and the setup of the furnace. In the process that was developed at the ESRF, the melt is kept at a temperature in the range 950-1150 ℃ during few weeks. Typically two or three samples are grown every day with a few hours waiting time between them.
The film thickness needs to be determined just after the growth for every sample.
Some techniques often used to determine the thickness of a film are based on optical interference or X-ray reflectivity. However, in the case of the thin film scintillators these techniques can not be easily applied, the first, because the refractive index of the film and the substrate are extremely close and the second, because the film is highly absorbing at small incidence angle. Other techniques damage or destroy the sample. For example, the thickness can be measured using SEM imaging on the sample side, but the sample needs to be cleaved.
The weighting method, i.e. the thickness determination from the weight gain during the growth process, is a quick and cheap way to measure the film thickness. The measurement uncertainty of this method was estimated to be approximately 5 % for 10 μm thick films (44). However, this estimation is valid if the thickness of the two films grown on the two largest surfaces of the substrate is the same and the growth on the edges is negligible.

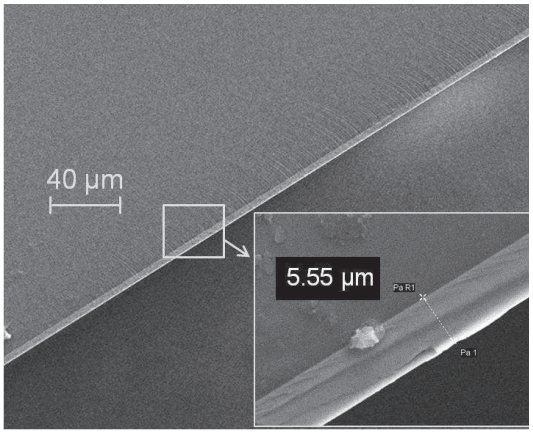

Figure 4.8: Cross sectional SEM image of a GdLuAP film on (001)-oriented YAP substrate. The thickness was found to be homogeneous and the estimation from the SEM image is 5.5 μm, while the thickness determined using the weighting method is 9.6 μm.

In the case of the GdLuAP films, few samples were cleaved and the film thickness was evaluated from cross-sectional SEM microscopy (figure 4.8) and compared with the ones obtained from weighting method. Among the considered orientation, the film thickness evaluated by the weighting method was found to be correct for the (011) and (100) oriented sample, while it was overestimated of approximately a factor 2 for the (001) oriented ones, for a film thickness in the order of 10 μm.
This difference is due to the growth on the edges of the substrate. The GdLuAP films were grown on YAP square substrates. The geometry and crystallographic orientation of the surfaces for the (001) oriented samples is reported in figure 4.9. The two surfaces where the two SCFs are grown have an area of 10×10 mm^2 and are polished down to a roughness of 5 Å. The four substrate edges have an area of 10×0.5 mm^2 and are not polished. Since the total surface where the SCFs are grown (top and bottom) is equal to 10 times the lateral surface, a lateral growth rate equal to 10 times the SCFs growth rate results in an estimation of the film thickness by the weighting method of twice the real value.

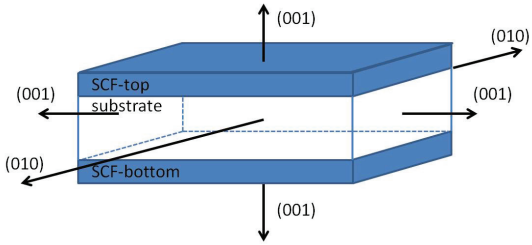

Figure 4.9: Scheme of the geometry and crystallographic orientations for a (001)-oriented GdLuAP on YAP substrate. Two single crystal films are grown on the top and bottom polished surfaces (area = 10×10 mm^2). Lateral growth can be observed on the edges, not polished (area = 10×0.5 mm^2)

The surfaces of the edges are oriented (100) and (010), for (001)-oriented substrate. In figure 4.3(a) the growth rate for GdLuAP SCFs on different substrate orientations is reported as a function of the temperature. The growth rate on the (010) oriented surfaces was not evaluated in this work. We can observe that for a given temperature in the supersaturation range, the growth rate on the (100) oriented surfaces is significantly higher than on the (001)-oriented ones. At 1012 °C, the growth rate is ≈ 0.25 μm/min on the (001) orientation and 1.5 μm/min on the (001). The lateral growth rate can not be precisely estimated from this data, due to the differences in the growth rate on a polished surface as compare to a rough one, and to the missing information about the (010) oriented surface. However, a non-negligible lateral growth is expected for the (001) oriented substrates, which explains the overestimation of the film thickness by weighting method. On the contrary, when the substrate is (100)-oriented, the lateral growth on the (001) lateral surfaces is expected to be close to zero, leading to a correct

estimation of the film thickness by the weighting method.

4.5 Conclusions

A LPE process to grow GdLuAP:Eu SCFs on YAP bulk substrates has been developed, using a $PbO - B_2O_3$ based flux. The improvement of the film crystallographic structure and surface quality with the reduction of the film-substrate mismatch has been demonstrated using X-ray diffraction techniques. Non-negligible contamination of Pt from the crucible have been detected in the SCFs, while the Pb contamination from the flux is less significant.

Chapter 5

Gd and Lu perovskites X-ray imaging properties

The scintillation properties of the newly developed GdLuAP thin films, doped with various rare earth ions, are presented in this chapter. The Eu-doped GdLuAP SCFs have been optimized for imaging and their performances as scintillators for high spatial resolution detectors have been compared with the state-of-the-art Eu-doped GGG SCFs. The effect of the birefringence of the aluminum perovskite crystals on the quality of the image is also presented.

5.1 Scintillation properties

Experimental

To evaluate the light yield (LY), the scintillator was irradiated by 8 keV X-rays and the signal was recorded by a PCO Sensicam camera, combined with 2X optics. The signal intensity was corrected by the calculated absorption of the X-rays in the scintillator and by the sensor quantum efficiency and compared to the signal obtained with a YAG:Ce bulk sample chosen as reference (produced by Crytur). The photoluminescence spectra were measured at room temperature (RT) using a Horiba/Jobin-Yvon Fluorolog-3 spectrofluorimeter with a 450 W xenon lamp and a Hamamatsu R928P photomultiplier. The photoluminescence excitation (PLE) spectra were corrected for the xenon lamp emission spectrum.

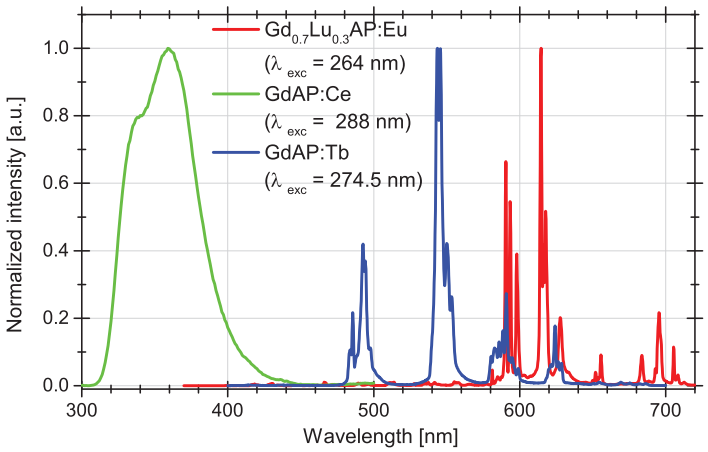

Figure 5.1: Emission spectra of GdAP:Ce, GdAP:Tb and GdLuAP:Eu SCFs under UV excitation (excitation wavelength reported in the plot).

Results

The perovskite SCFs can be doped with various rare earth ions ensuring the scintillation properties. In this work we tested europium, terbium and cerium as activators. In figure 5.1 the emission spectra under UV excitation of GdAP:Tb^{3+}, GdAP:Ce^{3+} and GdLuAP:Eu^{3+} are reported. The dopant concentrations R_X^{melt} in the melt, defined as the atomic ratio $R_X^{melt} = \frac{X}{X+Gd+Lu}$ (where $X = Tb, Ce, Eu$), were 6.3%, 0.5% and 2.0% for the GdAP:Tb^{3+}, GdAP:Ce^{3+} and GdLuAP:Eu^{3+} samples respectively.
The Ce^{3+} doped sample shows a broad UV band due to the electric dipole allowed d-f radiative recombination. The maximum wavelength peaking at 360 nm is typical for the cerium emission in perovskite phases. As shown in XRD, no residual garnet phase can be optically observed. Generally the optical components transmission of high-spatial resolution detectors is close to zero for wavelengths below 400 nm, therefore this dopant was not selected for further optimization in the frame of this work.
Eu^{3+} and Tb^{3+} exhibit the expected emission lines from of the f-f recombination, respectively in the red and green ranges, which is well transmitted by most of the available optics. Note that the divalent europium emission, normally located in the UV-blue region, was not observed. If the various activators can enter in the film, our final aim is to obtain the best light yield, combined with an appropriate emission wavelength and offering a good optical quality for X-ray micro-imaging. So far, we focused on the optimization of Eu^{3+} doped GdLuAP SCFs, with $R_{Lu} \approx 0.55$. As described above, this composition shows the smallest lattice mismatch with YAP substrates. This composition leads thus to the best optical quality SCFs which is crucial for imaging and to

proper scintillation yield evaluation.
Using a standard experimental set-up including a pulsed excitation source operating at 404 nm, we measured the fluorescence decay time of GdLuAP:Eu^{3+} at 614 nm emission wavelength and found a value of 1.49 ms. This means that Eu doped perovskite SCF are suitable for imaging experiments at acquisition frame rate lower than 500 Hz.
In figure 5.2b the LY of different Eu-doped GdLuAP SCFs is reported as a function of the percentage of the reference bulk YAG:Ce LY. Note that the measurement was corrected by the absorption in the film, the light emission of the substrate and the quantum efficiency of the camera. The density being of the same order of magnitude, similar penetration depth of X-rays in the samples is expected, enabling to consider similar light collection efficiency from sample to sample. On the (011)-oriented substrates, the optimized light yield is about 90 % of the YAG:Ce bulk scintillator used as reference. The LY of the GGG:Eu^{3+} SCFs is around 70 % while the currently used LSO:Tb SCF shows a scintillation yield of 100 %. In terms of efficiency, the GdLuAP:Eu SCFs can

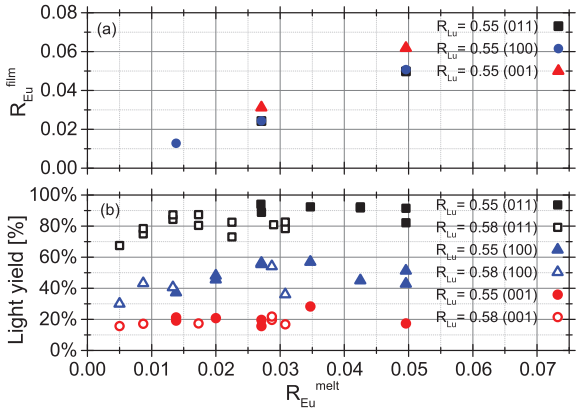

Figure 5.2: (a) Eu concentration in the film R_{Eu}^{film} as a function of the Eu concentration in the melt R_{Eu}^{melt} ($R_{Eu}^{film/melt} = Eu/(Eu + Gd + Lu)$), for $Gd_{0.45}Lu_{0.55}AlO_3$:Eu^{3+} ($R_{Lu}^{melt} = Lu/(Gd + Lu) = 0.55$).
(b) Light yield of $Gd_xLu_{1-x}AlO_3$:Eu^{3+} ($R_{Lu}^{melt} = 0.55 - 0.58$) for different YAP substrate orientations. The emitted light is recorded using a high-resolution setup and the measurement is corrected for absorption and detector quantum efficiency.

therefore compete with the existing SCFs, especially in the energy range 52-63 keV, where the absorption of the Lu-based materials is lower than the Gd-based ones. The figure of merit for 5 μm thick GGG, LSO and GdLuAP is plotted in figure 5.3. The FoM is calculated as in equation 2.2, including the scintillator MTF response and the deposited energy from the MC model described in chapter 2, and the light yield ex-

perimentally evaluated at 8 keV, assuming the scintillators being perfectly proportional with the X-ray energy and flux. The GdLuAP:Eu FoM is 1.3 times higher as compared to GGG:Eu and up to 3.4 times as compared to LSO:Tb in the energy range 52-63 keV, while in the energy range 64-80 keV it decreases down to 0.7 times as compared to LSO:Tb and increases up to 4 times as compared to GGG:Eu. An other important

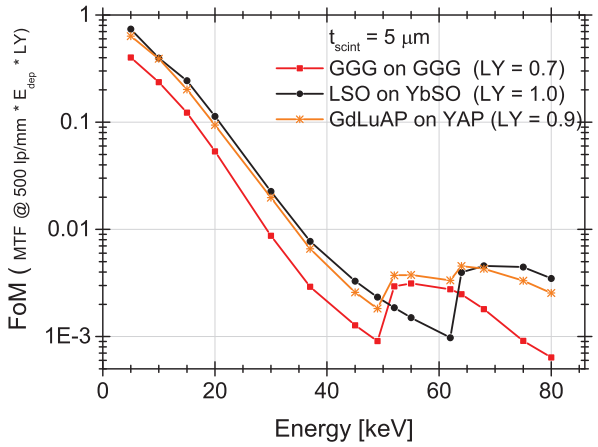

Figure 5.3: Figure of merit including the total efficiency (Deposited energy × LY) and the scintillator spatial resolution (contrast at 500 lp/mm), calculated as in equation 2.2 for 5 μm thick GGG, LSO and GdLuAP scintillators.

aspect to underline in figure 5.2 is the dependence of the GdLuAP:Eu scintillation yield on the crystallographic orientation: it is in fact only 20 % for (100)-oriented samples and 40-60 % for the (001)-oriented ones. For the (001)-oriented samples, keeping into account the overestimation of the film thickness due to the fast lateral growth on the sample borders, the light yield is approximately 30-40 %, still lower as compared to the (011)-oriented samples. The reason for this difference is not yet clear and requires more detailed investigations. So far, we can exclude that it could be due to a different segregation coefficient of Eu and therefore, to a different Eu concentration in the film. The Eu concentration in the films was measured by EPMA and the obtained values are similar for samples of different orientations grown at the same melt concentration (figure 5.2-a). Moreover, the Eu concentration in the melt was varied from R_{Eu}^{film} 0.5 % to 5 %: in this range, no significant variation of the scintillation yield was observed. Therefore, this difference is mainly due to the different strain and defects that could lead to a different efficiency of the energy transfer between the perovskite crystal and the Eu atoms. The Pb and Pt contents were evaluated by XRF on three samples: the results were reported in table 4.3. The Pb content is close to the detection limit and does not seem correlated with the light yield. For the (011)-oriented sample (LY≈90 %) the Pt and Pb content are comparable. In comparison to the (011)-oriented sample, the Pt content is twice higher for the (100)-oriented sample (LY≈40-60 %) and ten times

higher for the (100)-oriented sample (LY≈30 %). A different segregation coefficient of Pt in the film could explain the different light yield. However, more experiments to improve the statistics are needed to confirm this result.

5.2 High-resolution X-ray imaging

The imaging properties of the perovskite SCFs were tested at the ESRF on the beamline BM05. The scintillators were mounted in a high spatial resolution detector, equipped with microscope optics and PCO2000 CCD camera. The scintillators were polished down to 170 μm (total thickness film plus substrate) to match the standard correction for the glass coverslip implemented in most of the commercial microscope objectives.

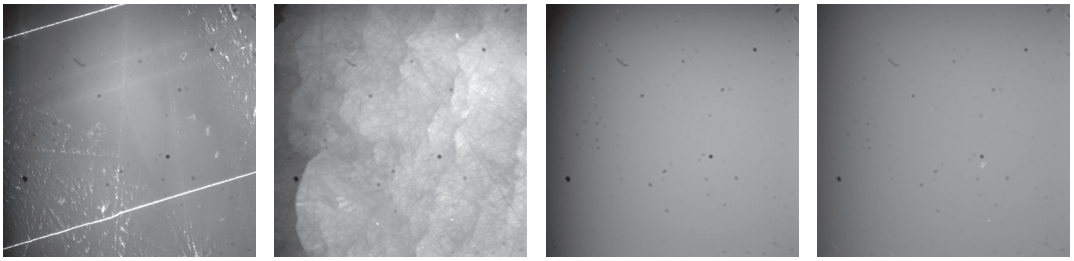

(a) **(b)** **(c)** **(d)**

Figure 5.4: Flat field images at 15 keV using 20X/0.45 optics (Field of view 0.7 mm) (a) GdAP on YAP (b) $Gd_{0.9}Lu_{0.1}AlO_3$ on YAP (c) $Gd_{0.45}Lu_{0.55}AlO_3$ on YAP and (d) GGG on GGG.

In figure 5.4, the flat field images recorded using (a) GdAP:Tb, (b) $Gd_{0.9}Lu_{0.1}AlO_3 : Tb$, (c) $Gd_{.45}Lu_{.55}AlO_3 : Eu$ and (d) GGG:Eu scintillators are compared. When the lattice parameter of the film is not optimized to reduce the mismatch with the substrate, the flat field image is inhomogeneous (a,b) due to the presence of regions where the film is thicker or surface structures leading to light scatter which enhance the light collection from the scintillator. This effect reduces the dynamic range of the detector and the image quality. In the case of the $Gd_{.45}Lu_{.55}AlO_3 : Eu$ SCF, the lattice mismatch is not reduced to zero but it is significantly reduced. However, the flat field (c) is as homogeneous as the one obtained with the homoepitaxially grown GGG:Eu (d) demonstrating that the perovskite film possesses the required optical quality high spatial resolution imaging.
The X-ray radiography of a fly recorded at 12 keV using different scintillators is shown as an illustration in figure 5.5. The flat field correction has been applied to all the

images. When the optical quality of the film is degraded by the lattice mismatch, as in the case of GdAP:Eu SCF on YAP substrate (fig.5.5a), the image is distorted and the small details can not be be clearly identified as in the case of a SCFs with higher optical quality (fig.5.5b). On the contrary, for the GdLuAP:Eu SCFs (fig.5.5c), the image quality is at least as high as the one obtained using a GGG:Eu state-of-the-art SCF. To quantify the image quality, the modulation transfer function was calculated

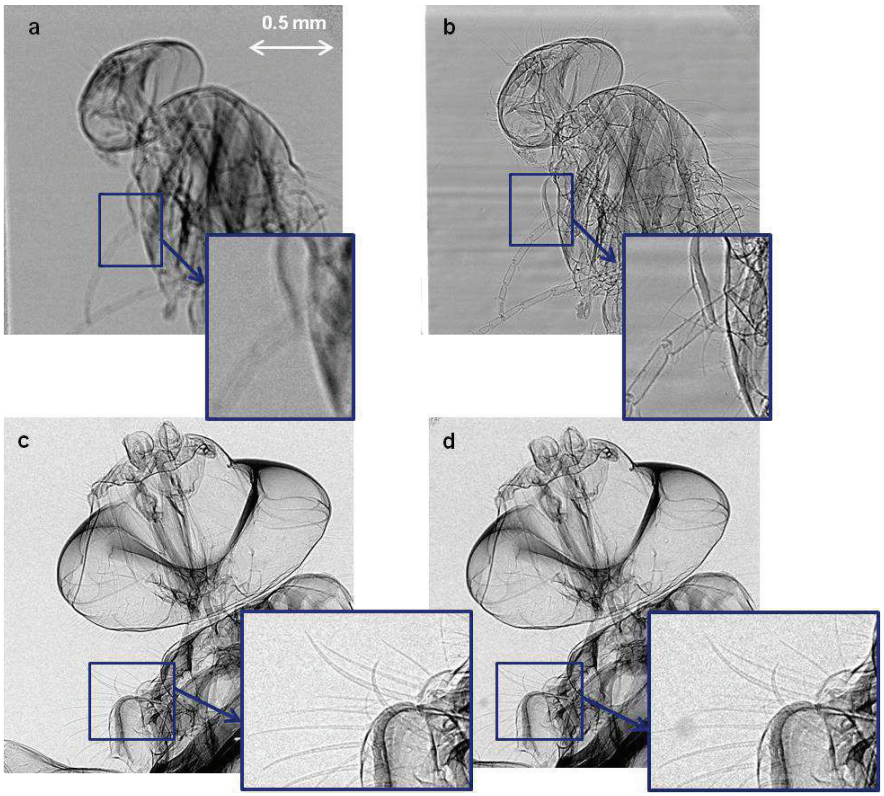

Figure 5.5: Image of a fly with 2X/0.08 microscope objective and (a) GdAP:Tb 17.1 μm, (b) LSO:Tb 5.6 μm, (c) GdLuAP 11.4 μm (d) GGG:Eu 11.2 μm.

from the radiography image of the JIMA micro-resolution chart. In figure 5.6 top, we show few images and deduce the contrast as a function of the spatial frequency for the bulk YAG:Ce, GGG:Eu SCF, the current state of the art, and the new optimized scintillating screen made of GdLuAP:Eu. We clearly show that the combination of the good light yield and optical quality give rise to a contrast improvement in the small spatial frequencies by a factor of 10%.
The result was also confirmed by the MTF measured using the slanted edge technique, reported in figure 5.7.

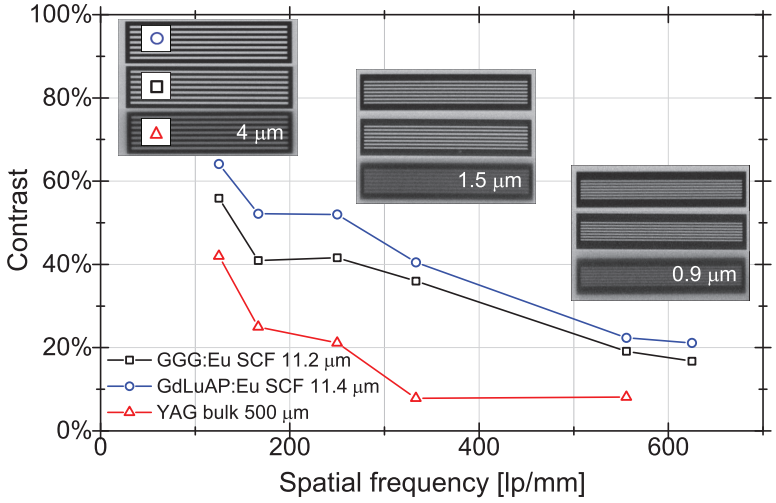

Figure 5.6: Images of a tungsten resolution chart and deduced contrast as a function of the spatial frequency, recorded using a PCO2000 camera coupled with a 20X/0.4 objective at 15 keV.

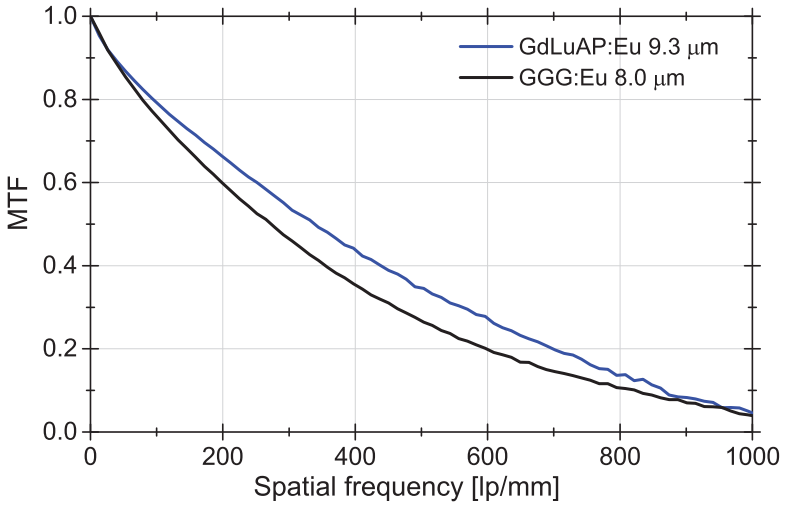

Figure 5.7: MTF curves measured using the slanted edge method at 16 keV, using GdLuAP:Eu and GGG:Eu SCF scintillators. The detector was equipped with 10X/0.4 microscope optics, 3.3X eyepiece and PCO2000 (pixel size 0.22 μm).

The optical quality obtained for the GdLuAP films on YAP is at least comparable to the one of the state-of-the-art GGG SCF scintillator. The possibility of obtaining the optical quality required for high spatial resolution imaging, reducing the mismatch of the film with the substrate tuning the film composition, was demonstrated.

5.3 Effect of the scintillator birefringence on the MTF

Many transparent solids, e.g. glasses, many polymers, or crystals with a cubic structure, are optically isotropic. This means that the index of refraction is the same along every direction in the material, which is caused by the arrangement of atoms, and therefore the electronic structure of the material, being the same along the three axis directions. The interaction of light with an isotropic material does not depend on the angle between the propagation direction of the light and the material axes. The light is refracted at a constant angle, travels at a single velocity and is not polarized by the interactions with the electronic structure.

Crystals with a non symmetric structure are often optically anisotropic: the index of refraction depends on the propagation direction of the light and on its polarization. These anisotropic materials, defined as birefringent, can be uniaxial or biaxial. In the first case an axis can be found around which a rotation of the crystal will not change its optical behavior because all the directions perpendicular to this axis are optically equivalent. This axis is called optic axis and the light propagating along it behaves as the light passing through an isotropic material. Uniaxial material can be described by two indexes of refraction: an ordinary index of refraction n_o, governing the light polarized perpendicularly to the optic axis, and an extraordinary one n_e, governing the light polarized along it. Biaxial materials are characterized by three indexes of refraction n_α, n_β, n_γ and have two optic axes. When the light propagates along a direction different from the optic axes, both polarizations are considered as extraordinary, with two different indexes of refraction. The dependence of the refractive index on the propagation direction of light in an anisotropic crystal is represented by a geometrical figure called an optical indicatrix (87).

The birefringence phenomenon was already observed in 1669 in calcium carbonate (88), with $n_o = 1.658$, $n_e = 1.486$ at 590 nm, one of the crystals presenting the strongest birefringence. Looking at an object through this crystal results in a double image due to the double refraction of the light reflected by the object (5.8(a)). However, the phenomenon was not understood until when A.J. Fresnel described the light in terms of waves including its polarization, more than one century later. Today the phenomenon is widely exploited in various applications, from optical microscopy to medical diagnostics and liquid crystal displays. However, in some fields birefringence can create problems. For example, it is critical for the fabrication of high-resolution UV optics used for semiconductors lithography, for the transparency of ceramic materials and for the spatial resolution obtained when birefringent scintillators are employed for

imaging applications.

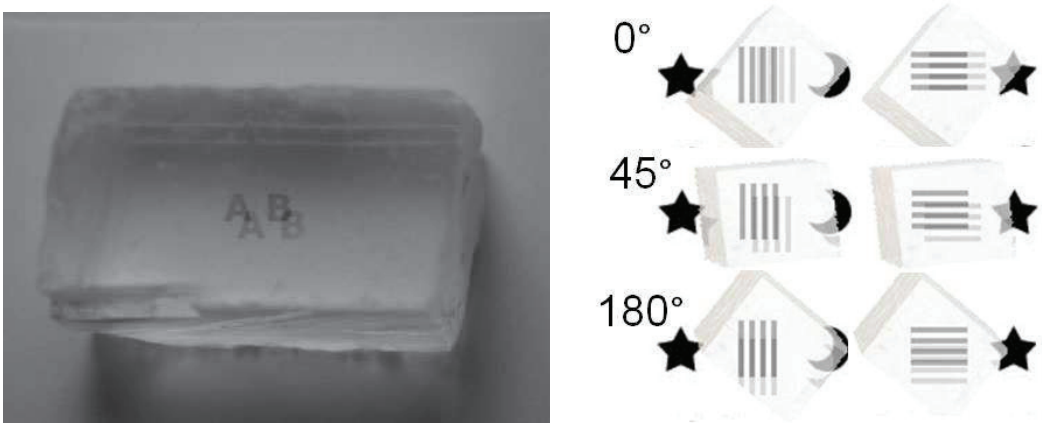

(a) (b)

Figure 5.8: (a) Example of the double image of an object when observed through a calcium carbonate (calcite) crystal. (b) Qualitative examples of the effect of the rotation of the crystal on the image, obtained using the Nikon on line tutorial (89).

The latter also concerns the GdLuAP thin films presented in this work. An example of the effect of the birefringence of a scintillator on the image quality is shown in figure 5.8. Line patterns along two perpendicular directions are observed through a calcite crystal: depending on its orientation, the image of the chart is doubled in a certain direction. For a certain position of the crystal, that we take as 0° reference, the doubling of the image is along the horizontal direction, therefore the resolution is highly degraded along this direction and not affected along the vertical one. When the crystal is rotate 180°, the situation is opposite. For every position between 0° and 180°, the doubling and the resolution degradation will somehow affect both the directions. However, an object is more complex than a resolution chart and contains details in every direction, as for example the fly in figure 5.5. The birefringence will affect some directions more than others, but the overall image quality will be degraded. The example of calcite is well known and often shown as example, since the difference in optical path between the ordinary and the extraordinary rays is well visible by eye for a sufficiently thick crystal. To compare this example with the case of GdLuAP scintillators considered in this work, we should first compare the birefringence B, evaluated as

$$B = n_{max} - n_{min} \tag{5.1}$$

where n_{min} and n_{max} are respectively the lowest and highest refractive index of the material. B is approximately 0.2 for calcite and 0.02 for YAP crystals (90). The difference in optical paths D depends not only on B but also on the distance to traverse, i.e. the thickness t of the crystal:

$$D = B \cdot t \, . \tag{5.2}$$

D is typically a few mm for a cm thick calcite crystal. Therefore a double image is easily visible by eye (see for example fig.5.8).
Thin film scintillators considered in this work are only 10-20 μm thick, but the visible light image produced in the scintillator also traverses the substrate. Therefore, a total thickness of approximately 170 μm should be considered. YAP is a biaxial crystal, it has therefore three refractive indexes n_α, n_β and n_γ along three optical directions, corresponding to the three crystallographic axes in the case of an orthorhombic crystal structure. By convention, the three refractive indexes n_α, n_β and n_γ are named from the lowest to the highest value to avoid confusion in the case of the monoclinic and triclinic crystal structures, where the optical directions are not parallel to the crystallographic ones. Hence each of the indexes n_α, n_β and n_γ can be associated to each of the lattice parameters a, b, and c. The three refractive indexes at 600 nm for the YAP crystal structure (91) are reported in table 5.1, after correctly associating them to the three crystallographic directions a, b and c. The birefringence B, varies from 0.009 to 0.024 depending on the crystallographic orientation. D is therefore in the order of few micrometers, non-negligible when compared to the spatial resolution we are aiming for.
To study the effect of the scintillator's birefringence on the quality of the images obtained using high-resolution X-ray detectors, the contrast and the spatial resolution were measured for different angles of the scintillator around its surface normal. These measurement were performed using both using both the resolution chart and the slanted edge method. The experiments were performed on the ESRF beamline BM05, at an X-ray energy of 16 keV. The setup of the expriment is the same as the one presented in section 3.3. The high-resolution detector is equipped with microscope optics of numerical aperture 0.4 and 10X magnification, a 3.3X eyepiece and a PCO2000 camera. The pixel size of the whole setup is 0.22 μm.
The measurement performed using the JIMA-C006-R:2006 resolution chart is similar to the example reported in figure 5.8(b). However, for X-ray imaging, the image is not formed by the light reflected by the object. The X-ray flux partially absorbed in the object irradiate the scintillator and produces a visible light image which traverses the scintillator and substrate and it is projected on the CCD camera. Hence, the image

quality does not only depend on the crystal's birefringence, but also on the X-ray beam divergence, the geometry of the investigated object and the spread of the energy deposited in the scintillator. However, by evaluating the contrast along two perpendicular directions while varying the scintillator's rotation angle around its surface normal, we can determine if the birefringence plays a role in the detector's performance.

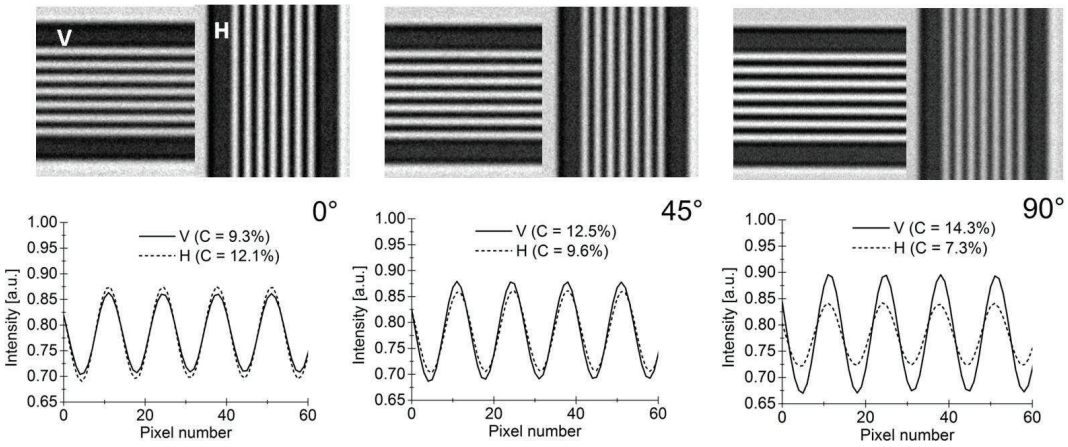

Figure 5.9: X-ray images of the 1.5 μm horizontal and vertical line patterns of the JIMA-C006-R:2006 resolution chart and extracted profiles in the vertical (V) and horizontal (H) direction, for three different angles of the scintillator around its normal. The calculated contrast $C = (I_{max} - I_{min})/(I_{max} + I_{min})$ is reported in the legend. The X-ray energy is 16 keV, the scintillator is a (110)-oriented 11.5 μm thick GdLuAP:Eu SCF on YAP, the microscope optics numerical aperture is 0.4 and the final pixel size is 0.22 μm (10X/0.4 + 3.3X + PCO2000).

In figure 5.9, the images of the 1.5 μm line patterns, as well as the extracted profiles along the vertical (V) and horizontal (H) direction in the image are reported for three different positions (0°, 45° and 90°) of the scintillator around its surface normal. The scintillator is (011)-oriented GdLuAP:Eu on a YAP substrate. The in-plane orientation of the scintillator was not measured. Therefore, the reported angles are relative to the reference 0°, but they should not be associated with a specific crystallographic orientation. It is important to underline that the X-ray beam presents a larger divergence along the horizontal direction than along the vertical, therefore, higher contrast and higher resolution are expected along the vertical direction. However, for a certain scintillator angle (0°), the contrast in the H direction is higher than in the V direction. When the scintillator is rotated 90°, the highest V contrast is obtained. At 45°, an intermediate situation was observed. The contrast measured along V is still higher than along H due to the beam divergence, but the difference between the two profiles

H an V is reduced with respect to the 90° measurement. The same measurement was

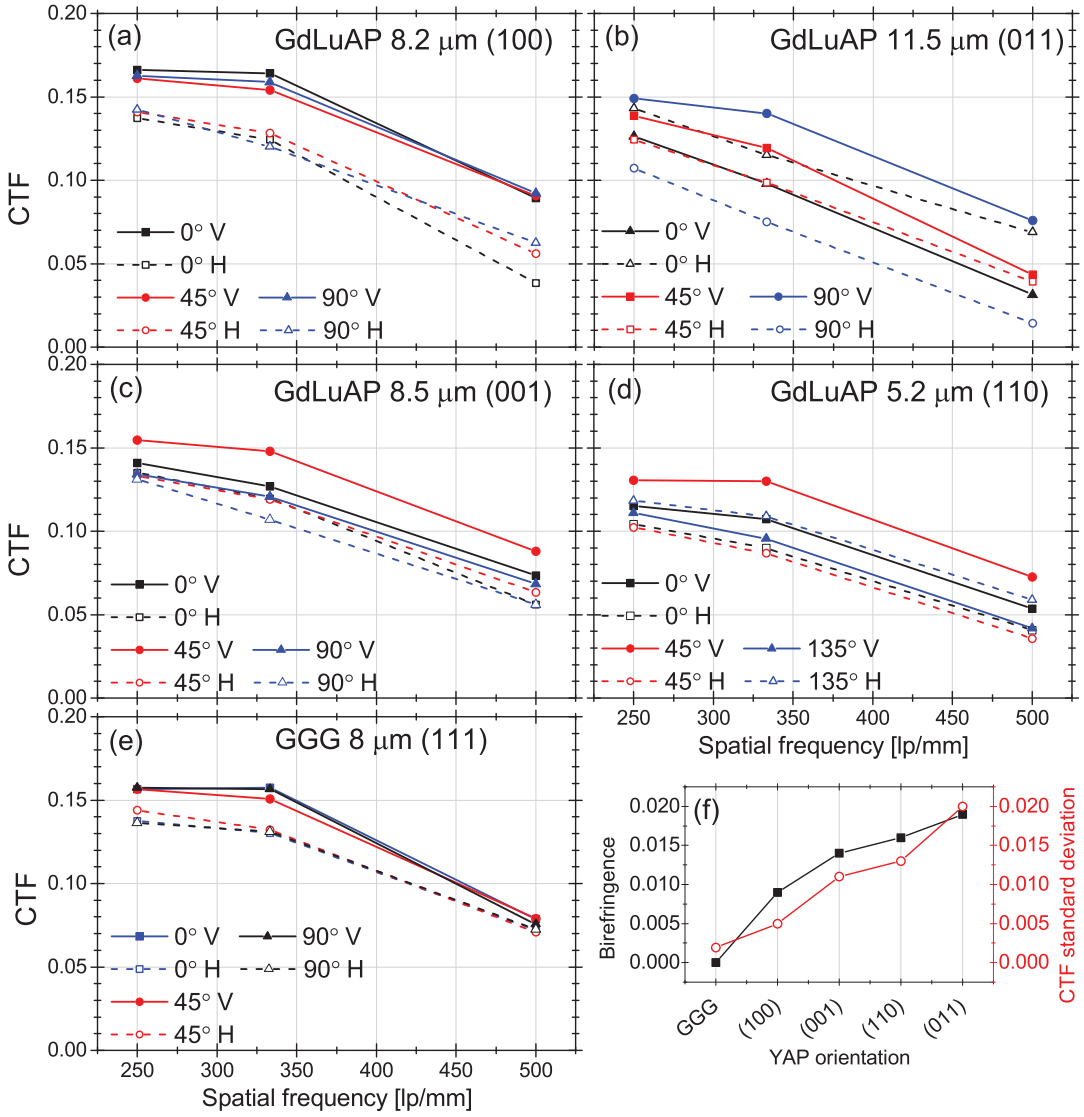

Figure 5.10: (a-e) CTF curves measured using a JIMA-C006-R:2006 resolution chart at 16 keV along two perpendicular directions H and V, varying the angle of the scintillator around its surface normal. (f) Birefringence value and standard deviation calculated for the CTF measurement reported in (a-e). The detector was equipped with 10X NA=0.4 microscope optics, 3.3X eyepiece and CCD camera PCO2000. The final pixel size is 0.22 μm.

repeated for the 1, 1.5 and 2 μm line patterns and the contrast transfer function CTF was calculated. The results are reported in figure 5.10 for (a) (100), (b) (011), (c) (011),

Table 5.1: Lattice parameters and refractive indexes of YAP at 600 nm as reported in (91). Since the crystal structure is orthorhombic the three optical directions correspond to the crystallographic axes. The birefringence (B) is calculated for different crystal orientations (c.o.). GdLuAP:Eu SCFs on the (010) and (110) orientated substrates, reported in gray, were not obtained in this work. The last column contains a quantitative evaluation of the effect of the birefringence as observed from the MTF measurement.

lattice parameter	n	c.o.	B	Impact on the MTF
a = 5.1803 Å	n_γ =1.9505	(100)	0.009	negligible
b = 5.3295 Å	n_β =1.9413	(010)	0.024	not evaluated
c = 7.3706 Å	n_α =1.9268	(001)	0.014	weak
		(011)	0.019	strong
		(110)	0.016	not evaluated

(d) (110) oriented GdLuAP:Eu thin film scintillators. As reference in figure 5.10(e) the result for a GGG:Eu scintillator is also shown. GGG has a cubic crystal structure and it is not birefringent, hence the CTF does not vary with the angle and the difference between the CTF measured along V and H remains constant because it is only due to the different beam divergence. The GdLuAP:Eu (100)-oriented scintillator (a) is similar to GGG:Eu, although a slightly higher dispersion of the CTF values is observed. The CTF values obtained along the H or V direction for the (011)-oriented GdLuAP:Eu strongly depend on the rotation of the scintillator. Additionally, as already shown in figure 5.9, at 0° the contrast measured along the H direction is higher than along the V one, while when the scintillator is rotated 90° the higher CTF along the vertical direction is measured. The same effect was observed for the (110)-oriented GdLuAP scintillator. At 45° the CTF along H is higher than along V, and the maximum CTF along V was measured at 135°. A smaller spread of the CTF values is observed when compared to the (011)-oriented scintillator. Finally, in the case of the (001)-oriented GdLuAP:Eu, the measured contrast is influenced by the angle, but a position where the H contrast is higher than the V contrast was not found.

To quantify the results obtained with the CTF measurement, in figure 5.10(f) we reported the standard deviation on the CTF obtained for the average contrast of the three measurements at three different scintillator angles. In the same plot, the birefringence values calculated from literature (table 5.1) for different YAP orientations are also reported. The results obtained for the CTF measurement are in good agreement with the birefringence values. Among the considered orientations, the (011) is expected to show the highest birefringence and the (100) the lowest one. The (010) should in principle present even a higher birefringence than the (011), but no scintillators were obtained

on this orientation. The (110) and the (001) oriented scintillator show an intermediate effect, in agreement with the calculated B values. The general trend described by the standard deviation well reproduces the increase of the birefringence values from the (001) to the (011) orientation.

To confirm the results obtained with the CTF we also measured the full MTF using the slanted edge method described in section 3.3 varying the angle of the scintillator around the surface normal, for the (011) and (100)-oriented GdLuAP:Eu and for the GGG:Eu SCFs. The condition of the experiment and the detector configuration are the same as used for the measurement using the JIMA resolution chart. The results are reported in figure 5.11. The MTF curves obtained obtained for three measurement at 0°, 45° and 90° using a GGG:Eu SCF are reported to show the uncertainty of the measurement. At 500 lp/mm the average contrast is 0.26 ± 0.02. In the case of the (011)-oriented GdLuAP:Eu scintillator, the MTF curve strongly depends on the rotation of the scintillator. The contrast at 500 lp/mm varies from 0.1 to 0.3 and the average value is 0.19 ± 0.12, lower than the one measured using GGG. However, the best MTF obtained for this orientation shows higher contrast than GGG. For the (100)-orientated SCF the MTF slightly depends on the angle, but the average contrast (0.34 ± 0.05) is higher than the value obtained using the GGG:Eu scintillator.

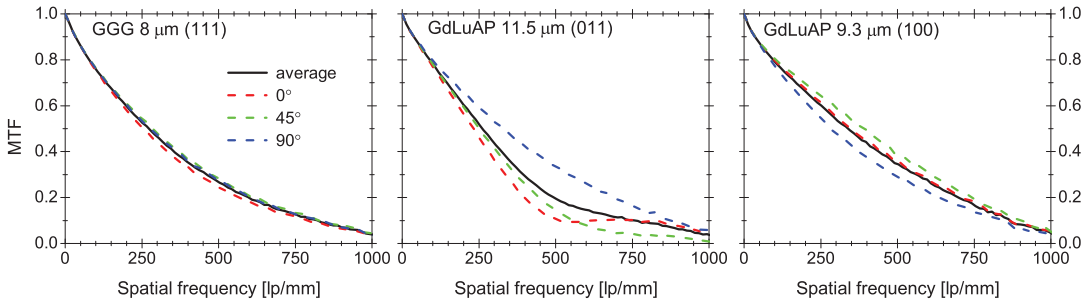

Figure 5.11: MTF curves measured using the slanted edge method at 16 keV, varying the angle of the scintillator around its surface normal. The detector was equipped with 10X NA = 0.4 microscope optics, 3.3X eyepiece and PCO2000. The final pixel size 0.22 μm.

The effects of the birefringence on the image quality has been experimentally measured and correlated with the YAP birefringence values from literature. The scintillator crystal structure and orientation have to be taken into account for the estimation of the MTF of the detector. It is, however, important to underline that these results are strictly connected with the conditions of the experiment. When the spatial resolution is already limited by other phenomena, as for example the energy distribution in the scintillator

at higher X-ray energy, or the out-of-focus light when a thicker scintillator is selected, the effect of the birefringence may become negligible. On the contrary, by selecting a lower X-ray energy and using a detector configuration for higher spatial resolution, the effect may become even more important.

5.4 Conclusions

The feasibility of sub-micrometer resolution X-ray imaging using GdLuAP:Eu have been demonstrated. The light yield depends on the substrate and film crystallographic orientation. For the (011)-oriented samples a light yield higher than the light yield of the GGG:Eu state-of-the-art SCF scintillators was obtained. The figure of merit, obtained from the efficiency of the scintillator and its MTF response, shows that the new GdLuAP:Eu SCF could compete with the existing SCFs, especially in the range 52-64 keV. However the birefringence effect of the (011)-oriented aluminum perovskite crystals is non-negligible when sub-micrometer spatial resolution is required. Consequently, further investigations are required to optimize the LPE process on the (100)-oriented YAP substrates and increase the light yield up to the value obtained for the (011)-oriented ones.

Chapter 6

Single crystal lutetium oxide scintillating films

The first results about the development of Eu-doped lutetium oxide (Lu_2O_3) single crystal films are reported in this chapter.

6.1 Introduction

In the last twenty years, Lu_2O_3 has been studied extensively since it showed promising properties as a laser material and as a scintillator for radiation detection. Over the years the development has focused on many different crystalline forms, e.g. transparent ceramic (92), bulk single crystal (36, 37, 93), polycrystalline thin film (94), micro-structured material (95) and micro- and nano-particles (96, 97).
Lutetium oxide is a good candidate for high-resolution imaging for three main reasons. Firstly, the remarkable high density (9.5 g/cm^3) and high effective Z number of Lu_2O_3 lead to a high absorption efficiency. In table 6.1 the calculated energy deposited (see chapter 2 for the calculation details) in a 5 μm thick film of Lu_2O_3 is reported and compared to GGG, LSO, GdLuAP and LuAG films. In terms of absorption efficiency, the lutetium oxide film outperforms the other considered materials. For example at 64 keV, the energy deposited is 1.6 times that of LSO and 2.4 times that of LuAG.
Secondly, Lu_2O_3 accepts many activators, and is thus a versatile host for efficient phosphors. Eu-doped Lu_2O_3 has been proposed as an excellent scintillator for the first time by Dujardin et al (30) in powder form, exhibiting a scintillation yield up to 60 % of the well-known $Gd_2O_2S : Tb^{3+}$. Transparent ceramic Lu_2O_3:Eu scintillators were reported by Shi et al.(98) to show 10 times the light yield of single crystal BGO scintillators,

Table 6.1: Total energy deposited (E_{dep}) in 5 μm thick scintillators calculated for different X-ray energies using the Monte Carlo simulations described in chapter 2.

	GGG on GGG	LSO on YbSO	GdAP on YAP	GdLuAP on YAP	LuAG on YAG	Lu_2O_3 on Lu_2O_3
E_{dep} at 15keV	21.11 %	27.85 %	20.13 %	24.73 %	21.02 %	38.15%
E_{dep} at 52keV	1.28 %	0.94 %	1.40 %	1.38 %	0.76 %	1.47%
E_{dep} at 64keV	0.87 %	1.14 %	1.02 %	1.09 %	0.75 %	1.83%

which have a conversion efficiency of approximately 9-10 ph/keV, while Seeley at al.(92) reported an efficiency 3 times higher than commercially available scintillating glasses (IQI-301). Garcia-Murillo et al. (99) reported a light yield of 22 photons/keV for Lu_2O_3:Eu sol-gel polycristalline films. All these results show that Lu_2O_3:Eu can surely compete in terms of light yield with many currently commercially available scintillators. However, not many results are available for the single crystal Lu_2O_3:Eu scintillators. Recently, Veber et al. (37) reported a light yield for $Lu_{1.56}Gd_{0.41}O_3$: Eu single crystals up to 2 times higher than that of YAG:Ce.
The last reason for being a good candidate for high resolution imaging is found in the cubic crystal structure of Lu_2O_3 and its optically isotropic properties. Therefore, the resolution is not expected to be degraded due to the birefringence (see section for a detailed explanation).

6.2 Lutetium oxide liquid phase epitaxy growth

For the LPE growth of lutetium oxide SCFs a bulk SC with the same structure and a lattice parameters close to the ones of the film are required. Many sesquioxide materials as Lu_2O_3, Y_2O_3 or Gd_2O_3 are difficult to growth as bulk single crystals due to their high melting point, which is above 2400 ℃. However, much progress has been observed recently. Promising results have been obtained using techniques which lower the growth temperature using solvents as for example the hydrothermal or the flux methods (37, 93). Up to now, however, the production of optically good crystals with a volume of a few cubic centimeters has only been reported using a modified version of the Bridgman technique, the so-called heat exchanger method (HEM) (37), which is still in a development stage.
In this work the Lu_2O_3 films were grown on SC Lu_2O_3 substrates produced by FEE GmbH using the HEM technique. Due to the development state of the bulk growth, the substrates were not oriented along a preferential direction and in some of them

the presence of grains with a different orientation than the rest of the substrate was observed through X-ray Laue diffraction.
The solvent used for the growth of the film was composed of PbO and B_2O_3 5N pure powders with an atomic ratio Pb/B 5.1-5.5. Lu_2O_3 and Eu_2O_3 5N pure powders were dissolved in the solvent. The experimental details are the same as described in chapter 4.
So far two different melt compositions, here called A and B, were studied, and approximately 40 Lu_2O_3 films with thicknesses in the range 0.5-22 μm were grown. The parameters for the growth are reported in table 6.2. As comparison, the parameters for the optimized growth of GdLuAP SCFs on YAP substrates are also reported.

Table 6.2: Growth parameters studied for the liquid phase epitaxy development of Lu_2O_3 thin films on Lu_2O_3: R_{Eu}^{melt} =(Eu)/(Eu+Lu) and R_s^{melt} =(Eu+Lu)/(Lu + Eu + Pb + Eu), range of growth temperature (T), thickness (Th.), growth rate (G.R.) and average light yield (L.Y.) compared to the LY of a bulk YAG:Ce S.C.. As reference, R_s^{melt}, T and G.R. are also reported for the optimized melt composition for the GdLuAP film growth.

melt	R_s^{melt} [%]	R_{Eu}^{melt} [%]	T [°C]	G.R. [$\frac{\mu m}{min}$]	Th.[μm]	L.Y.
A	4.2 ± 0.3	0-5.6	1075 ± 35	1.3-3.5	9-22	5%
B	3.2 ± 0.3	2.1-22.3	985 ± 25	0.1-0.8	0.5-20	15-20%
GdLuAP	5.1 ± 0.2		1030 ± 20	0.1-0.6		

Both the compositions A and B lead to a stable melt and to the formation of a film with homogeneous thickness, good optical quality and homogeneous surface. A SEM image of the surface of a Lu_2O_3 film and the cross sectional image of that film are shown in figure 6.1. The thicknesses measured from cross sectional SEM images agree with the values calculated from the weight gain.
The solute/solvent ratio in the first melt (A) was varied around the value R_s^{melt} =4.2. Good quality films were obtained, but a growth rate below 1 μm/min was not obtained, because the saturation temperature was approximately 1250 ℃, higher than the maximum working conditions of the LPE furnace (maximum temperature of growth ≈1100℃). Low light yields, about 5% of that obtained using the reference YAG:Ce SC were obtained. The europium concentration in the melt R_{Eu}^{melt} was gradually increased up 5.6%; no variation of the L.Y. in this range was obtained. In the second melt (B) the R_s^{melt} ratio was reduced to study lower growth rates. Compared to the YAG:Ce reference the maximum obtained light yield was 20%. For R_{Eu}^{melt} in the range 3.5-22.3%, no dependence of the L.Y. on R_{Eu}^{melt} was observed.

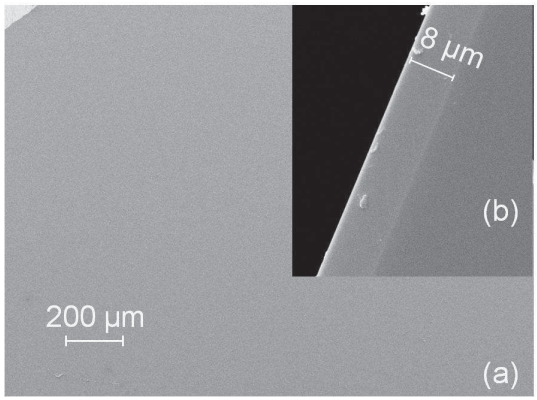

Figure 6.1: SEM images of a Lu_2O_3:Eu film on a Lu_2O_3 substrate. (a) Top-view of the film surface (b) Cross section of the film. The film's thickness is indicated.

Table 6.3: Atomic ratios of the impurity contents (Eu, Pb, Pt and Zr) in three different Lu_2O_3 thin films, grown from melt B. As reference, the intervals of variation of the same ratios are shown for the measured GdLuAP films. The different ratios are defined as $R_X^{film} = \frac{X}{(Gd)+Lu+Eu+Zr+Pt+Pb}$. The concentration of Eu in the melt $R_{Eu}^{melt} = \frac{Eu}{(Gd)+Lu+Eu}$ and the ratio $R_{Eu}^{melt}/R_{Eu}^{film}$ are also reported.

	Lu_2O_3 : Eu sample nb.1	Lu_2O_3 : Eu sample nb.2	Lu_2O_3 : Eu sample nb.3	GdLuAP:Eu (average)
R_{Pb}^{film}	0.46 %	0.21 %	0.33 %	0.01-0.04 %
R_{Pt}^{film}	0.03 %	n.d.	0.04 %	0.04-0.5 %
R_{Zr}^{film}	0.37 %	0.65 %	1.09 %	not detected
R_{Eu}^{film}	1.39 %	2.26 %	3.37 %	1.17-1.88 %
R_{Eu}^{melt}	10.14 %	20.28 %	22.3 %	1.33-1.73 %
$R_{Eu}^{melt}/R_{Eu}^{film}$	0.14	0.11	0.15	0.88-1.08

To keep the supersaturation temperature range below the furnace limit of 1100 °C, it was needed to lower percentage of solute dissolved in the PbO-B_2O_3 solvent (as compared, for example, to the GdLuAP film growth). As a consequence, the platinum crucible became strongly corroded by the lead based solvent and contaminated the melt. The light yield obtained for Lu_2O_3 : Eu was unexpectedly low, despite the good light yield reported for this material. Hence, to understand the possible origin of the low light yield, the amount of unwanted impurities in the films, as well as the amount of Eu dopant, were investigated using XRF.

The results are reported in table 6.3 for three different samples, which are compared to the values obtained for GdLuAP. Several remarks about these data should be made.

Firstly, the lead content is approximately one order of magnitude higher than in the perovskite films.

Secondly, the platinum content is comparable with the (011)-oriented GdLuAP SCF, which shows the lowest Pt content of all studied orientations and the highest light yield.
Thirdly, the europium segregation in the Lu_2O_3 films is only 0.11-0.15, while it is approximately 1 for the GdLuAP SCFs. The Eu content in the film increases linearly with the Eu content in the melt. The maximum value of R_{Eu}^{film} was found to be 3.4%, for $R_{Eu}^{melt} = 22.3\%$. The supersaturation temperature range of the melt was observed to reduce for increasing R_{Eu}^{melt}. This meant that Lu_2O_3 films could not be grown for R_{Eu}^{melt} above 22.3%. However, no significant variations of the light yield were observed while the europium in the melt was increased. Therefore, the low europium segregation in the film is probably not responsible for the low light yield.
Lastly, the most surprising result is the high contents of zirconium measured in the film. The Zr contents originates from the Pt crucible in which it is used as a reinforcement and the concentration in the crucible is approximately 200 ppm. The ratio R_{Zr}^{film} increases with the Eu contents. This can be explained since the samples with higher Eu contents are produced later and therefore more of the crucible content is incorporated in the melt. The Zr contents can not be compared with the GdLuAP SCFs since they were grown using a Y-reinforced crucible (Zr-free), which is not produced anymore.
The lead and zirconium contaminations may be responsible for the low light yield of the lutetium oxide films. A different solvent, with a lower lead component, needs to be studied to clarify this point.
XRD measurements were performed to confirm the growth of Lu_2O_3 single crystal films with cubic phase. The experiment was performed at 15 keV on the reflectometer on the ESRF beamline BM05 (see "experimental" in chapter 4). The XRD pattern is reported in figure 6.2 for a 3.5 μm thick (111)-oriented Lu_2O_3 : Eu SCF, grown from melt B. The europium ratio R_{Eu}^{melt} was 10%, corresponding to approximately 1% in the film.
Omega-2theta scans were performed around the (222), (444) and (666) symmetric Bragg reflections (figure 6.2 a,b,c). The substrate peak is located at higher angles than the film peak. For the (222)-Bragg reflection, the substrate peak is not completely separated from the film peak due to the lower angle separation and to the higher absorption in the film at low angles. The mismatch between the film and substrate lattice parameters $\Delta\ell = (\ell^{film} - \ell^{substrate})/(\ell^{substrate})$ was found to be 0.04 %. The complete omega-2theta diffraction pattern is reported in figure 6.2d. Additional peaks were not observed.
The rocking curves around the (444) Bragg reflections of the film and of the substrate are reported in figure 6.3. To compare the FWHM, the two curves are normalized and shifted to zero. Similar rocking curves are obtained for the film and the substrate, which

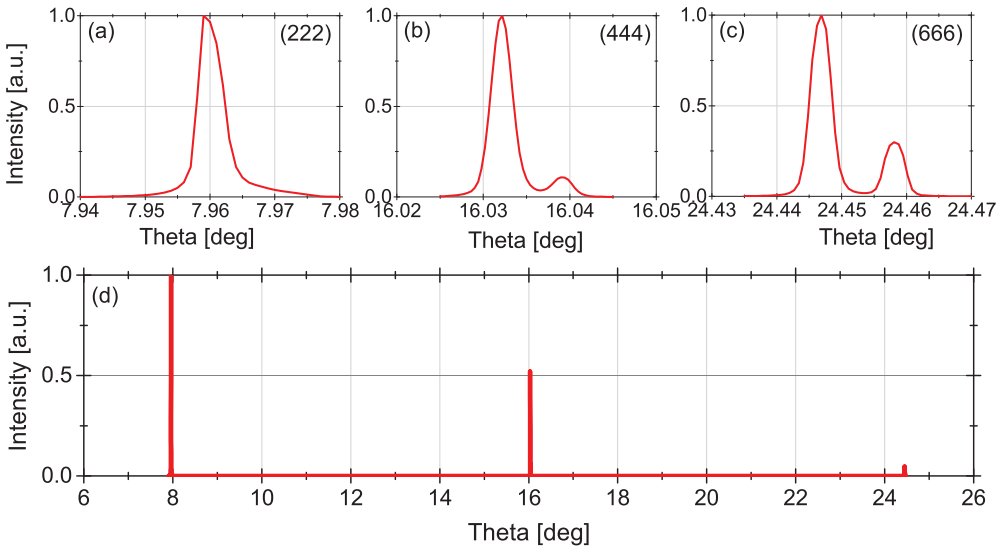

Figure 6.2: Omega-2Theta scans for a (111)-oriented 3 μm thick Lu_2O_3 film on a Lu_2O_3 substrate. The scan was recorded at 15 keV around the (a) (222) (b) (444) and (c) (666) bragg reflection. The film-substrate mismatch measured from (b) and (c) is 0.04%. In (a) the substrate peak is not visible due to the complete X-ray absorption in the film. In (d) the full Omega-2Theta scan from the (222) to the (666) Bragg reflection is reported.

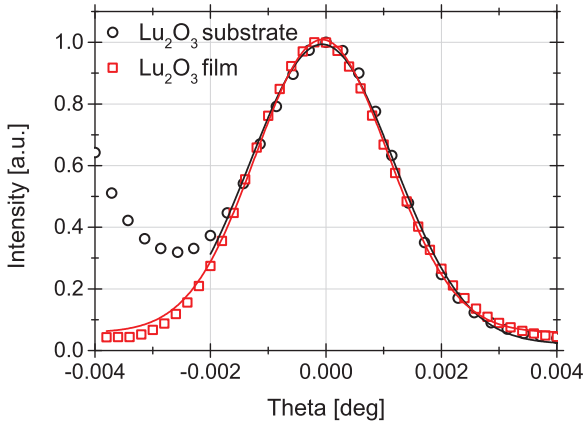

Figure 6.3: Rocking curves around the (444) Bragg reflection for 3 μm thick Lu_2O_3 film on a Lu_2O_3 substrate. The film and the substrate are (111)-oriented. The curves were recorded at 15 keV and they are shifted at 0° for comparison: the FWHM of the substrate is 0.0027° and the one of the film is 0.0029°.

indicates a similar crystallinity.

6.3 X-ray imaging using lutetium oxide SCFs

The Lu_2O_3 : Eu emission spectra under X-ray irradiation at 8 keV is reported in figure 6.4. The emission spectra, typical of the Lu_2O_3 : Eu cubic-phase, confirming the XRD results. Several peaks between 575 and 725 nm were observed, corresponding to the $^5D_0 \rightarrow ^7 F_j$ (j=0,1,2,3,4) transitions. The strongest emission, located at 611 nm, corresponds to the $^5D_0 \rightarrow ^7 F_2$ transition.

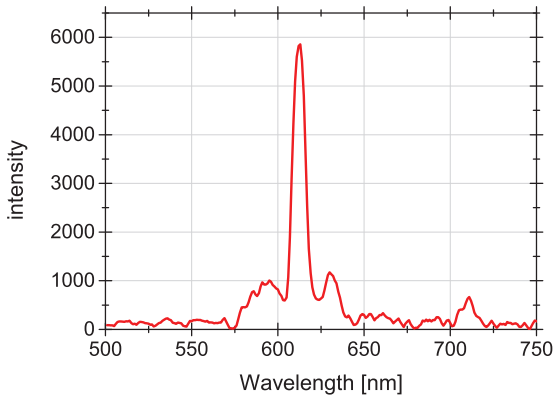

Figure 6.4: Emission spectra of a Lu_2O_3 : Eu SCF scintillator under X-ray irradiation at 8 keV.

So far the maximum light yield that we obtained for Lu_2O_3 : Eu SCFs is 20% of the YAG:Ce bulk SC used as reference. Typical values for GGG:Eu and LSO:Tb scintillators, as well as for the newly developed GdLuAP:Eu SCFs, are in the range 70-100%.

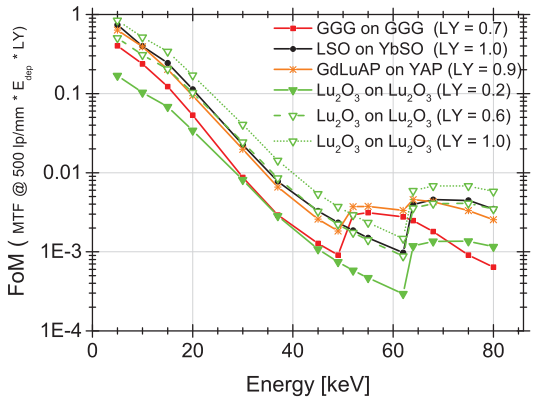

Figure 6.5: Figure of merit including the total efficiency (Deposited energy × LY) and the scintillator response (contrast at 500 lp/mm), calculated as in equation 2.2 for 5 μm thick GGG, LSO and GdLuAP scintillators.

Figure 6.5 compares the figure of merit (absorption × light yield × MTF at 500 lp/mm), calculated using the simulation results from chapter 2, for Lu_2O_3 : Eu films as compared to GGG:Eu, LSO:Tb and GdLuAP:Eu SCFs.
Although the absorption of Lu_2O_3 is higher, its efficiency is reduced because of the low

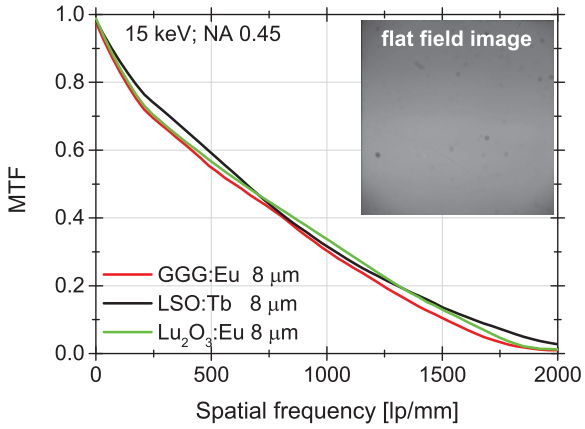

Figure 6.6: MTF curves recorded at 15 keV using the slanted edge method. 8 μm thick LSO:Tb, GGG:Eu and Lu_2O_3:Eu films were combined in the high resolution detector with 20X/0.45 microscope optics, 3.3X eyepiece and PCO2000 camera.

light yield of the grown films. To compete with LSO:Tb SCFs, a light yield of 60% compared to YAG:Ce SC is required. For a light yield higher than 60%, Lu_2O_3 would outperform the other SCFs, except in the 51-64 keV range, where the Gd-based materials are still more performant even if a LY equal to the one of LSO:Tb is obtained. For example, if the LY for Lu_2O_3 scintillator is equal to the one of LSO:Tb (LY=1), the FoM is 1.5 times higher at 68 keV.

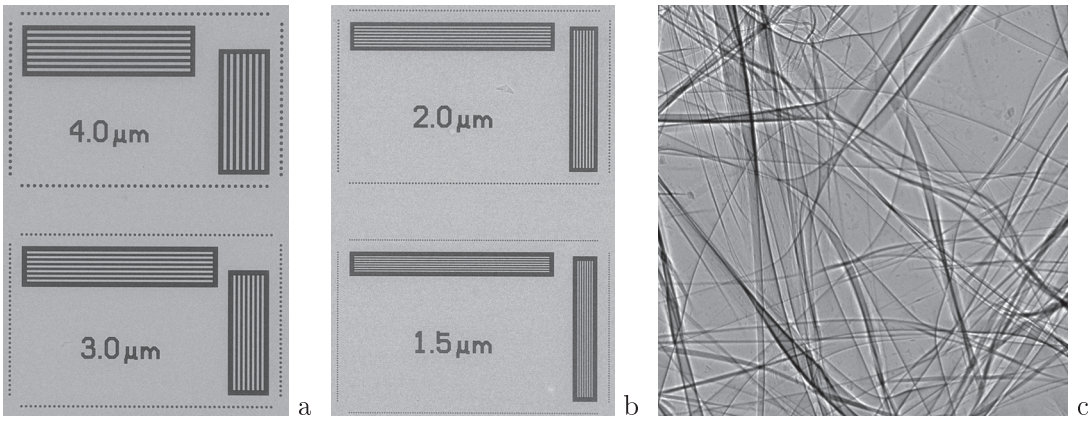

Figure 6.7: Radiography images of a (a,b) JIMA resolution chart, for several detail sizes and of (c) a plastic foam, obtained with 8 μm thick Lu_2O_3:Eu SCF combined with 20X/0.45 microscope optics, 3.3X eyepiece and PCO2000 camera.

The image quality obtained using the new Lu_2O_3 : Eu SCFs for high resolution detectors was also tested. In figure 6.6, the MTF is calculated from the image of a sharp edge, using different SCFs combined with 20X/0.45 microscope optics, 3.3X eyepiece

and PCO2000 camera. The results obtained with GGG:Eu, LSO:Tb and Lu_2O_3:Eu are comparable. In the inset, the flat field image for the Lu_2O_3:Eu is reported. It is shown that the light emission from the Lu_2O_3:Eu film does not show inhomogeneities which may reduce the light yield.
Some radiographies of the JIMA resolution chart and a styrofoam obtained using the Lu_2O_3:Eu SCFs are shown in figure 6.7. The details can be clearly identified and distortions are not observed in the images, confirming the good optical quality of the films.

6.4 Conclusions

Lu_2O_3:Eu SCFs with high optical quality were successfully grown on Lu_2O_3 SC substrates. The quality of the images obtained using these new SCFs are already comparable to the existing LSO and GGG SCFs, but the Lu_2O_3:Eu SCFs are less efficient due to the low light yield, even if their absorption is higher.
The low light yield requires further investigations, but it is probably linked to the high contents of lead and zirconium in the film. The first is coming from the solvent, the latter from the Pt crucible. The low solute concentration which is needed to keep the growth temperature below 1100°C results in a melt which strongly corrodes the platinum crucible and sample holder and contaminates the films.
In our case, the next steps are the investigation of different solvent compositions with a reduced percentage of lead and the test of different Pt crucibles, possibly Zr-free. Additionally, the scintillation properties of the Lu_2O_3 SCFs, activated using different dopants and co-dopants, should be investigated.

Chapter 7

Conclusions

7.1 Modelling of the high-resolution detector

Indirect detectors are today often preferred for absorption and phase contrast imaging experiments at synchrotrons. Some of the main advantages over direct semiconductor detectors are the possibility of managing high X-ray fluxes, the lower price and the resistance to radiation damage. Indirect detectors using thin SCF scintillators and microscope optics are capable of sub-micrometer spatial resolution. Additionally, the detector's resolution and field of view can be adapted to suit the demands of the experiment. The thickness of the scintillator and its composition play a crucial role in the delicate compromise between spatial resolution and efficiency of the detector, especially at high X-ray energy.

In the first part of this work a model to simulate the MTF of high-spatial resolution detectors was presented. Using Monte Carlo simulations, the contribution of the scintillator to the MTF of the detector was evaluated from the distribution of the energy deposited in the scintillator. To take the microscope optics into account, the distribution of the deposited energy was corrected for the light diffraction and for the defocus, as a function of the distance between the focal and any other parallel plane in the scintillator. The total MTF response of the detector was evaluated as the sum of superimposing images produced from the different planes in the scintillator.

The model was experimentally validated. It showed good capability to predict both the detector's MTF and the amount of energy deposited in the film, as a function of the scintillator material, the microscope optics and the X-ray energy.

Different compositions of scintillating film and substrate were simulated for energies ranging from 5 to 80 keV. The MTF response was found to depend mainly on the K-

edge fluorescence of the film and the substrate. The MTF values decrease with the X-ray energy, but a significant improvement was observed above the K-edge of the film, due to the higher cross-section of the photoelectric effect and due to the lower energy of the photoelectrons. Therefore, Gd-based films outperform Lu-based films for energies ranging from 51 to 64 keV, while the Lu-based films are more performant between 64 and 80 keV. On the contrary, the K-edge of the substrate degrades the MTF since the created fluorescence X-rays interact with the film and reduce the contrast at low spatial frequencies. Compared to scintillators on a Y-based substrate, the ones on a Gd or Lu-based substrate are more performant in the 17 to 50 keV range and less performant in the range from 50 to 80 keV.
Without taking the scintillator response into account, the best scintillator thickness equals the depth of field. The model introduced in this work does take the scintillator response into account and allows one to find the detector configuration needed to obtain the best MTF and higher absorption efficiency. In fact the model shows that a thicker scintillator can outperform a thinner one, if the energy distribution is sharper. Of course, it depends on the balance between defocus and scintillator response and, therefore, on the numerical aperture of the optics, the composition of the scintillator and the X-ray energy.
Based on the results of the simulations, lutetium oxide (Lu_2O_3) and gadolinium or lutetium based aluminum perovskites (GdAP, GdLuAP) have been selected as candidate materials for the liquid phase epitaxy based development of thin SCF scintillators.

7.1.1 Perspectives

The Geant4 developed application can be now used both to chose the detector configuration and to guide the development of new scintillators. However, to run a simulation the user should have a basic knowledge of Matlab and C++ programming languages. If an user-friendly interface is created, the application could be released to the beamlines to help in the choice of the detector configuration.
Moreover, Geant4 includes the possibility to simulate the scintillation and track the optical photons. A few preliminary test have been performed, the results are not included in this work. By additionally tracking the optical photons, more configurations could be evaluated. For example, the MTF degradation and the light collection improvement could be evaluated for optical coatings at the surfaces of the scintillator or for modified geometries (curved substrate, structured scintillators).

7.2 Gadolinium and lutetium aluminum perovskite SCF scintillators

GdAP and GdLuAP SCF scintillators were grown on YAP SC substrates. The optical quality of the films needed for high-resolution imaging was obtained after optimizing the GdLuAP film composition to reduce the lattice mismatch with the substrate.
The Eu-doped GdLuAP films show a scintillation LY which is higher than the state-of-the-art GGG scintillators. The LY, however, depends on the substrate orientation, probably due to the a different amount of platinum impurities incorporated in the film. X-ray images obtained using the newly developed films show a slightly better contrast at low energy (15 keV). It was observed that the image quality is also affected by the crystallographic orientation. This became apparent due to the birefringence of the perovskite crystals, since this phenomenon degrades the resolution in the sub-micrometer range. The orientation presenting the highest LY is also strongly affected by the birefringence.

7.2.1 Perspectives

GdLuAP:Eu SCFs can compete with the state-of-the-art SCFs as scintillators for high-spatial resolution detectors. However, more investigations are required to clarify the role of the substrate orientation on the light yield. The growth process needs to be modified to improve the LY of the films grown on the orientations least affected by the birefringence.
Moreover, the YAP substrates present a luminescence in the UV and visible range that can degrade the resolution at high energies. This luminescence can be only partially suppressed using an optical filter. Therefore, a YAP growth process in collaboration with companies or laboratories that produce bulk SC YAP should be foreseen in order to reduce or suppress the unwanted luminescence.
Finally, the scintillation properties of other dopants than europium in GdLuAP host, as for example cerium or terbium, should be investigated.

7.3 Lutetium oxide SCF scintillators

Undoped and Eu-doped Lu_2O_3 SCFs were grown on SC Lu_2O_3 substrates. Homogeneous films were obtained, showing high crystalline and optical quality. The imaging performance is comparable with the state-of-the-art SCF scintillators. However, the

conversion efficiency is unexpectedly low when compared to Lu_2O_3:Eu scintillators developed using other techniques than LPE. The scintillation in LPE based crystals is probably quenched by lead and zirconium impurities in the film which originate from the solvent and the platinum crucible, respectively. The amount of lead used to keep the growing temperature within the limitation of the furnace was in fact significantly higher than for other materials (e.g. GdLuAP, LSO and GGG), resulting in a melt that corroded the crucible. If the melt composition can be modified to reduce the luminescence quenching, Lu_2O_3 could become a very welcome addition to the SCF scintillator family. Due to its absorption efficiency being higher than most other known scintillators, and due to the high-optical quality that can be obtained through LPE growth, Lu_2O_3 remains one of the best candidates for high-resolution imaging at high X-ray energies.

7.3.1 Perspectives

The reason of the low light yield observed in Lu_2O_3:Eu SCFs should be investigated. On the one hand, the role of the traps could be clarified for example using thermo stimulated luminescence experiments. On the other hand, the solvent used for the LPE should be modified to reduce the corrosion of the crucible and thus the melt contamination. Other kind of Zr-free platinum crucibles have to be tested to clarify the role of the zirconium in the luminescence quenching. Moreover, different dopants, as for example Tb, are known as good activators in the Lu_2O_3 host, and should be investigated in the case of SCFs grown by LPE.

References

[1] Jean-David Moreau, Peter Cloetens, Bernard Gomez, Véronique Daviero-Gomez, Didier Néraudeau, Tamzin A Lafford, and Paul Tafforeau. **Multiscale 3D virtual dissections of 100-million-year-old flowers using X-Ray synchrotron micro-and nanotomography**. *Microscopy and Microanalysis*, **20**(01):305–312, 2014. 12, 13

[2] Thierry Martin and Andreas Koch. **Recent developments in X-ray imaging with micrometer spatial resolution**. *Journal of Synchrotron Radiation*, **13**(2):180–194, 2006. 14, 35, 36

[3] P-A Douissard, Angelica Cecilia, Thierry Martin, Valentin Chevalier, Maurice Couchaud, Tilo Baumbach, Klaus Dupré, Markus Kuehbacher, and Alexander Rack. **A novel epitaxially grown LSO-based thin-film scintillator for micro-imaging using hard synchrotron radiation**. *Journal of synchrotron radiation*, **17**(5):571–583, 2010. 14, 35, 36

[4] Andreas Koch, Carsten Raven, Per Spanne, and Anatoly Snigirev. **X-ray imaging with submicrometer resolution employing transparent luminescent screens**. *JOSA A*, **15**(7):1940–1951, 1998. 14, 22, 69, 70

[5] K Uesugi, M Hoshino, and N Yagi. **Comparison of lens-and fiber-coupled CCD detectors for X-ray computed tomography**. *Journal of synchrotron radiation*, **18**(2):217–223, 2011. 14

[6] R Dinapoli, A Bergamaschi, S Cartier, D Greiffenberg, I Johnson, JH Jungmann, D Mezza, A Mozzanica, B Schmitt, X Shi, et al. **MÖNCH, a small pitch, integrating hybrid pixel detector for X-ray applications**. *Journal of Instrumentation*, **9**(05):C05015, 2014. 15

[7] C Ponchut, JM Rigal, J Clément, E Papillon, A Homs, and S Petitdemange. **MAXIPIX, a fast readout photon-counting X-ray area detector**

for synchrotron applications. *Journal of Instrumentation*, **6**(01):C01069, 2011. 15, 18

[8] Takaki Hatsui and Heinz Graafsma. **X-ray imaging detectors for synchrotron and XFEL sources**. *IUCrJ*, **2**(3):371–383, 2015. 16

[9] Philip Willmott. *An introduction to synchrotron radiation: Techniques and applications*. John Wiley & Sons, 2011. 16

[10] Desy website. **http://science.desy.de/research/studentsteaching/sr_and_fel_basics/fel_basics/tdr_spectral_characteristics/index_eng.html**. 17

[11] Roberto Dinapoli, Anna Bergamaschi, Beat Henrich, Roland Horisberger, Ian Johnson, Aldo Mozzanica, Elmar Schmid, Bernd Schmitt, Akos Schreiber, Xintian Shi, et al. **EIGER: Next generation single photon counting detector for X-ray applications**. *Nuclear Instruments and Methods in Physics Research Section A: Accelerators, Spectrometers, Detectors and Associated Equipment*, **650**(1):79–83, 2011. 18

[12] Marie Ruat and Cyril Ponchut. **Characterization of a X-ray pixellated CdTe detector with TIMEPIX photon-counting readout chip**. In *Nuclear Science Symposium and Medical Imaging Conference (NSS/MIC), 2011 IEEE*, pages 4799–4803. IEEE, 2011. 18

[13] AEF de Jong, V Vonk, M Ruat, M Boćkowski, G Kamler, I Grzegory, V Honkimäki, and E Vlieg. **Preparation of a smooth GaN–Gallium solid–liquid interface**. *Journal of Crystal Growth*, **448**:70–75, 2016. 18

[14] D Pennicard, S Lange, S Smoljanin, H Hirsemann, H Graafsma, M Epple, M Zuvic, MO Lampert, T Fritzsch, and M Rothermund. **The LAMBDA photon-counting pixel detector**. In *Journal of Physics: Conference Series*, **425**, page 062010. IOP Publishing, 2013. 18

[15] P-A Douissard, A Cecilia, X Rochet, X Chapel, T Martin, Th van de Kamp, L Helfen, T Baumbach, L Luquot, X Xiao, et al. **A versatile indirect detector design for hard X-ray microimaging**. *Journal of Instrumentation*, **7**(09):P09016, 2012. 19

[16] Jean-Claude Labiche, Olivier Mathon, Sakura Pascarelli, Mark A Newton, Gemma Guilera Ferre, Caroline Curfs, Gavin Vaughan, Alejandro Homs, and David Fernandez Carreiras. **Invited article: The fast readout low noise camera as a versatile x-ray detector for time resolved dispersive extended x-ray absorption fine structure and diffraction studies of dynamic problems in materials science, chemistry, and catalysis**. *Review of scientific instruments*, **78**(9):091301, 2007. 19, 23

[17] C Nemoz, S Bayat, G Berruyer, T Brochard, P Coan, G Le Duc, J Keyrilainen, S Monfraix, M Renier, H Requardt, et al. **Synchrotron radiation computed tomography station at the ESRF biomedical beamline**. 2007. 19

[18] Gema Martinez-Criado, Julie Villanova, Rémi Tucoulou, Damien Salomon, J-P Suuronen, Sylvain Labouré, Cyril Guilloud, Valentin Valls, Raymond Barrett, Eric Gagliardini, et al. **ID16B: a hard X-ray nanoprobe beamline at the ESRF for nano-analysis**. *Journal of synchrotron radiation*, **23**(1), 2016. 20

[19] Jakoub Szlachetko, M Cotte, J Morse, M Salomé, P Jagodzinski, J-C Dousse, Joanna Hoszowska, Yves Kayser, and J Susini. **Wavelength-dispersive spectrometer for X-ray microfluorescence analysis at the X-ray microscopy beamline ID21 (ESRF)**. *Journal of synchrotron radiation*, **17**(3):400–408, 2010. 20

[20] UW Arndt and DJ Gilmore. **X-ray television area detectors for macromolecular structural studies with synchrotron radiation sources**. *Journal of Applied Crystallography*, **12**(1):1–9, 1979. 21, 22

[21] NM Allinson. **Development of non-intensified charge-coupled device area X-ray detectors**. *Journal of synchrotron radiation*, **1**(1):54–62, 1994. 22

[22] Glenn D Boreman. *Modulation transfer function in optical and electro-optical systems*, **21**. SPIE Press Bellingham, WA, 2001. 24, 27

[23] Yue Min Zhu, Valérie Kaftandjian, Gilles Peix, and Daniel Babot. **Modulation transfer function evaluation of linear solid-state x-ray-sensitive detectors using edge techniques**. *Applied optics*, **34**(22):4937–4943, 1995. 27, 76

[24] Ehsan Samei, Michael J Flynn, and David A Reimann. **A method for measuring the presampled MTF of digital radiographic systems using an edge test device**. *Medical physics*, **25**(1):102–113, 1998. 27, 76

[25] Martin Nikl. **Scintillation detectors for x-rays**. *Measurement Science and Technology*, **17**(4):R37, 2006. 28

[26] P Dorenbos, J Th M de Haas, and CWE Van Eijk. **Non-proportionality in the scintillation response and the energy resolution obtainable with scintillation crystals**. *IEEE Transactions on Nuclear Science*, **42**(6):2190–2202, 1995. 30, 53, 80

[27] Federico Moretti, Gael Patton, Andrei Belsky, Mauro Fasoli, Anna Vedda, Mattia Trevisani, Marco Bettinelli, and Christophe Dujardin. **Radioluminescence sensitization in scintillators and phosphors: trap engineering and modeling**. *The Journal of Physical Chemistry C*, **118**(18):9670–9676, 2014. 30

[28] KA Wickersheim, RV Alves, and RA Buchanan. **Rare earth oxysulfide x-ray phosphors**. *IEEE Transactions on Nuclear Science*, **1**(17):57–60, 1970. 31

[29] E Zych, D Hreniak, and W Strek. **Spectroscopic properties of Lu2O3/Eu3+ nanocrystalline powders and sintered ceramics**. *The Journal of Physical Chemistry B*, **106**(15):3805–3812, 2002. 31

[30] C Dujardin, A Garcia-Murillo, C Pedrini, C Madej, C Goutaudier, A Koch, AG Petrosyan, KL Ovanesyan, GO Shirinyan, and MJ Weber. **Synthesis and scintillation properties of some dense X-ray phosphors**. In *Proceedings of the 5th International Conference on Inorganic Scintillators and Their Applications (SCINT99)*, pages 16–20, 1999. 31, 32, 113

[31] Robert K Swank. **Calculation of modulation transfer functions of X-ray fluorescent screens**. *Applied optics*, **12**(8):1865–1870, 1973. 31

[32] Heinz Graafsma and Thierry Martin. **Detectors for synchrotron tomography**. *Advanced tomographic methods in materials research and engineering*, **66**:277, 2008. 31, 34

[33] W Van Sciver and Robert Hofstadter. **Scintillations in Thallium-Activated Ca I 2 and CsI**. *Physical Review*, **84**(5):1062, 1951. 32

[34] Piotr Szupryczynski, Charles L Melcher, Merry A Spurrier, Michael P Maskarinec, A Andrew Carey, Andrzej J Wojtowicz, Winicjusz Drozdowski, Darek Wisniewski, and Ron Nutt. **Thermoluminescence and scintillation properties of rare earth oxyorthosilicate scintillators**. *IEEE Transactions on Nuclear Science*, **51**(3):1103–1110, 2004. 32

[35] H Ishibashi, K Shimizu, K Susa, and S Kubota. **Cerium doped GSO scintillators and its application to position sensitive detectors**. *IEEE Trans. Nucl. Sci.;(United States)*, **36**(CONF-881103-), 1989. 32

[36] V Peters, A Bolz, K Petermann, and G Huber. **Growth of high-melting sesquioxides by the heat exchanger method**. *Journal of crystal growth*, **237**:879–883, 2002. 32, 113

[37] Philippe Veber, Matias Velazquez, Paul-Antoine Douissard, Thierry Martin, Olivier Plantevin, and Rekia Belhoucif. **Flux growth and physical properties characterizations of Y 1.866 Eu 0.134 O 3 and Lu 1.56 Gd 0.41 Eu 0.03 O 3 single crystals**. *Optical Materials Express*, **6**(1):207–219, 2016. 32, 113, 114

[38] A Cecilia, V Jary, M Nikl, E Mihokova, D Hänschke, E Hamann, P-A Douissard, A Rack, T Martin, B Krause, et al. **Investigation of the luminescence, crystallographic and spatial resolution properties of LSO: Tb scintillating layers used for X-ray imaging applications**. *Radiation Measurements*, **62**:28–34, 2014. 32

[39] Jianren Lu, Ken-ichi Ueda, Hideki Yagi, Takagimi Yanagitani, Yasuhiro Akiyama, and Alexander A Kaminskii. **Neodymium doped yttrium aluminum garnet (Y 3 Al 5 O 12) nanocrystalline ceramicsa new generation of solid state laser and optical materials**. *Journal of alloys and compounds*, **341**(1):220–225, 2002. 33

[40] A Lempicki, C Brecher, P Szupryczynski, H Lingertat, VV Nagarkar, SV Tipnis, and SR Miller. **A new lutetia-based ceramic scintillator for X-ray imaging**. *Nuclear Instruments and Methods in Physics Research Section A: Accelerators, Spectrometers, Detectors and Associated Equipment*, **488**(3):579–590, 2002. 33

[41] Zsolt Marton, Stuart R Miller, Charles Brecher, Peter Kenesei, Matthew D Moore, Russell Woods, Jonathan D Almer, Antonino

Miceli, and Vivek V Nagarkar. **Efficient high-resolution hard x-ray imaging with transparent Lu2O3: Eu scintillator thin films**. In *SPIE Optical Engineering+ Applications*, pages 95940E–95940E. International Society for Optics and Photonics, 2015. 33

[42] JM Ko, K Lebbou, C Dujardin, C Pedrini, SD Durbin, and T Fukuda. **Molecular beam epitaxy of rare-earth trifluoride, RF 3 (R= Ce, Nd, Er, Lu) layers**. *Optical Materials*, **19**(1):139–143, 2002. 35

[43] C Dujardin, C Le Luyer, C Martinet, C Garapon, J Mugnier, AG Murrillo, C Pedrini, and T Martin. **Thin scintillating films of sesquioxides doped with Eu 3+**. *Nuclear Instruments and Methods in Physics Research Section A: Accelerators, Spectrometers, Detectors and Associated Equipment*, **537**(1):237–241, 2005. 35

[44] DENIS PELENC. *Elaboration par epitaxie en phase liquide et caracterisation de couches monocristallines de yag dope: realisation de lasers guide d'onde neodyme et ytterbium a faibles seuils*. PhD thesis, Grenoble 1, 1993. 35, 86, 95

[45] G. Dhanaraj, K. Byrappa, V. Prasad, and M. Dudley. *Springer Handbook of Crystal Growth*. Springer Handbook of Crystal Growth. Springer Berlin Heidelberg, 2010. 35, 86

[46] M Nikl, J Tous, JA Mares, P Prusa, E Mihokova, K Blazek, A Vedda, Yu Zorenko, V Gorbenko, and V Babin. **Lu3Al5O12-based materials for high 2D-resolution scintillation detectors**. In *SPIE Defense, Security, and Sensing*, pages 731008–731008. International Society for Optics and Photonics, 2009. 35

[47] M Nikl, A Vedda, M Fasoli, I Fontana, VV Laguta, E Mihokova, J Pejchal, J Rosa, and K Nejezchleb. **Shallow traps and radiative recombination processes in Lu 3 Al 5 O 12: Ce single crystal scintillator**. *Physical Review B*, **76**(19):195121, 2007. 36

[48] Yu V Zorenko and VI Gorbenko. **Growth and luminescence properties of single-crystalline films of RAlO3 (R= Lu, Lu-Y, Y, Tb) perovskite**. *Phys. Solid State*, **51**(9):1800–1808, 2009. 36, 85

[49] M Kučera, K Nitsch, M Nikl, M Hanuš, and S Daniš. **Growth and characterization of YAG and LuAG epitaxial films for scintillation applications**. *J. Cryst. Growth*, **312**(9):1538–1545, 2010. 36

[50] Jan Tous, Karel Blazek, Miroslav Kucera, Martin Nikl, and Jiri A Mares. **Scintillation efficiency and X-ray imaging with the RE-Doped LuAG thin films grown by liquid phase epitaxy**. *Radiat. Meas.*, **47**(4):311–314, 2012. 36

[51] Yu Zorenko, JA Mares, P Prusa, M Nikl, V Gorbenko, V Savchyn, R Kucerkova, and K Nejezchleb. **Luminescence and scintillation characteristics of YAG: Ce single crystalline films and single crystals**. *Radiat. Meas.*, **45**(3):389–391, 2010. 36

[52] Yuriy Zorenko, Vitaliy Gorbenko, Taras Voznyak, Thierry Martin, Paul-Antoine Douissard, Jiri A Mares, and Martin Nikl. **LuAG: Pr, LuAG: La, and LuAP: Ce thin film scintillators for visualisation of x-ray images**. In *SPIE Defense, Security, and Sensing*, pages 731007–731007. International Society for Optics and Photonics, 2009. 37

[53] F Riva, P-A Douissard, T Martin, F Carlà, Y Zorenko, and C Dujardin. **Epitaxial growth of gadolinium and lutetium-based aluminum perovskite thin films for X-ray micro-imaging applications**. *CrystEngComm*, **18**(4):608–615, 2016. 37

[54] Claude Elwood Shannon. **Communication in the presence of noise**. *Proceedings of the IRE*, **37**(1):10–21, 1949. 40

[55] Harry Nyquist. **Certain topics in telegraph transmission theory**. 1928. 40

[56] Sea Agostinelli, John Allison, K al Amako, J Apostolakis, H Araujo, P Arce, M Asai, D Axen, S Banerjee, G Barrand, et al. **Geant4a simulation toolkit**. *Nuclear instruments and methods in physics research section A: Accelerators, Spectrometers, Detectors and Associated Equipment*, **506**(3):250–303, 2003. 40, 42

[57] HH Hopkins. **The frequency response of a defocused optical system**. In *Proceedings of the Royal Society of London A: Mathematical, Physical and Engineering Sciences*, **231**, pages 91–103. The Royal Society, 1955. 41, 69

[58] Geant4 website. **https://geant4.web.cern.ch/geant4/**. 42

[59] John Apostolakis, S Giani, M Maire, P Nieminen, MG Pia, and L Urban. **Geant4 low energy electromagnetic models for electrons and photons**. *Istituto Nazionale Di Fisica Nucleare Technical Report*, 1999. 43

[60] Nagoya City Hall. **Recent improvements in Geant4 electromagnetic physics models and interfaces**. 2011. 43

[61] AG Petrosyan, GO Shirinyan, KL Ovanesyan, C Pedrini, and C Dujardin. **Bridgman single crystal growth of Ce-doped (Lu 1- x Y x) AlO 3**. *Journal of crystal growth*, **198**:492–496, 1999. 44

[62] P Dorenbos, E Bougrine, JTM De Haas, CWE Van Eijk, and MV Korzhik. **Scintillation properties of GdAlO3: Ce crystals**. *Radiation effects and defects in solids*, **135**(1-4):321–323, 1995. 44

[63] Thomas Kimble, Mitch Chou, and Bruce HT Chai. **Scintillation properties of LYSO crystals**. In *Nuclear Science Symposium Conference Record, 2002 IEEE*, **3**, pages 1434–1437. IEEE, 2002. 44

[64] Xianming Zhou, Jun Li, Williams J Nellis, Xiang Wang, Jiabo Li, Hongliang He, and Qiang Wu. **Pressure-dependent Hugoniot elastic limit of Gd3Ga5O12 single crystals**. *Journal of Applied Physics*, **109**(8):083536, 2011. 44

[65] E Zych, D Hreniak, and W Strek. **Lu2O3: Eu, a new X-ray phosphor**. *Mater. Sci*, **20**(111122):9, 2002. 44

[66] Ji-Guang Li and Yoshio Sakka. **Recent progress in advanced optical materials based on gadolinium aluminate garnet (Gd3Al5O12)**. *Science and Technology of Advanced Materials*, 2016. 44

[67] VV Nagarkar, TK Gupta, SR Miller, Y Klugerman, MR Squillante, and G Entine. **Structured CsI (Tl) scintillators for X-ray imaging applications**. *IEEE transactions on nuclear science*, **45**(3):492–496, 1998. 44

[68] Nist database website. **http://www.nist.gov/pml/data/xcom/index.cfm**. 50, 81

[69] CSDA database. **http://srdata.nist.gov/gateway/gateway?property=CSDA+range**. 56

[70] Nikon microscopy website. **http://www.microscopyu.com/microscopy-basics/modulation-transfer-function**. 67, 68

[71] Mortimer Abramowitz, Kenneth R Spring, H Ernst Keller, and Michael W Davidson. **Basic principles of microscope objectives**. *Biotechniques*, **33**(4):772–781, 2002. 68

[72] C.J. Shilpa, A Kadgathur Jayaram, N. Dhananjaya, H. Nagabhushana, S.C. Prashantha, D.V. Sunitha, S.C. Sharma, C. Shivakumara, and B.M. Nagabhushana. **GdAlO3:Eu3+:Bi3+ nanophosphor: Synthesis and enhancement of red emission for WLEDs**. *Spectroc. Acta A*, **133**:550â558, 2014. 85

[73] Jin Young Park, Hong Chae Jung, G. Seeta Rama Raju, Byung Kee Moon, Jung Hyun Jeong, Se-Mo Son, and Jung Hwan Kim. **Enhanced green emission from Tb3+âBi3+ co-doped GdAlO3 nanophosphors**. *Mater. Res. Bull.*, **45**(5):572 – 575, 2010. 85

[74] P-A Douissard, Thierry Martin, Federica Riva, Eric Mathieu, Yuriy Zorenko, Volodymyr Savchyn, Tanya Zorenko, and Alexander Fedorov. **Scintillating Screens for Micro-Imaging Based on the Ce-Tb Doped LuAP Single Crystal Films**. *IEEE Trans. Nucl. Sci.*, **61**(1):433–438, 2014. 85

[75] JP Andreeta and BR Jovanic. **Growth and optical properties of Cr3+ doped GdAlO3 single crystals**. *Materials Research*, **3**(2):45–49, 2000. 85

[76] R Mazelsky, WE Kramer, and RH Hopkins. **Crystal growth of GdAlO 3**. *J. Cryst. Growth*, **2**(4):209–214, 1968. 85

[77] Jiri A Mareš, Martin Nikl, Petr Malỳ, Karel Bartoš, Karel Nejezchleb, Karel Blazek, F De Notaristefani, C D'Ambrosio, D Puertolas, and E Rosso. **Growth and properties of Ce 3+-doped Lu x (RE 3+) 1- x AP scintillators**. *Opt. Mater.*, **19**(1):117–122, 2002. 85

[78] J Chval, D Clement, J Giba, J Hybler, J-F Loude, JA Mares, E Mihokova, Christian Morel, K Nejezchleb, and M Nikl. **Development of new mixed Lu x (RE 3+) 1- x AP: Ce scintillators (RE 3+= Y 3+ or Gd 3+): comparison with other Ce-doped or intrinsic scintillating crystals**. *Nucl. Instr. Meth. Phys. Res. Section A*, **443**(2):331–341, 2000. 85

[79] Miroslav Kučera, Karel Nitsch, Martin Nikl, and Martin Hanuš. **Defects in Ce-doped LuAG and YAG scintillation layers grown by liquid phase epitaxy**. *Radiat. Meas.*, **45**(3):449–452, 2010. 85

[80] GB Stringfellow. **The importance of lattice mismatch in the growth of GaxIn1- xP epitaxial crystals**. *Journal of Applied Physics*, **43**(8):3455–3460, 1972. 85

[81] JM Robertson, MW Van Tol, and JPH Heynen. **Thin single crystalline phosphor layers grown by liquid phase epitaxy**. *Philips J. Res*, **35**(6):354–371, 1980. 86

[82] O Balmes, R van Rijn, D Wermeille, A Resta, L Petit, H Isern, T Dufrane, and R Felici. **The ID03 surface diffraction beamline for in-situ and real-time X-ray investigations of catalytic reactions at surfaces**. *Catal. Today*, **145**(3-4):220–226, 2009. 90

[83] S Roobol, W Underwater, J Drnec, R Felici, and J. Frenken. **BINoculars: data reduction and analysis software for two-dimensional detectors in surface X-ray diffraction**. *J. Appl. Crystallogr.*, **48**(3-4):1324â1329, 2015. 90

[84] NL Ross, J Zhao, and RJ Angel. **High-pressure structural behavior of GdAlO 3 and GdFeO 3 perovskites**. *J. Solid State Chem.*, **177**(10):3768–3775, 2004. 90, 91

[85] L Vasylechko, A Senyshyn, and DM Trots. **Anomalous low-temperature structural properties of orthorhombic REAlO3 perovskites**. *Hasylab Annual Report*, 2007. 90, 91

[86] NL Ross, J Zhao, and RJ Angel. **High-pressure single-crystal X-ray diffraction study of YAlO 3 perovskite**. *J. Solid State Chem.*, **177**(4):1276–1284, 2004. 90, 91

[87] Robert E Newnham. *Properties of materials: anisotropy, symmetry, structure*. Oxford University Press on Demand, 2005. 105

[88] Johannes August Lohne. **Nova Experimenta Crystalli Islandici Disdiaclastici1**. *Centaurus*, **21**(2):106–148, 1977. 105

[89] Nikon microscopy Birifringence. **@onlineDoFweb, author = Nikon microscopy website, title = http://www.microscopyu.com/tutorials/java/polarized/calcite/** . 106

[90] Marvin J Weber. *Handbook of optical materials*, **19**. CRC press, 2002. 107

[91] KW Martin and LG DeShazer. **Indices of Refraction of the Biaxial Crystal YAIO 3**. *Applied optics*, **12**(5):941–943, 1973. 107, 110

[92] ZM Seeley, JD Kuntz, NJ Cherepy, and SA Payne. **Transparent Lu 2 O 3: Eu ceramics by sinter and HIP optimization**. *Optical Materials*, **33**(11):1721–1726, 2011. 113, 114

[93] Colin McMillen, Daniel Thompson, Terry Tritt, and Joseph Kolis. **Hydrothermal single-crystal growth of Lu2O3 and lanthanide-doped Lu2O3**. *Crystal Growth & Design*, **11**(10):4386–4391, 2011. 113, 114

[94] Angel de Jesus Morales Ramírez, Margarita García Hernández, Antonieta García Murillo, Felipe de Jesús Carrillo Romo, Joel Moreno Palmerin, Dulce Yolotzin Medina Velazquez, and María Luz Carrera Jota. **Structural and Luminescence Properties of Lu2O3: Eu3+ F127 Tri-Block Copolymer Modified Thin Films Prepared by Sol-Gel Method**. *Materials*, **6**(3):713–725, 2013. 113

[95] Zsolt Marton, Stuart R Miller, Charles Brecher, Peter Kenesei, Matthew D Moore, Russell Woods, Jonathan D Almer, Antonino Miceli, and Vivek V Nagarkar. **Efficient high-resolution hard x-ray imaging with transparent Lu2O3: Eu scintillator thin films**. In *SPIE Optical Engineering+ Applications*, pages 95940E–95940E. International Society for Optics and Photonics, 2015. 113

[96] Jun Yang, Chunxia Li, Zewei Quan, Cuimiao Zhang, Piaoping Yang, Yinyan Li, Cuicui Yu, and Jun Lin. **Self-assembled 3D flowerlike Lu2O3 and Lu2O3: Ln3+ (Ln= Eu, Tb, Dy, Pr, Sm, Er, Ho, Tm) microarchitectures: ethylene glycol-mediated hydrothermal synthesis and luminescent properties**. *The Journal of Physical Chemistry C*, **112**(33):12777–12785, 2008. 113

[97] Piaoping Yang, Shili Gai, Yanchao Liu, Wenxin Wang, Chunxia Li, and Jun Lin. **Uniform hollow Lu2O3: Ln (Ln= Eu3+, Tb3+) spheres: facile synthesis and luminescent properties**. *Inorganic chemistry*, **50**(6):2182–2190, 2011. 113

[98] Y Shi, QW Chen, and JL Shi. **Processing and scintillation properties of Eu 3+ doped Lu 2 O 3 transparent ceramics**. *Optical Materials*, **31**(5):729–733, 2009. 113

[99] Antonieta Garcia-Murillo, C LeLuyer-Urlacher, C Dujardin, C Pedrini, and J Mugnier. **Rare-earth actived sol-gel films for scintillator applications**. *Journal of sol-gel science and technology*, **26**(1-3):957–960, 2003. 114

Résumé

Introduction

Les détecteurs de rayon-X utilisés pour l'imagerie à haute résolution spatiale (micromètrique ou sub-micromètrique) utilisés aux synchrotrons sont pour la plupart basés sur un système de détection indirect. Les rayons X ne sont pas directement convertis en signal électrique, mais ils sont absorbés par un scintillateur, un matériau qui émet de la lumière à la suite de l'absorption d'un rayonnement ionisant. L'image émise sous forme de lumière visible est ensuite projetée par des optiques de microscopie sur une caméra 2D, de type CCD ou CMOS. Différents types des scintillateurs sont disponibles aujourd'hui: en poudre compactée, micro structuré, sous forme céramique polycristalline et monocristalline. Pour obtenir une résolution spatiale au dessous d'un micromètre avec une très bonne qualité d'image, une couche mince (1-10 μm) monocristalline doit être privilégiée.
Selon la combinaison des différentes parties du détecteur, c'est-à-dire le scintillateur, les lentilles de microscopie et la caméra, la résolution spatiale peut être, au final, limitée par différents phénomènes. Premièrement, l'élargissement de la région dans le scintillateur ou l'énergie du photon X incident est déposée. L'énergie n'est pas localisée dans un seul point, mais se propage due à la diffusion par effet Rayleigh et Compton et à la diffusion des photons X ainsi que des électrons secondaires. Deuxièmement, les lentilles de microscopie agissent comme un trou circulaire vis à vis de la lumière émise. En conséquence, la meilleure image d'un point source qui peut être projetée est limitée par la largeur de la première frange de diffraction. Une telle largeur dépend de la longeur d'onde de la lumière et de l'ouverture numérique des optiques. Troisièmement, les optiques de microscope ont une profondeur de champ, qui correspond à l'épaisseur maximum de la source le long de l'axe optique (i.e. l'épaisseur du scintillateur) peuvent être projetée en focus. La lumière produite en dehors de cette profondeur dégrade la résolution spatiale. Enfin, la taille du pixel de la caméra peut limiter la résolution spa-

tiale. La taille physique du pixel est réduite grâce au grossissement de l'image visible produit par les optiques. Pour un grossissement suffisant et un scintillateur plus mince que la profondeur de champ des optiques, le système est limité soit par la diffraction de la lumière, soit par la diffusion de l'énergie déposée dans le scintillateur.
Pourtant, la profondeur de champ est inférieur à 10 μm pour une ouverture numérique supérieure à 0.3, donc l'efficacité du détecteur est limitée par l'absorption dans la couche, surtout pour des énergies au dessus de 20 keV.
Le travail qui est présenté dans cette thèse est centré sur l'évaluation de la résolution spatiale des détecteurs et sur le développement de nouveaux matériaux monocristallin en couche mince, déposées par épitaxie en phase liquide sur un substrat.

Calcul de la résolution spatiale

La première partie de la thèse décrit le modèle qui a été développé pour pouvoir prédire la résolution spatiale du détecteur selon l'énergie des rayons X, les paramètres du scintillateur (épaisseur, matériau, longueur d'onde d'émission) et l'ouverture numérique des optiques. Ce modèle est basé sur une combinaison de calculs Monte Carlo et d'équations analytiques. Le schéma du model est présenté sur la figure 7.1.

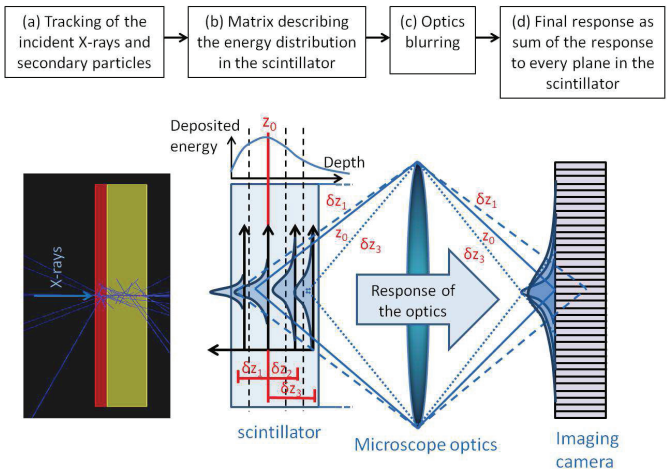

Figure 7.1: Schéma du model développé pour la simulation de la résolution spatiale. Le modèle inclut la réponse du scintillateur et l'effet des optiques de microscopie.

La partie Monte Carlo (MC) a été développée pour obtenir la réponse du scintillateur, c'est-à-dire l'étendue de diffusion de l'énergie déposée dans le scintillateur. Le logiciel utilisé est Geant4, une "boite à outils" mise en place pour développer son propre calcul MC. Des photons X primaires dont nous avons fixé l'énergie entre 5 et 80 keV sont

envoyés sur le scintillateur, perpendiculairement à la surface. Les photons X peuvent interagir avec les atomes du scintillateur ou du substrat par effet photoélectrique, diffusion Compton ou diffusion Rayleigh, pouvant donc éjecter des électrons. Les atomes, laissés dans un état excité, se relaxent en émettant des photons X (fluorescence) ou des électrons Auger. Tous les électrons et photons-X primaires et secondaires sont suivis jusqu'à ce que leur énergie soit inférieure à 250 eV. Chaque photon ou électron dépose l'énergie en plusieurs étapes et en plusieurs positions. Le scintillateur est divisé en voxels et l'énergie déposée dans chaque voxel est accumulée pendant la simulation. En sortie, le calcul Monte Carlo donne une matrice qui décrit la distribution de l'énergie déposée dans le volume du scintillateur. L'énergie totale déposée dans la couche ainsi que la fonction d'étalement d'une ligne (LSF, Line Spread Function) et sa transformée de Fourier, la fonction de transfert de modulation (MTF, Modulation Transfer Function) peuvent être calculées. La MTF décrit le contraste dans l'image en fonction de la fréquence spatiale de l'objet.

Différents matériaux ont été simulés. Les scintillateurs GGG (gadolinium gallium garnet) et LSO (lutetium orthosilicate) sont aujourd'hui produits à l'ESRF et sont l'état de l'art pour les détecteurs d'imagerie à haute résolution. Les scintillateurs GdAP, GdLuAP (gadolinium et lutetium aluminum perovskites) et Lu_2O_3 (lutetium oxide), au centre de ce projet, et d'autres scintillateurs ont été évalués pour le développement de noveaux détecteurs, comme le GdAG et LuAG (gadolinium et lutécium aluminium garnet).

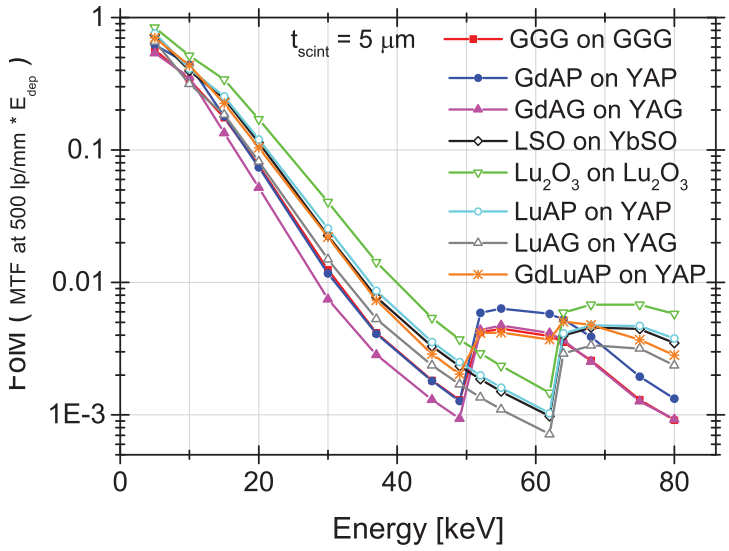

Figure 7.2: Facteur de mérite (contraste à 500 lp/mm × énergie déposé) calculées pour des couches de 5 μm d'épaisseur, en fonction de l'énergie et de la composition de la couche.

Sur la figure 7.2, le facteur de mérite FoM, calculé à partir de l'efficacité d'absorption

de la couche E_{dep} et de la valeur de la MTF à 500 lp/mm, est tracé en fonction de l'énergie. En principe il faudrait égalment tenir en compte le rendement lumineux pour pouvoir calculer la vraie efficacité de chaque scintillateur, mais ce paramètre ne peut pas être prévu avec précision avant que le matériau soit développé, donc il n'était pas inclus dans le calcul.

On remarque que selon l'énergie des photons, la FoM varie selon la composition des scintillateurs. Le rôle le plus important est joué par les seuils d'absorptions K des éléments présents dans le scintillateur et le substrat. Si l'énergie dépasse le seuil de production de fluorescence du substrat, la valeur de la courbe de MTF à basse fréquence est réduit due aux photons de fluorescence produites dans le substrat qui reviennent dans la couche. Cet effet est mieux illustré sur la figure 7.3. La couche scintillatrice (GdAP)

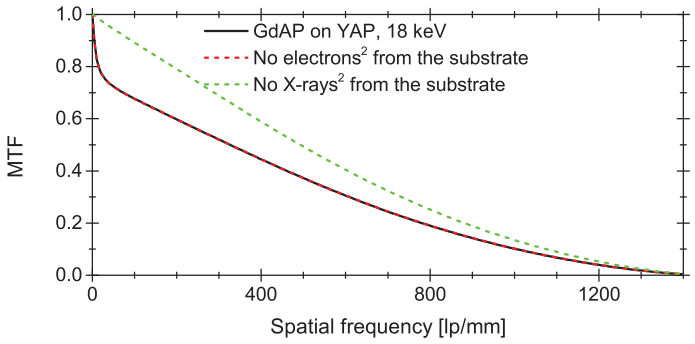

Figure 7.3: MTF calculées pour une couche de 5 μm du GdAP sur un substrat de YAP à 18 keV, en considérant tout les électrons et photons ou en supprimant les particules secondaires qui sont créés dans le substrat.

est déposée sur un substrat de pérovskite d'yttrium et d'aluminium: au-dessus de 17 keV, c'est à dire au-dessus de seuil d'absorption K de l'yttrium, le contraste décroit à 80% aux basses fréquences spatiales. Si les électrons secondaires produits dans le substrat ne sont pas pris en compte, le résultat est identique, mais lorsque les photons X secondaires produits dans la couche sont retirés de la simulation, la baisse brutale de la MTF à basse fréquence disparait.

Les courbes de MTF ont été comparées à des mesures faites sur la ligne de lumière BM05 à l'ESRF. Quelques résultats sont présentés sur la figure 7.4. Le contraste dans la courbe de MTF est augmenté à cause du contraste de phase, mais la variation avec les différents scintillateurs et l'énergie des rayons X est bien visible.

Des calculs analytiques ont été ajoutés pour prendre en compte la diffraction de la lumière et la profondeur de champ de l'objectif. Les courbes de MTF calculées à différentes positions dans l'épaisseur du scintillateur (MTF_j) sont modifiées par les variations de l'ouverture numérique, la longueur d'onde du scintillateur ainsi que la distance du plan focal des optiques 7.1. La MTF totale est donnée par la moyenne des MTF_j pondérées

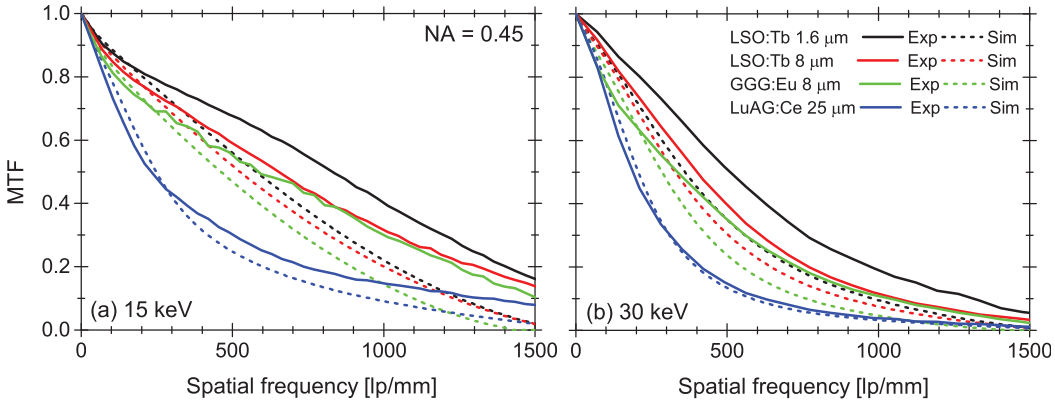

Figure 7.4: Courbes de MTF calculées et mesurées expérimentalement à (a) 15 keV et (b) 30 keV, pour différents scintillateurs combinés avec une optique de microscopie (ouverture numérique 0.45) et une caméra PCO2000. Grossissement total 66X, taille pixel du 0.11 μm.

par l'énergie déposée à chaque profondeur. La position du plan focal des optiques est choisie en évaluant la meilleure MTF totale.

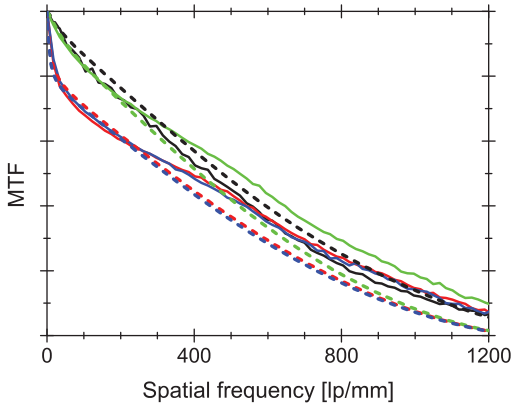

Figure 7.5: Courbes de MTF calculées et mesurées expérimentalement à 18 keV, pour différents scintillateurs, contenant ou pas de l'yttrium dans le substrat, combinées avec les optiques de microscopie (ouverture numérique 0.4) et une caméra PCO2000. Grossissement total 33X, taille pixel 0.22 μm.

L'effet du substrat prévu par les simulations a donc bien été confirmé expérimentalement. Les courbes de MTF calculées et mesurées sont comparées à 18 keV sur la figure 7.5. Si le substrat contient de l'yttrium, comme c'est le cas du GdLuAP:Eu et du LuAG:Eu, la réduction de contraste à basse fréquence prévue par les simulations est effectivement observée expérimentalement. Par contre, pour les scintillateurs LSO:Tb et GGG:Eu, qui sont déposés sur un substrat sans yttrium, cet effet n'est pas observé.

Couches minces de perovskite de gadolinium et lutetium

Un procèdé pour la croissance par épitaxie en phase liquide des couches de GdAP et GdLuAP sur des substrats monocristallins de YAP a été développé. Un solvant composé de B_2O_3 et PbO a été utilisé pour abaisser la température du bain liquide jusqu'à ≈1000℃.
A cause de la différence des paramètres de maille entre la couche et le substrat (mismatch), la qualité cristalline et optique des couches du GdAP n'est pas suffisante pour l'imagerie à haute résolution, en comparaison des couches de GGG :Eu ou LSO :Tb. L'écart de maille a ainsi été réduit en introduisant du lutétium dans le bain et donc dans la couche. Figure 7.6, les courbes de diffraction (omega-2theta) autour des réflections de Bragg (400) et (002) pour des échantillons orientés (100) et (001) sont tracés. Le pic

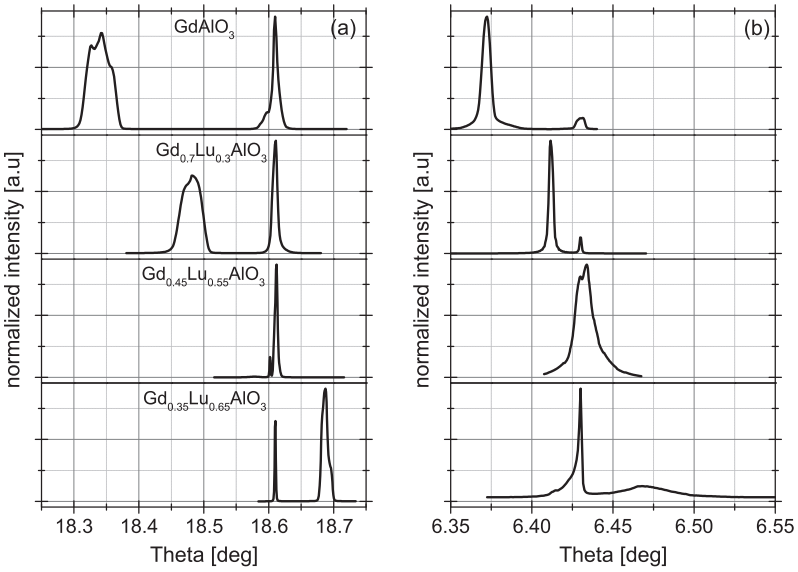

Figure 7.6: Mesures de diffraction (Omega-2theta) pour des couches de $Gd_xLu_{1-x}AlO_3$ sur un substrat de YAP. (a) Substrats orientés (100), réflexion de Bragg 400, substrats à 18.56° (b) substrats orientés (001), réflexion de Bragg 002, Substrats à 6.43°.

correspondant à la couche se rapproche du pic correspondant au substrat en ajoutant du lutetium, jusqu'à un optimum pour un rapport $R_{Lu} = \frac{Lu}{Lu+Gd} \approx 0.5$. Simultanément, la largeur du pic de la couche se réduit pour un écart de maille inférieur.
L'amélioration de la qualité de la surface entre les couches de GdAP et GdLuAP sont illustrées dans la figure 7.7, effectuées par microscopie électronique (SEM).
Les couches de GdLuAP:Eu ainsi obtenues sont très prometteuses pour l'imagerie à

haute resolution. Les couches du GdLuAP ont été dopées avec différentes concentrations

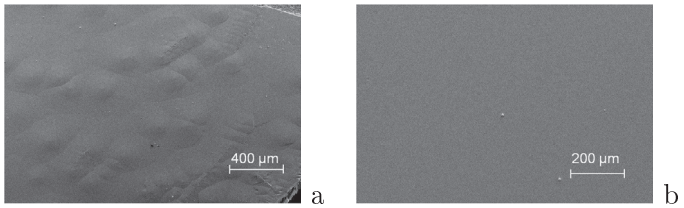

a b

Figure 7.7: Images SEM de la morphologie de surface pour (a) une couche de $Gd_{.10}Lu_{.90}AlO_3$ (haut écart de maille avec le substrat $\Delta\ell = 1.12$ %) et une couche de $Gd_{.10}Lu_{.90}AlO_3$ (faible écart de maille, $\Delta\ell = -0.04$ %).

d'europium afin d'optimiser le rendement de scintillation. Un rendement lumineux de ≈90% par rapport au rendement d'un monocristal de YAG :Ce, utilisé comme référence, a été mesuré. Le rendement ne dépend pas fortement de la concentration d'europium (dans la gamme mesurée), mais il dépend de manière plus surprenante de l'orientation du substrat de YAP. Une explication possible est la ségrégation de platine qui rentre de manière différente dans les couches, mais l'origine de cette différence n'est pas encore complètement claire.

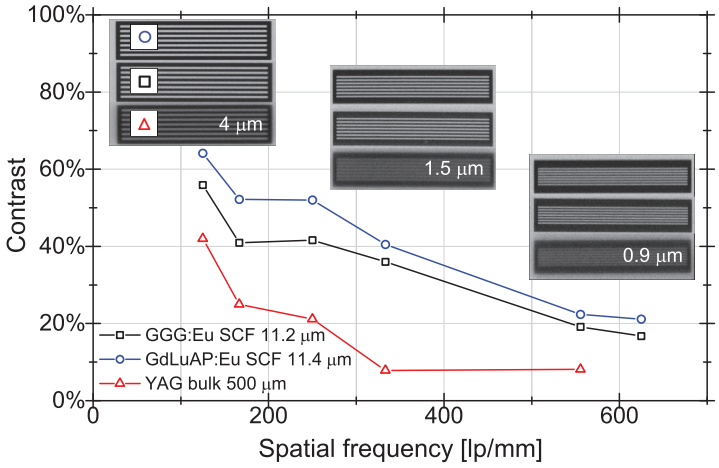

Figure 7.8: Images d'une mire en tungsten pour la résolution et les valeurs du contraste déduites en fonction de la fréquence spatiale. Optiques 20X/0.4 et PCO 200 caméra, 15 keV.

Les couches de GdLuAP :Eu ont été testées comme scintillateurs pour l'imagerie à haute résolution, et comparées avec des couches minces de GGG :Eu. Un contraste plus élevé a été mesuré pour le GdLuAP :Eu (figure 7.8).

Pourtant, la biréfringence des cristaux de YAP et GdLuAP peut dégrader la qualité de l'image (figure 7.8). Cet effet a été évalué pour les différentes orientations. Sur la figure 7.9, la MTF est évaluée pour différents angles du scintillateur autour de la normale à la surface. L'effet est très fort pour les scintillateurs orientés (011), mais beaucoup moins important pour l'orientation (100). Pour référence, la mème mesure a été effectuée aussi avec un scintillateur GGG :Eu, qui ne présente pas de biréfringence.

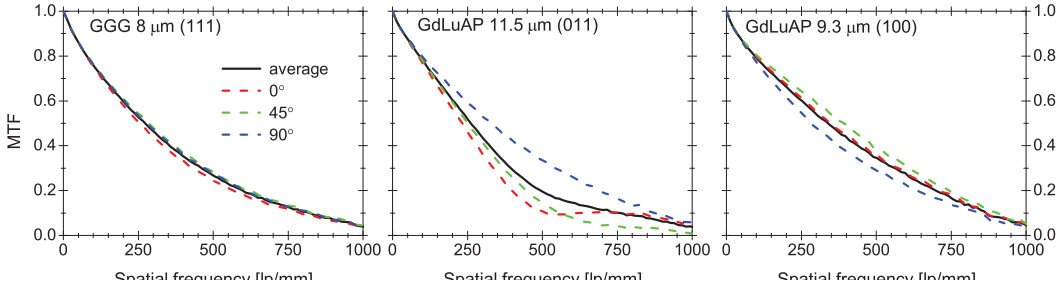

Figure 7.9: Courbes MTF mesurées à 16 keV à partir de l'image d'un bord. L'angle du scintillateur a été modifié autour de la normale à la surface. Optiques 10X/0.4, oculaire 3.3X, PCO2000. Taille du pixel 0.22 μm.

Couches minces de Lu_2O_3

La croissance des couches minces monocristallines de Lu_2O_3 : Eu par LPE a aussi été étudiée. Ce matériau présente une densité très haute et un très bon rendement a été mesuré pour des échantillons polycristallins ou en poudre. Ce matériau est donc le candidat idéal pour l'imagerie à rayons X à haute résolution et haute énergie.
Le FoM calculé pour le Lu_2O_3 est très élevée grâce à sa grande efficacité d'absorption. Sur la figure 7.10 les valeurs du FoM sont tracées. Le FoM est calculé à partir de la formule suivante :

$$\mathrm{FoM} = \mathrm{MTF}^{\mathrm{G4+Optics}}_{500\ \mathrm{lp/mm}} * \mathrm{E_{dep}} * \mathrm{LY} \tag{7.1}$$

en considérant le contraste à 500 lp/mm et l'énergie déposée obtenus par les simulations et le rendement mesuré expérimentalement. Le Lu_2O_3 doit avoir un rendement de 60 % comparé au LY du YAG :Ce pour obtenir des valeurs de FoM comparables avec le scintillateur LSO :Tb.
Des couches de Lu_2O_3 : Eu ont été déposées sur des substrats monocristallins de Lu_2O_3 : Yb. La croissance a été effectuée avec un solvant composé de B_2O_3 et PbO. Les substrats n'avait pas d'orientation préférentielle. La qualité optique des couches est excellente et la qualité cristalline est comparable à celle du substrat. Des exemples d'images faites

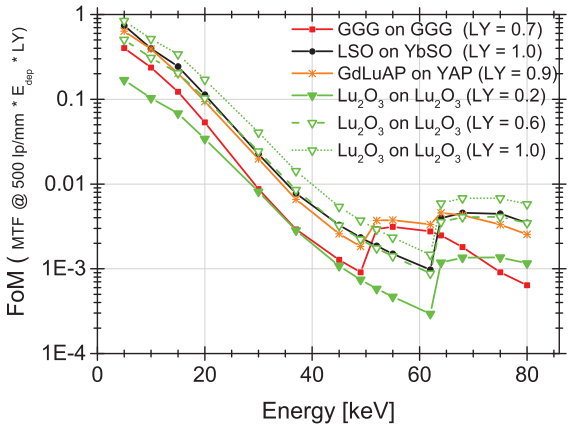

Figure 7.10: Facteur de mérite (MTF à 500 lp/mm $\times E_{dep} \times$ LY) de scintillateurs de 5 μm d'épaisseur, en fonction de l'energie des rayons X incidents.

avec de nouvelles couches minces de Lu_2O_3 : Eu sont montrées figure 7.11. Aujourd'hui, la limite principale des couches du Lu_2O_3 : Eu est leur rendement lumineux. Un rendement maximum de 20% par rapport au YAG :Ce a été obtenu pour les couches de Lu_2O_3 : Eu. La raison d'un rendement bien plus faible que prévu est très probablement du à une contamination très élevée en plomb et en zircone dans la couche. Cette contamination provient du solvant, ainsi que du creuset en platine. Le zircone est ajouté au platin pour augmenter sa résistance au plomb.

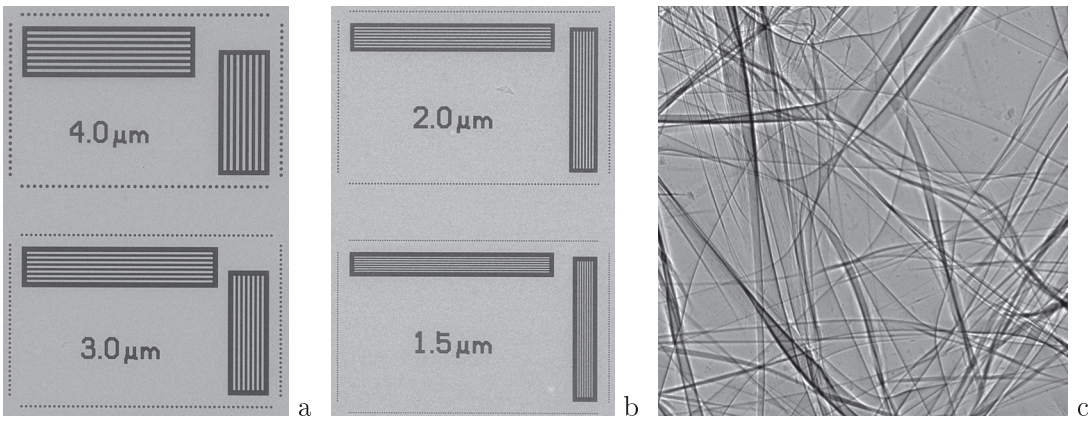

a b c

Figure 7.11: Images sous rayons X (a,b) d'une mire JIMA (c) d'une mousse en plastique avec un scintillateur Lu_2O_3:Eu en couche mince (8 μm), optique 20X/0.45, oculaire 3.3X et CCD camera PCO2000.

Conclusion

Un modéle pour évaluer la résolution spatiale des détecteurs à haute résolution pour l'imagerie à rayons X a été mis en place. Le modèle a été validé avec des mesures expérimentales, et peut être maintenant utilisé pour prévoir la résolution spatiale des nouvelles couches à développer, ainsi qu'aider dans le choix de la meilleur configuration du détecteur à rayon X.

Deux nouveaux types de scintillateurs monocristallins en couche minces on été développés et caractérisés.

Les scintillateurs basés sur une combinaison de perovskite de gadolinium et lutétium, dopés avec de l'europium, ont un bon rendement lumineux et une bonne qualité optique, qui dépend fortement de l'orientation cristallographique. L'orientation présentant le rendement le plus élevé n'est pas adaptée pour l'imagerie à très haute résolution due à la biréfringence qui dégrade la qualité de l'image. Par consequence, le procédé de croissance par LPE doit être amélioré pour les orientations presentant une biréfringence réduite, avec pour objectif de réduire les contaminations dans la couche et d'améliorer le rendement lumineux.

Les scintillateurs à base d'oxide de lutetium ont une très haute efficacité d'absorption et une très bonne qualité optique, mais un rendement très bas comparé aux autres scintillateurs en couche mince. La grande quantité de plomb nécessaire pour abaisser suffisamment la température de croissance donne un bain très corrosif pour le creuset en platine, et donc de très fortes contaminations dans la couche, qui probablement sont la raison du faible rendement de scintillation observé. Un nouveau type de bain moins riche en plomb doit donc être étudié pour réduire ou soupprimer ce problème de contamination.

Summary

X-ray detectors for high spatial resolution imaging are mainly based on indirect detection. The detector consists of a converter screen (scintillator), light microscopy optics and CCD or CMOS camera. The screen converts part of the absorbed X-rays into a visible light image, which is projected onto the camera by means of the optics. The detective quantum efficiency of the detector is strongly influenced by the properties of the converter screen (X-ray absorption, spread of energy deposition, light yield and emission wavelength).

To obtain detectors with micrometer and sub-micrometer spatial resolution, thin (1-20 μm) single crystal film (SCF) scintillators are required. These scintillators are layers grown on a substrate by liquid phase epitaxy (LPE). The critical point for these layers is their weak absorption, especially at energies exceeding 20 keV. At the European Synchrotron radiation Facility (ESRF), X-ray imaging applications can exploit energies up to 120 keV. Therefore, the development of new scintillating materials is currently investigated. The aim is to improve the contradictory compromise between absorption and spatial resolution, to increase the detection efficiency while keeping a good image contrast even at high energy.

The first part of this work presents a model describing high-resolution detectors, which was developed to calculate the modulation transfer function (MTF) of the system as a function of the X-ray energy. The model can be used to find the optimal combination of scintillator and visible light optics for different energy ranges and guide the choice of the materials to be developed as SCF scintillators. In the second part, two new kinds of scintillators for high-resolution are presented: the gadolinium-lutetium aluminum perovskite ($Gd_{0.5}Lu_{0.5}AlO_3 : Eu$) and the lutetium oxide ($Lu_2O_3 : Eu$) SCFs.